FULL-WAVE SURFACE INTEGRAL EQUATION METHOD FOR ELECTROMAGNETIC-CIRCUIT SIMULATION OF THREE-DIMENSIONAL INTERCONNECTS IN LAYERED MEDIA

A Dissertation

by

NUR KURT KARSILAYAN

Submitted to the Office of Graduate Studies of
Texas A&M University
in partial fulfillment of the requirements for the degree of

DOCTOR OF PHILOSOPHY

May 2010

Major Subject: Electrical Engineering

FULL-WAVE SURFACE INTEGRAL EQUATION METHOD FOR ELECTROMAGNETIC-CIRCUIT SIMULATION OF THREE-DIMENSIONAL INTERCONNECTS IN LAYERED MEDIA

A Dissertation

by

NUR KURT KARSILAYAN

Submitted to the Office of Graduate Studies of
Texas A&M University
in partial fulfillment of the requirements for the degree of

DOCTOR OF PHILOSOPHY

Approved by:

Chair of Committee,	Krzysztof A. Michalski
Committee Members,	Kai Chang
	Weiping Shi
	Mark E. Everett
Head of Department,	Costas N. Georghiades

May 2010

Major Subject: Electrical Engineering

ABSTRACT

Full-Wave Surface Integral Equation Method for
Electromagnetic-Circuit Simulation of Three-Dimensional Interconnects
in Layered Media. (May 2010)
Nur Kurt Karsilayan, B.S., Bilkent University;
M.S., Portland State University
Chair of Advisory Committee: Dr. Krzysztof A. Michalski

A new full-wave surface impedance integral equation method is presented for three-dimensional arbitrary-shaped interconnect parasitic extraction in layered media. Various new ways of applying voltage and current excitations for electromagnetic-circuit simulation are introduced. A new algorithm is proposed for matrix formation of electromagnetic-circuit simulation, low frequency solution and layered media so that it can be easily integrated to a Rao-Wilton-Glisson based method of moment code. Two mixed potential integral equation forms of the electric field integral equation are adapted along with the Michalski-Mosig formulations for layered kernels to model electromagnetic interactions of interconnects in layered media over a conducting substrate. The layered kernels are computed directly for controllable accuracy. The proposed methods are validated against existing methods for both electromagnetic and electromagnetic-circuit problems.

To Ilker

ACKNOWLEDGMENTS

I would like to thank Krzysztof A. Michalski for advising me on my doctoral research. I would like to thank my committee members, Kai Chang, Weiping Shi, and Mark Everett, for serving on my committee. The classes by Krzysztof A. Michalski, Kai Chang, and Weiping Shi are valuable contributions to my knowledge.

I would like to thank both my former and current managers, Jim Falbo and Rick Pier, at Mentor Graphics, for their understanding.

Although my family is thousands of miles away, they constantly have cared and supported me, for which I am grateful. I finally would like to thank my husband, Aydin Ilker Karsilayan, for believing in me.

TABLE OF CONTENTS

CHAPTER Page

LIST OF TABLES

LIST OF FIGURES

FIGURE Page

FIGURE Page

CHAPTER I

INTRODUCTION

A. Problem Statement

Parasitic extraction of the interconnects and the substrate in integrated circuits (IC), printed circuit boards or packages continues to be an important research topic as the switching frequency, density and complexity of processes and designs continue to increase [1]. Earlier, the process definitions included several layers of planar dielectrics and the designs were composed of regular rectangular (Manhattan-type) interconnects and square vias. Over the years, the number of dielectric layers increased explosively in addition to new non-planar dielectric requirements [2]. Now, it is more common to encounter non-Manhattan interconnects with trapezoidal cross-sections and even cylindrical vias in recent process descriptions. At lower frequencies, quasi-static assumptions were sufficient to simulate interconnects over substrate, however the effect of substrate becomes visible at GHz frequencies which cannot be ignored [3]. These process and design requirements along with higher frequencies create new research problems such as electromagnetic-circuit simulation of arbitrary-shaped three-dimensional interconnects over conducting substrate layers.

Parasitic extraction is the general term used for modeling unwanted electromagnetic interactions among interconnects and the substrate. Sample three-dimensional (3-D) interconnect over a substrate is illustrated in Fig. 1. Sample cross-sections and layer parameters of a lightly and a heavily doped substrate are shown in Fig. 2 and 3, respectively, where ρ represents resistivity [3, 4].

Parasitic extraction problem involves modeling in both the electromagnetic and

---

The journal model is *IEEE Transactions on Automatic Control.*

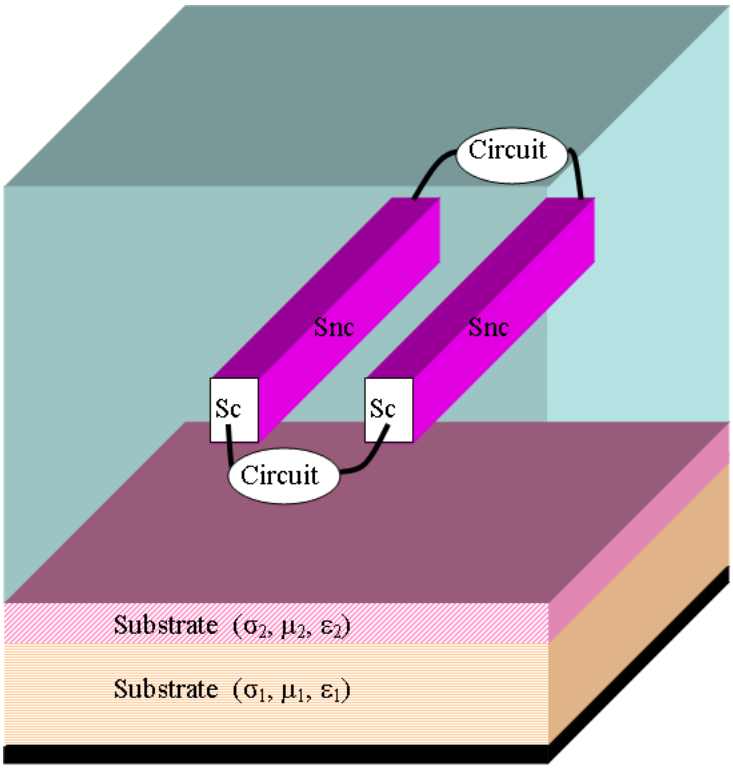

Fig. 1. Parasitic extraction of 3-D interconnects over substrate

the circuit domains.

The electromagnetic part of the problem consists of solving the Maxwell equations based on boundary conditions on conducting surfaces. For time-harmonic fields, differential form of Maxwell equations for a homogeneous, linear, non-dispersive, isotropic media can be stated in frequency domain as follows [5–7],

$$\nabla \times \boldsymbol{E} = -j\omega\mu\boldsymbol{H} - \boldsymbol{M}, \tag{1.1}$$

$$\nabla \times \boldsymbol{H} = j\omega\epsilon\boldsymbol{E} + \boldsymbol{J}, \tag{1.2}$$

$$\nabla \cdot \boldsymbol{E} = \rho_e/\epsilon, \tag{1.3}$$

$$\nabla \cdot \boldsymbol{H} = \rho_m/\mu, \tag{1.4}$$

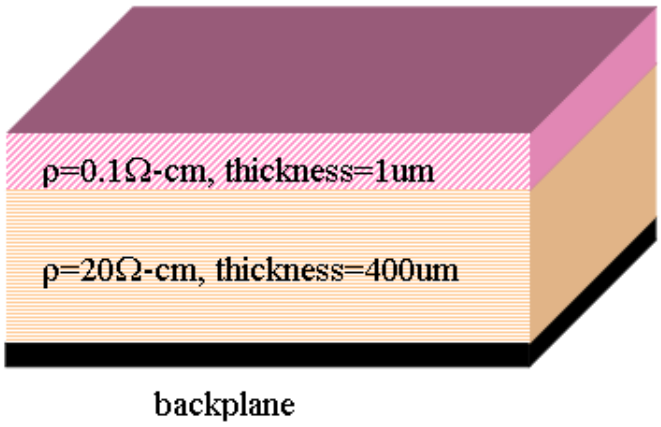

Fig. 2. Lightly doped substrate

where $\boldsymbol{E}$ and $\boldsymbol{H}$, $\boldsymbol{J}$ and $\boldsymbol{M}$, $jw\epsilon\boldsymbol{E}$[1] and $jw\mu\boldsymbol{H}$, ρ_e and ρ_m are the electric and magnetic field vectors, the total electric and magnetic current densities, the electric and magnetic displacement currents, and the electric and magnetic charge densities, respectively. Note that, (1.1) and (1.2) are called the Faraday and the Ampere laws, respectively, whereas (1.3) and (1.4) are called the Gauss laws. Another basic set of equations are called the continuity equations which are obtained by taking the divergence of (1.1) and (1.2),

$$\nabla \cdot \boldsymbol{M} = -j\omega\rho_m, \tag{1.5}$$

$$\nabla \cdot \boldsymbol{J} = -j\omega\rho_e \tag{1.6}$$

The circuit part of the problem involves solving a system of equations for the port currents or voltages for applied voltages and currents through the contact surfaces, respectively. In Fig. 1, S_c and S_{nc} represent contact and non-contact surfaces,

[1]Regular and bold letters represent scalar and vector quantities, respectively.

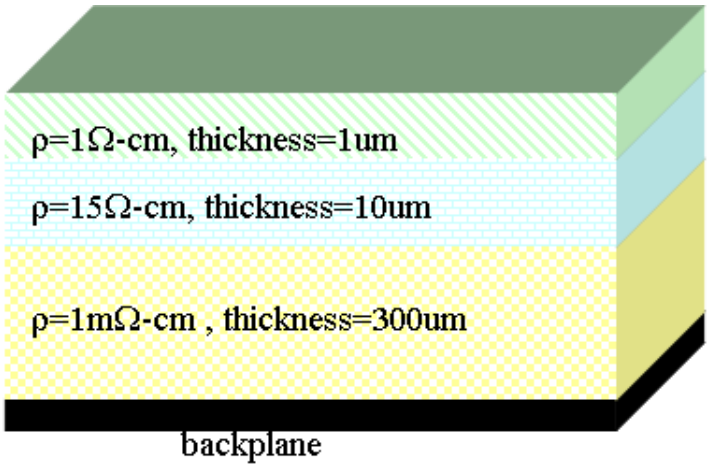

Fig. 3. Heavily doped substrate

respectively. The contact surfaces simply represent the interface between the electromagnetic and the circuit domains.

B. State of the Art

In this section, the parasitic extraction problem is explained from various point of views using a top-down approach. First of all, high level approaches to the real-life parasitic extraction problems are described. Then field solvers based on various assumptions are discussed. After that, current methods for applying excitations at the ports or interconnect terminals are summarized. Finally, the low frequency problem along with its remedies is described.

1. High Level Parasitic Extraction

Most commercial IC chip layout parasitic extraction tools address the problem using rule-based techniques where resistance (R), capacitance (C) and inductance (L) are

treated separately using analytical equations or table look-ups that are based on two-dimensional (2-D) or 3-D field solvers [8–10]. In the parasitic extraction area, "field solver" term usually implies electromagnetic-circuit simulators which output results in terms of R, L, C, instead of electromagnetic fields. Although it may be impractical to use a 3-D field solver for extracting the whole chip, it is possible to extract the parasitics of the critical nets or the specific parts of the chip, in order to incorporate into the final parasitic netlist.

2. Field Solvers

Field solvers can be classified as differential-equation-based [3] and integral-equation-based [11–23], where the whole domain and only the conductors are discretized, respectively. Integral equation (IE) field solvers can be grouped based on volume integral equation (VIE) [14, 19, 21, 23–25] and surface integral equation (SIE) [11–13, 15–18, 20, 22], where volumes and surfaces of the conductors are discretized, respectively. Most of the existing IE field solvers are based on electro-quasi-static (EQS) [12, 13, 15], magneto-quasi-static (MQS) [14] or electro-magneto-quasi-static (EMQS) [17] assumptions.

The EQS assumption implies neglecting the magnetic displacement current in the Maxwell equation for the Faraday law (1.1), and therefore leads to the following potential formula:

$$\phi(\boldsymbol{r}) = \frac{1}{\epsilon}\int \rho_e(\boldsymbol{r}')G(R)ds', \tag{1.7}$$

$$G(R) = \frac{1}{4\pi R}, \tag{1.8}$$

where $R = |\boldsymbol{R}|$, $\boldsymbol{R} = \boldsymbol{r} - \boldsymbol{r}'$, ρ_e is the surface charge density and $G(R)$[2] is the quasi-

[2]Green function for homogeneous medium. "Homogeneous" and "free-space"

static (QS) Green function[3], $\boldsymbol{r}$ and $\boldsymbol{r}'$ are the testing and the source coordinates, respectively, with respect to the origin. With the use of method of moments (MOM)[4], conductor surfaces are discretized into panels to obtain charge distributions based on applied voltages on each panel.

The MQS assumption implies ignoring the electric displacement current in the Ampere law (1.2) [14]. The MQS approach, along with the Coulomb gauge, leads to the following vector potential formula, where $\boldsymbol{J}(\boldsymbol{r}')$ is the volumetric electric current density:

$$\boldsymbol{A}(\boldsymbol{r}) \;=\; \mu \int \boldsymbol{J}(\boldsymbol{r}')G(R)dv'. \tag{1.9}$$

In [14], conductors are partitioned into filaments and the electric field depends on both vector and scalar potentials through the mixed potential integral equation (MPIE) representation of the electric field integral equation (EFIE), as follows:

$$\boldsymbol{E} \;=\; -j\omega\boldsymbol{A} - \boldsymbol{\nabla}\phi, \tag{1.10}$$

where $\boldsymbol{\nabla}\phi$ is treated as the voltage difference between nodes and $\boldsymbol{E}$ is defined as $\boldsymbol{J}/\sigma$ inside the filaments, where σ is the conductivity of the medium. The VIE method is also called the partial element equivalent circuit (PEEC) method when each filament is represented with partial R and L values [26–31]. These methods require frequency-dependent volume discretizations, since at higher frequencies the skin depth becomes smaller and the conductor cross-section needs to be discretized finer, which increases the number of unknowns. Both [12] and [14] are based on

---

terms will be used interchangeably throughout the dissertation.

[3] "Green function" and "kernel" terms will be used interchangeably throughout the dissertation.

[4] "Method of Moments" is also called "Boundary Element Method."

multipole expansion method, which depends on the free-space kernel, therefore both require that the dielectric surfaces and the substrate are discretized similarly to conductors, which increases the number of unknowns and slows down the solution of an interconnect system for a realistic IC process with tens of dielectric layers.

In the EMQS method, both capacitive and inductive effects are considered by assuming a surface charge, whereas in the MQS approach, surface charge is neglected. In [14], the EMQS approach is applied based on the volume and surface discretization for currents and charges, respectively, whereas in [17], only surface discretization is considered. The error due to QS assumptions is negligible when the maximum interconnect dimension is much less than the wavelength that corresponds to the highest frequency of interest [32]. However, with the increasing design density and frequencies, there is a growing need for full-wave field solvers.

The majority of the existing full-wave IE approaches treat planar layered media similarly to the conducting objects, by discretizing the dielectric interfaces and the substrate and using free-space Green functions [17, 20, 23, 33–36]. The full-wave free-space Green function is obtained without neglecting the displacement currents in the Maxwell equations,

$$G(R) = \frac{e^{-jkR}}{4\pi R}, R = |\boldsymbol{R}|, \boldsymbol{R} = \boldsymbol{r} - \boldsymbol{r}' \tag{1.11}$$

where $k = \omega\sqrt{\mu\epsilon}$ is the wavenumber. This kernel is used for computing the vector magnetic and the scalar electric potentials.

Since modern IC processes include tens of dielectric layers, discretizing each dielectric interface and the substrate region causes significant increase in the number of unknowns when the free-space Green function is used. Some full-wave, VIE methods that are published in the last decade are based on a different type of basis and testing functions, called conduction modes, in order to avoid extremely fine volume dis-

cretizations at high frequencies and speed up the volume integral equation methods. However, these approaches do not handle layered media [24, 25]. Several full-wave SIE methods published in recent years treat conductors as 2-D surfaces with impedance boundary conditions and use layered, instead of free-space kernels. However, these methods are based on the assumption of 2.5-D simulation of regular rectangular objects where only the upper and lower surfaces of the conductors are modeled [37, 38]. Another full-wave, VIE method [19] uses layered medium kernels limited to only two half spaces and the kernels are approximated with discrete complex image method (DCIM). However, the disadvantages of the VIE approach, such as finer discretization of the conductor cross-sections for higher frequencies, still remain. The DCIM method has been used as a faster alternative to the direct evaluation of the Sommerfeld integrals that arise in layered media Green functions and involves approximating the spectral integrand by a finite sum of complex exponential terms [39]. However, the accuracy of this method is neither predictable nor controllable, unlike the direct computation of Sommerfeld integrals by numerical quadrature and extrapolations.

Most existing electromagnetic, geophysics or induction modeling methods [40–42] in layered media use the Michalski-Zheng or the Michalski-Mosig layered medium kernels [43, 44]. To our knowledge, although these kernels are often used in these areas, they have never been applied to the full-wave, surface-based parasitic extraction of three-dimensional interconnects and the substrate.

3. External Excitations

There are several approaches for applying external excitations in field solvers. One approach is called point-fed or delta-gap excitation where a current or a voltage is applied through the terminals separated by a distance much smaller than a wavelength [35, 45]. The drawback of this approach is its sensitivity to the selection of

the parameters such as length and direction. Another method is to convert the gradient of scalar potential in MPIE to a voltage difference between nodes [14, 17, 19]. The drawback of this method is that it requires post-computation of the current at contact surfaces to obtain the port impedance. A recent approach presented in [18] is based on injecting current sources through the contact surfaces. This method does not require any post-processing, however the details of applying current and voltage sources and how to compute port admittances and impedances are not discussed.

4. Low Frequency Problem

In addition to the formulation and simulation aspects of the parasitic extraction problem, there is another aspect called the low frequency problem. This arises when the frequency goes to zero, the vector potential term in MPIE goes to zero but the scalar potential term goes to infinity. In order to alleviate this problem, the surface current is separated into divergence-free and non-divergence-free parts. Divergence-free part is modeled with loop functions whereas non-divergence-free part is modeled with tree or star functions [21, 35, 36, 46–51]. Although low frequency solutions are provided in the context of electromagnetic problems, there is no published algorithms to address the low frequency problem in the context of SIE 3-D parasitic extraction in layered media.

C. Proposed Method

A new full-wave, surface impedance equation method for electromagnetic-circuit simulation of 3-D arbitrary-shaped conducting objects in layered media is proposed. Two MPIE forms are used for the parasitic extraction problem where different sets of layered medium kernels are involved. Unlike most of the existing approaches, no

assumptions are made for the layered media Green functions since the Sommerfeld integrals are computed directly for controllable accuracy. Since the layer information is independent of the interconnect geometries, the Sommerfeld integrals can be computed one time and used later during the geometry processing.

Another contribution of this dissertation is that several ways of applying external voltage and current sources are discussed in detail in the proposed electromagnetic-circuit simulation approach. The advantage of the proposed method is that the port admittance or impedance is computed directly, therefore no model order reduction techniques are required, unlike in PEEC methods. Another advantage is that for a multi-port system, the impedances or the admittances are not required to be computed for all the ports to obtain the admittance or the impedance of a single port, respectively.

In addition to the above contributions, the proposed matrix formation algorithm for addressing low frequency problem, electromagnetic-circuit simulation and layered media is addressed such that it can be incorporated to an existing RWG-based MOM code easily.

In Chapter II, the electromagnetic surface integral formulation is explained. In Chapter III, the electromagnetic-circuit interface, several ways of applying external voltage and current sources along with the circuit equations are presented. In Chapter IV, the discretization of the surface integral equations using the MOM is explained. In Chapter V, practical considerations and a new algorithm for handling the low frequency problem, electromagnetic-circuit simulation and layered media are introduced. In Chapter VI, numerical results are presented for the validation of the proposed methods. Chapter VII contains the concluding comments and recommendations for future work.

CHAPTER II

ELECTROMAGNETIC SURFACE INTEGRAL FORMULATION

A. Generic Surface Integral Formulation

Any arbitrary-shaped 3-D interconnect can be considered as a homogeneous volume residing in a layered medium over the substrate as shown in Fig. 1. Original interconnect problem can be considered as in Fig. 4. Dielectric and lossy conducting objects have real and complex values of permittivities, respectively.

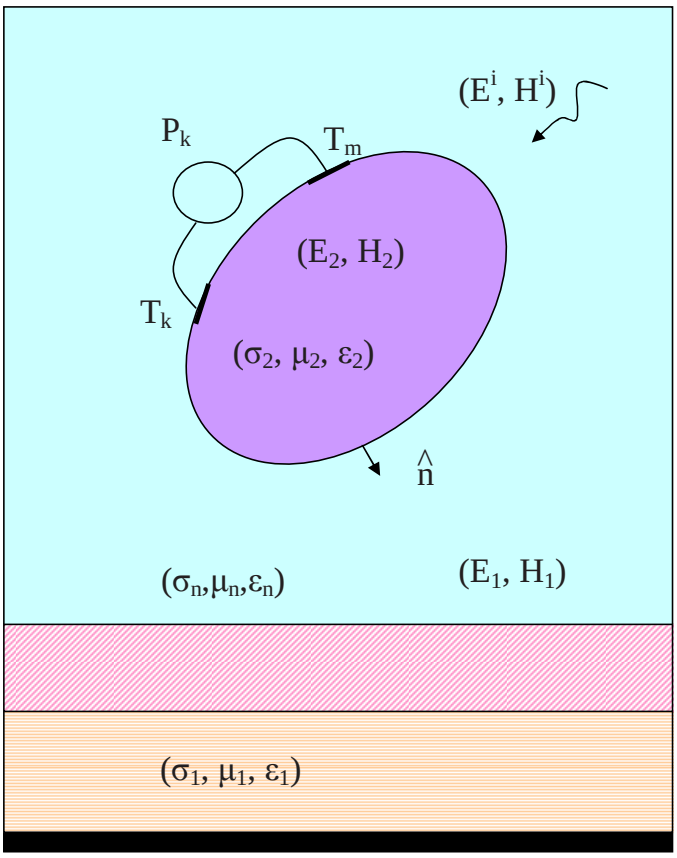

Fig. 4. Original problem

According to the equivalence principle, the original problem in Fig. 4 can be

separated into interior and exterior equivalent problems where the Green functions for the interior and the exterior regions can be used, respectively [5, 52]. The surface normal unit vector $\hat{n}$ points outward and ($\boldsymbol{E}^i$,$\boldsymbol{H}^i$) represent the incident electric and magnetic fields. Another form of the external sources is port voltage or current sources. Note that, a port is represented as P_k in Fig. 4. Each port is associated with two circuit terminals[1]. Note that, the two terminals associated with port P_k is represented as T_k and T_m in Fig. 4.

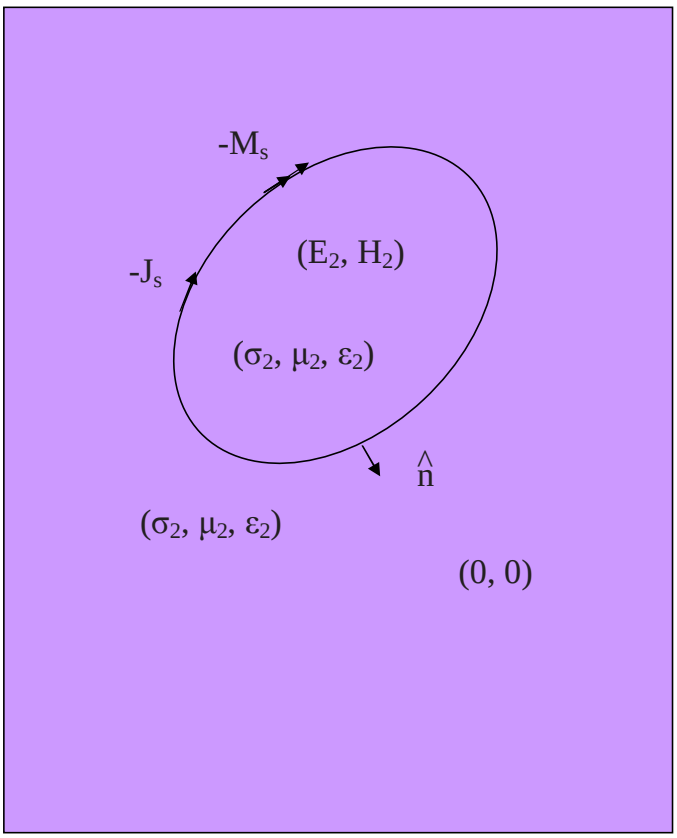

Fig. 5. Interior equivalent

[1]A terminal and a node represent the same concept in circuit domain. A terminal in circuit domain corresponds to a contact surface in electromagnetic domain.

For the interior problem in Fig. 5, the exterior and the interior fields are zero and non-zero, respectively. To compensate for the difference in the interior and the exterior fields, fictitious electric and magnetic surface currents are assumed to exist over the surface. The medium parameters for the whole space is that of the interior region. Note that, there are no external sources in the interior equivalent problem.

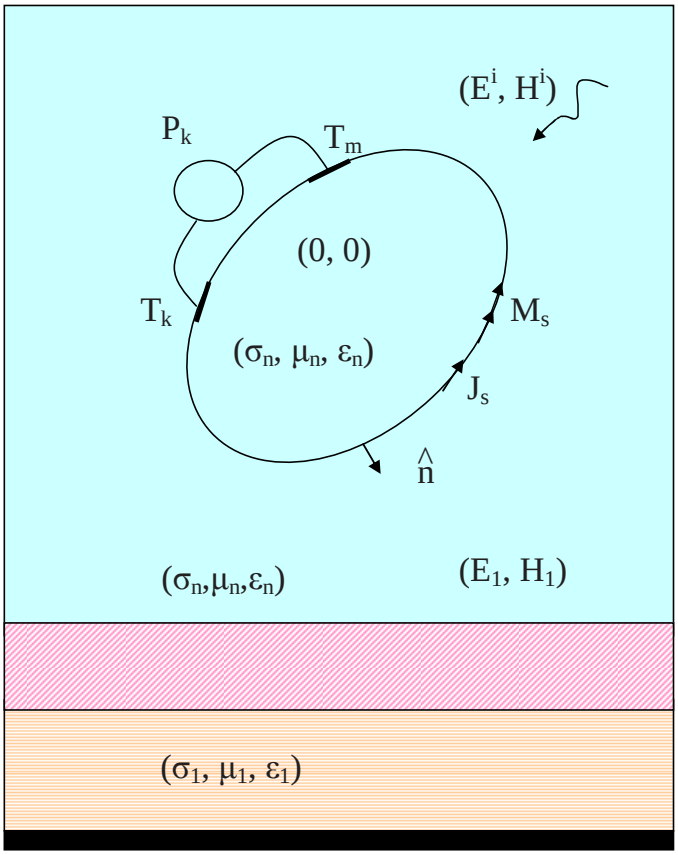

Fig. 6. Exterior equivalent

For the exterior problem in Fig. 6, the interior and the exterior fields are zero and non-zero, respectively and the fictitious surface currents are in the opposite direction of the interior problem. The medium parameters are the same as the exterior region which contains multiple planar layers that extend to infinity in the horizontal

directions. In the exterior equivalent problem layered medium instead of homogeneous Green functions are used unlike the interior equivalent problem. Note that, the incident fields or the ports are kept in the exterior equivalent problem.

The SIE for the interior and the exterior equivalent problems when both mediums are homogeneous are summarized in Appendix A.

B. Surface Impedance Integral Formulation

Since interconnects have finite high conductivity, they can be considered as lossy objects with surface impedance boundary condition [18, 37, 38, 53–57]. This eliminates the need of interior equations and magnetic surface current in (A.1) and (A.2), therefore the number of unknowns are reduced significantly. When the surface impedance boundary condition is used, the tangential electric field on the surface satisfy the following condition.

$$(\boldsymbol{E}^i + \boldsymbol{E}^s)_{tan} = Z_s \boldsymbol{J}_s \tag{2.1}$$

where Z_s, $\boldsymbol{E}^i$ and $\boldsymbol{E}^s$ represent the surface impedance, possible incident electric field, and the scattered electric field, respectively. For high frequency,

$$Z_s = \frac{1+j}{\sigma\delta}, \quad \delta = \frac{1}{\sqrt{\pi f \mu \sigma}}, \tag{2.2}$$

where σ and δ represent the conductivity and the skin depth, respectively. For low frequency,

$$Z_s = \frac{1}{\sigma t}, \tag{2.3}$$

where t represents the conductor thickness.

When the exterior region is layered medium as in Fig. 6, the layered Green functions [41, 43, 44, 58] are used in the exterior equivalent problem. Two different MPIE forms for the layered medium are explained in Appendix B [41, 43, 58]. General

form of MPIE in terms of vector and scalar potentials can be stated as follows,

$$\boldsymbol{E}^s = -j\omega\boldsymbol{A} - \boldsymbol{\nabla}\phi, \tag{2.4}$$

where the vector potential formula is the same in both MPIE forms but the content of the vector dyadic Green function, $\underline{\boldsymbol{G}}^A$ is different as shown in the table on page 103.

$$\boldsymbol{A} = \mu_0 \oint \underline{\boldsymbol{G}}^A \cdot \boldsymbol{J}_s \; dS' \tag{2.5}$$

The scalar potential formula is different since the second form has a correction term which are stated as follows,

$$\phi = -\frac{1}{j\omega\epsilon_0} \oint G^\phi \boldsymbol{\nabla} \cdot \boldsymbol{J}_s \; dS' \tag{2.6}$$

$$\phi = -\frac{1}{j\omega\epsilon_0} \oint (G^\phi \boldsymbol{\nabla} \cdot \boldsymbol{J}_s + \hat{\boldsymbol{z}} C^\phi \cdot \boldsymbol{J}_s) \; dS' \tag{2.7}$$

Surface impedance integral equation is obtained by using (2.4) in (2.1).

$$Z_s \boldsymbol{J}_s + (j\omega\boldsymbol{A} + \boldsymbol{\nabla}\phi)_{tan} = (\boldsymbol{E}^i)_{tan} \tag{2.8}$$

The two MPIE equations with impedance boundary condition on non-contact surfaces can be summarized as follows.

$$\begin{aligned} Z_s \boldsymbol{J}_s + \oint [j\omega\mu_0 \underline{\boldsymbol{G}}^A \cdot \boldsymbol{J}_s - \frac{1}{j\omega\epsilon_0} \boldsymbol{\nabla}(G^\phi \boldsymbol{\nabla}'_s \cdot \boldsymbol{J}_s)] dS' \\ = \boldsymbol{E}^i_{tan}, \boldsymbol{r}' \epsilon S_{nc} \end{aligned} \tag{2.9}$$

$$\begin{aligned} Z_s \boldsymbol{J}_s + \oint [j\omega\mu_0 \underline{\boldsymbol{G}}^A \cdot \boldsymbol{J}_s - \frac{1}{j\omega\epsilon_0} \boldsymbol{\nabla}(G^\phi \boldsymbol{\nabla}'_s \cdot \boldsymbol{J}_s \\ + \hat{\boldsymbol{z}} C^\phi \cdot \boldsymbol{J}_s)] dS' = \boldsymbol{E}^i_{tan}, \boldsymbol{r}' \epsilon S_{nc} \end{aligned} \tag{2.10}$$

CHAPTER III

ELECTROMAGNETIC-CIRCUIT FORMULATION

A. Electromagnetic-Circuit Interface

The boundary condition or the interface between electromagnetic and circuit domains are through the injected normal currents or applied voltages at the contact surfaces as shown in Fig. 7. The continuity equation for non-contact and contact surfaces are assumed to be different such that there is an additional accumulated charge on the contact surface due to the normal injected current from outside [18, 59].

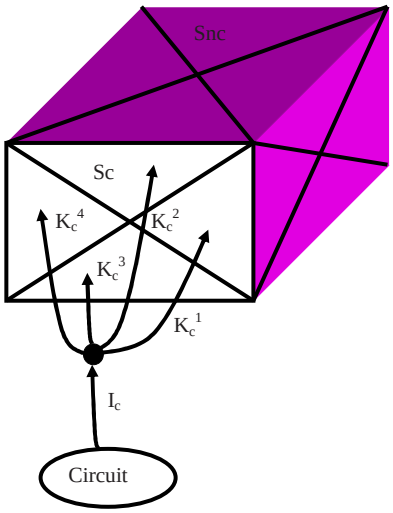

Fig. 7. Interface between circuit and electromagnetic parts

The continuity equation at non-contact and contact surfaces are stated as follows,

$$-j\omega\rho_e = \boldsymbol{\nabla}'_s \cdot \boldsymbol{J}_s, \;\; \boldsymbol{r}' \epsilon S_{nc}, \tag{3.1}$$

$$-j\omega\rho_e = \boldsymbol{\nabla}'_s \cdot \boldsymbol{J}_s - K_c, \;\; \boldsymbol{r}' \epsilon S_c, \tag{3.2}$$

where K_c represents the current density injected through contact c, S_c and S_{nc} repre-

sent contact and non-contact surfaces as shown in Fig. 7, respectively. Note that, the thin wires pointing to contact surfaces represent the interface between electromagnetic and circuit domains which means they are not modeled as part of the electromagnetic domain. A contact surface in the electromagnetic domain can be considered as a terminal or a node in the circuit domain as shown in Fig. 7. The current flowing from the circuit domain to node c and the currents flowing into each contact element n from node c are represented as I_c and K_c^n, respectively. Kirchoff current Law (KCL) is applied at node c where the sum of the contact element normal currents is equal to the terminal current.

$$I_c = \sum_{n=1}^{N_c} K_c^n \tag{3.3}$$

where N_c is the number of contact elements corresponding to contact c and K_c^n is the injected normal current through contact element n.

In addition to modifying the continuity equation for current conservation, the potential at the contact surface S_c is matched to the circuit voltage at node c. Note that, the reference for the circuit node and the electromagnetic contact surface potentials are ground and infinity, respectively. The potential equations for each MPIE form are stated as follows,

$$V_c = -\frac{1}{j\omega\epsilon_0}[\oint G^{\phi}(\boldsymbol{\nabla}'_s \cdot \boldsymbol{J}_s - K_c)dS'], \boldsymbol{r}'\epsilon S_c, \tag{3.4}$$

$$\begin{aligned} V_c = -\frac{1}{j\omega\epsilon_0} \oint (G^{\phi}(\boldsymbol{\nabla}'_s \cdot \boldsymbol{J}_s - K_c) \\ + \hat{\boldsymbol{z}} C^{\phi} \cdot \boldsymbol{J}_s)\ dS', \boldsymbol{r}'\epsilon S_c, \end{aligned} \tag{3.5}$$

where V_c represents the potential at the contact surface.

The set of equations for two MPIE forms at the electromagnetic-circuit interface

or contact surfaces, S_c are summarized as follows,

$$Z_s \boldsymbol{J}_s + \oint [j\omega\mu_0 \underline{\boldsymbol{G}}^A \cdot \boldsymbol{J}_s - \frac{1}{j\omega\epsilon_0} \boldsymbol{\nabla}(G^\phi(\boldsymbol{\nabla}'_s \cdot \boldsymbol{J}_s - K_c))] dS' = \boldsymbol{E}^i_{tan}, \boldsymbol{r}' \epsilon S_c \tag{3.6}$$

$$Z_s \boldsymbol{J}_s + \oint [j\omega\mu_0 \underline{\boldsymbol{G}}^A \cdot \boldsymbol{J}_s - \frac{1}{j\omega\epsilon_0} \boldsymbol{\nabla}(G^\phi(\boldsymbol{\nabla}'_s \cdot \boldsymbol{J}_s - K_c) + \hat{\boldsymbol{z}} C^\phi \cdot \boldsymbol{J}_s)] dS' = \boldsymbol{E}^i_{tan}, \boldsymbol{r}' \epsilon S_c \tag{3.7}$$

B. Circuit Equations

Until now, the SIE for contact and non-contact surfaces are introduced. The electromagnetic contact surface is associated with a circuit node or terminal. In this section, the terminal and port currents and voltages are discussed in detail. Additionally, various ways of applying external voltage and current excitations at the terminals or ports are explained. Fig. 8 shows the reference current directions at a port which is associated with two terminals.

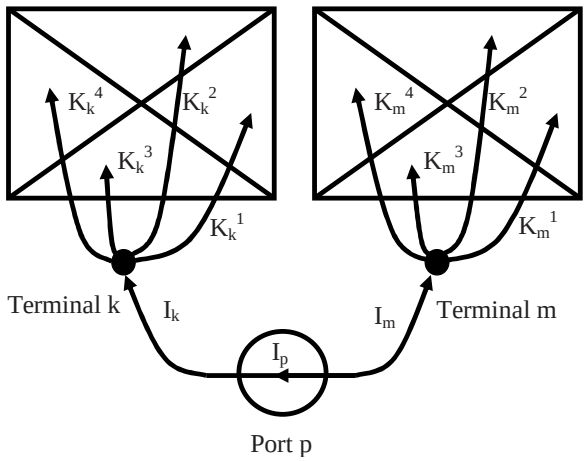

Fig. 8. Current definitions at a port

Port current, I_p and terminal currents, I_k and I_m are related as follows,

$$I_p = I_k \tag{3.8}$$

$$I_p = -I_m \tag{3.9}$$

Port voltages in Fig. 8 relate to terminal voltages as follows.

$$V_p = V_k - V_m \tag{3.10}$$

The relation between the port and the terminal voltages or currents can be summarized in matrix form as follows,

$$[V_p] = [Q][V_c], \tag{3.11}$$

$$[I_c] = [Q]^T[I_p] \tag{3.12}$$

where Q can be considered as the translational matrix between the port and the terminal voltages.

The port in Fig. 8 can be connected to a current or a voltage source or another circuit which may have its own linear equations. In that case, the port currents and the voltages in Fig. 8 should match the circuit port currents and voltages. For both the circuit and the interface, modified nodal analysis (MNA) can be used because of its flexibility of defining floating voltages such as port voltages along with terminal currents as unknowns [60].

When a voltage source is applied at the port or the port is short-circuited, an additional equation for relating the port voltage to the voltage supply is needed,

$$V_p = \begin{cases} V_s, & excitation \\ 0, & short-circuit \end{cases} \tag{3.13}$$

where V_s represents the voltage source.

When a current source is applied at the port or the port is open-circuit, an additional equation for relating the port current to the current supply is needed,

$$I_p = \begin{cases} I_s, & excitation \\ 0, & open-circuit \end{cases} \tag{3.14}$$

where I_s represents the current source.

Another excitation method can be through terminals directly as shown in Fig. 7 where the other terminal from the circuit is grounded. In this case, port current and voltage equations drop and the current or voltage sources are applied as follows,

$$I_c = \begin{cases} I_s, & excitation \\ 0, & open-circuit \end{cases} \tag{3.15}$$

$$V_c = \begin{cases} V_s, & excitation \\ 0, & short-circuit \end{cases} \tag{3.16}$$

The circuit equations are summarized in terms of modified nodal analysis (MNA) equations as follows,

$$[R][I_p] + [P][V_p] = [U] \tag{3.17}$$

where [U] represents current or voltage sources.

In summary, the proposed electromagnetic-circuit simulation method is flexible such that the voltage and the current sources can be applied through the ports or the terminals. For all types of excitations, additional equations are introduced for contact element potentials and terminal currents where the number of equations are the same as contact element count and terminal count, respectively. In the case of port excitations, there are $N_t + N_p$ equations in addition to the contact potential and terminal current equations, where N_t and N_p are the terminal and the port counts,

respectively.

C. Summary of Electromagnetic-Circuit Equations

The set of equations for MPIE form I is as follows,

$$Z_s \boldsymbol{J}_s + \oint [j\omega\mu_0 \underline{\boldsymbol{G}}^A \cdot \boldsymbol{J}_s - \frac{1}{j\omega\epsilon_0} \boldsymbol{\nabla}(G^\phi \boldsymbol{\nabla}'_s \cdot \boldsymbol{J}_s)] dS' = (\boldsymbol{E}^i)_{tan}, \boldsymbol{r}' \epsilon S_{nc} \tag{3.18}$$

$$Z_s \boldsymbol{J}_s + \oint [j\omega\mu_0 \underline{\boldsymbol{G}}^A \cdot \boldsymbol{J}_s - \frac{1}{j\omega\epsilon_0} \boldsymbol{\nabla}(G^\phi (\boldsymbol{\nabla}'_s \cdot \boldsymbol{J}_s - K_c))] dS' = (\boldsymbol{E}^i)_{tan}, \boldsymbol{r}' \epsilon S_c \tag{3.19}$$

$$V_c = -\frac{1}{j\omega\epsilon_0} [\oint G^\phi (\boldsymbol{\nabla}'_s \cdot \boldsymbol{J}_s - K_c) dS'], \boldsymbol{r}' \epsilon S_c, \tag{3.20}$$

$$I_c = \sum_{n=1}^{N_c} K_c^n \tag{3.21}$$

$$[V_p] = [Q][V_c], \tag{3.22}$$

$$[I_c] = [Q]^T [I_p], \tag{3.23}$$

$$[R][I_p] + [P][V_p] = [U] \tag{3.24}$$

The set of equations for MPIE form II is as follows,

$$Z_s \boldsymbol{J}_s + \oint [j\omega\mu_0 \underline{\boldsymbol{G}}^A \cdot \boldsymbol{J}_s - \frac{1}{j\omega\epsilon_0} \boldsymbol{\nabla}(G^\phi \boldsymbol{\nabla}'_s \cdot \boldsymbol{J}_s + \hat{\boldsymbol{z}} C^\phi \cdot \boldsymbol{J}_s)] dS' = (\boldsymbol{E}^i)_{tan}, \boldsymbol{r}' \epsilon S_{nc} \tag{3.25}$$

$$Z_s \boldsymbol{J}_s + \oint [j\omega\mu_0 \underline{\boldsymbol{G}}^A \cdot \boldsymbol{J}_s - \frac{1}{j\omega\epsilon_0} \boldsymbol{\nabla}(G^\phi (\boldsymbol{\nabla}'_s \cdot \boldsymbol{J}_s - K_c) + \hat{\boldsymbol{z}} C^\phi \cdot \boldsymbol{J}_s)] dS' = (\boldsymbol{E}^i)_{tan}, \boldsymbol{r}' \epsilon S_c \tag{3.26}$$

$$V_c = -\frac{1}{j\omega\epsilon_0} \oint (G^\phi (\boldsymbol{\nabla}'_s \cdot \boldsymbol{J}_s - K_c) + \hat{\boldsymbol{z}} C^\phi \cdot \boldsymbol{J}_s)\ dS', \boldsymbol{r}' \epsilon S_c, \tag{3.27}$$

$$I_c = \sum_{n=1}^{N_c} K_c^n \tag{3.28}$$

$$[V_p] = [Q][V_c], \tag{3.29}$$

$$[I_c] = [Q]^T[I_p], \tag{3.30}$$

$$[R][I_p] + [P][V_p] = [U] \tag{3.31}$$

CHAPTER IV

DISCRETIZATION OF THE SURFACE INTEGRAL EQUATIONS

In Chapter II, the SIE for electromagnetic domain is introduced. In Chapter III, the SIE for electromagnetic and circuit interface along with circuit equations are presented. In this chapter, MOM is used to transform the continuous surface integrals to a linear matrix system [45].

A. Problem Description

Before going into the discretization steps, the domain of the problem is described as follows.

Let each conductor surface be s_i where $s_i \in (S_c \cup S_{nc})$.

Let each s_i be composed of surface elements, l_j, where $s_i = \cup l_j$ and $l_j \in L_i$, where L_i is the set of triangular elements corresponding to s_i.

Let each l_j corresponds to nodes ($n_k \in N_i$) and edges ($e_l \in E_i$) at surface s_i, where N_i and E_i represent the set of nodes and edges corresponding to s_i.

Let $c_m \in C$ be the contact surface on s_i which maps to a subset of elements, $l_j \subset L_i$. Note that C represents the set of contact numbers.

Let c_m also map to a port $p_n \in P$, where P represents the set of port numbers in the problem domain.

Note that, the total set of surfaces, nodes, elements, edges are $S = S_c \cup S_{nc}$, $N = \cup N_i$, $L = \cup L_i$, and $E = \cup E_i$.

There are two directional mappings among the defined sets as follows, $N \leftrightarrow E$, $N \leftrightarrow L$, $E \leftrightarrow L$, $C \leftrightarrow L$, $C \leftrightarrow P$.

B. Discretization of the Surface Impedance Integral Equation

Each conductor surface is discretized with triangles and well-known Rao-Wilton-Glisson (RWG) functions are used for basis and testing functions over triangles. An RWG function is defined over pairs of triangle surfaces as follows [61].

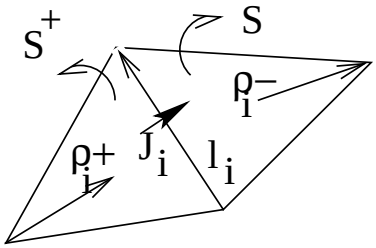

Fig. 9. RWG function

$$\boldsymbol{\Lambda}_i(\boldsymbol{r}) = \begin{cases} l_i \frac{\boldsymbol{\rho}_i^+}{2S^+}, & \boldsymbol{r}\epsilon S^+ \\ l_i \frac{\boldsymbol{\rho}_i^-}{2S^-}, & \boldsymbol{r}\epsilon S^- \end{cases}$$

$$\nabla \cdot \boldsymbol{\Lambda}_i(\boldsymbol{r}) = \begin{cases} \frac{l_i}{S^+}, & \boldsymbol{r}\epsilon S^+ \\ -\frac{l_i}{S^-}, & \boldsymbol{r}\epsilon S^- \end{cases} \tag{4.1}$$

The advantages of the RWG functions are that there are no accumulated line charges at the element boundaries since the current is continuous at the edges and the divergence of the RWG function is piecewise constant which is suitable for representing the surface charge. Surface currents are expanded by RWG functions as follows,

$$\boldsymbol{J} = \sum_{i=1}^{N_e} \boldsymbol{\Lambda}_i J_i \tag{4.2}$$

where N_e, $\boldsymbol{\Lambda}_i$ and J_i represent the number of independent edges, the RWG function and the normal current at edge i, respectively. Parameters are depicted in Fig. 9 for reference.

Two more basis functions are used in addition to RWG functions for expanding the voltages and the currents over each contact surface.

$$\upsilon_n = \begin{cases} 1, \boldsymbol{r}' \in S_n \\ 0, \boldsymbol{r}' \notin S_n \end{cases} \tag{4.3}$$

$$\varphi_n = \begin{cases} \frac{1}{S_n}, \boldsymbol{r}' \in S_n \\ 0, \boldsymbol{r}' \notin S_n \end{cases} \tag{4.4}$$

The voltage at contact c is expanded as follows.

$$V_c = \sum_{n=1}^{N_c} \upsilon_n V_c^n \tag{4.5}$$

where N_c and V_c^n are the number of contact elements associated with contact c and the potential at contact element n, respectively. Each contact surface is equipotential, therefore

$$V_c^n = V_c \tag{4.6}$$

The current density at contact c is expanded as follows.

$$K_c = \sum_{n=1}^{N_c} \varphi_n K_c^n \tag{4.7}$$

where K_c^n represents the normal current injected through the contact element n. Testing and expanding the integral equations in (3.18), (3.20) and (3.19) with the

corresponding functions provides the following matrix system,

$$\begin{bmatrix} A & C & 0 & 0 & 0 & 0 \\ E & F & 0 & G & 0 & 0 \\ 0 & L & I & 0 & 0 & 0 \\ 0 & 0 & 0 & -Q & 0 & I \\ 0 & 0 & I & 0 & -Q^T & 0 \\ 0 & 0 & 0 & 0 & R & P \end{bmatrix} \begin{bmatrix} J \\ K \\ I_c \\ V_c \\ I_p \\ V_p \end{bmatrix} = \begin{bmatrix} E^g \\ 0 \\ 0 \\ 0 \\ 0 \\ U \end{bmatrix} \tag{4.8}$$

where U is either a voltage or a current source, and J, K, I_c, V_c, I_p, V_p are the unknown vectors for the surface current, the normal current, the terminal currents, the terminal voltages, the port currents and the port voltages of size N_e, N_c, N_t, N_t, N_p, and N_p, respectively. Note that, N_e, N_c, N_t and N_p are non-boundary edge, contact element, terminal and port counts, respectively.

When the excitation is through a voltage source at a port, the solution for the unknown vector, I_p directly provides port admittance values. Similarly, when the excitation is through a current source at a port, the solution for the unknown vector, V_p provides the port impedance values.

Note that, the sub-matrix, A corresponds to the electromagnetic part of the system, C, E, F, G, L represent the sub-matrices for electromagnetic and circuit interactions. The rest of the sub-matrices correspond to the Kirchoff current and voltage laws in circuit domain.

Sub-matrix A has different formation depending on the MPIE form used. The

matrix that corresponds to (3.18) is as follows,

$$\begin{aligned} A = {} & j\omega\mu_0\langle \boldsymbol{\Lambda}_i, \underline{\boldsymbol{G}}^A, \boldsymbol{\Lambda}_j\rangle \\ & + \frac{1}{j\omega\epsilon_0}\langle \boldsymbol{\nabla}\cdot\boldsymbol{\Lambda}_i, G^\phi, \boldsymbol{\nabla}\cdot\boldsymbol{\Lambda}_j\rangle \\ & + Z_s\langle \boldsymbol{\Lambda}_i, \boldsymbol{\Lambda}_j\rangle \end{aligned} \tag{4.9}$$

The matrix that corresponds to (3.25) is as follows,

$$\begin{aligned} A = {} & j\omega\mu_0\langle \boldsymbol{\Lambda}_i, \underline{\boldsymbol{G}}^A, \boldsymbol{\Lambda}_j\rangle \\ & + \frac{1}{j\omega\epsilon_0}(\langle \boldsymbol{\nabla}\cdot\boldsymbol{\Lambda}_i, G^\phi, \boldsymbol{\nabla}\cdot\boldsymbol{\Lambda}_j\rangle \\ & + \langle \boldsymbol{\nabla}\cdot\boldsymbol{\Lambda}_i, C^\phi\hat{\boldsymbol{z}}, \boldsymbol{\Lambda}_j\rangle) + Z_s\langle \boldsymbol{\Lambda}_i, \boldsymbol{\Lambda}_j\rangle \end{aligned} \tag{4.10}$$

Similarly, sub-matrix E has different formations depending on the MPIE form used. The matrix that corresponds to (3.20) is as follows,

$$E = \frac{1}{j\omega\epsilon_0}\langle \varphi_m, G^\phi, \boldsymbol{\nabla}\cdot\boldsymbol{\Lambda}_j\rangle \tag{4.11}$$

The matrix that corresponds to (3.27) is as follows,

$$E = \frac{1}{j\omega\epsilon_0}(\langle \varphi_m, G^\phi, \boldsymbol{\nabla}\cdot\boldsymbol{\Lambda}_j\rangle + \langle \varphi_m, \hat{\boldsymbol{z}}C^\phi, \boldsymbol{\Lambda}_j\rangle) \tag{4.12}$$

The rest of the sub-matrices are as follows,

$$C = -\frac{1}{j\omega\epsilon_0}\langle \boldsymbol{\nabla}\cdot\boldsymbol{\Lambda}_i, G^\phi, \varphi_n\rangle \tag{4.13}$$

$$F = -\frac{1}{j\omega\epsilon_0}\langle \varphi_m, G^\phi, \varphi_n\rangle \tag{4.14}$$

$$G = \langle \varphi_m, \upsilon_n\rangle \tag{4.15}$$

$$E^g = \langle \boldsymbol{\Lambda}_i, \boldsymbol{E}^i\rangle \tag{4.16}$$

where $\langle \boldsymbol{f}, \boldsymbol{g}\rangle = \oint \boldsymbol{f}\cdot\boldsymbol{g}\ dS'$.

The term for dyadic vector potential kernel $\underline{\boldsymbol{G}}^A$ in (4.9) is expanded as follows,

$$\begin{aligned}\langle \boldsymbol{\Lambda}_i, \underline{\boldsymbol{G}}^A, \boldsymbol{\Lambda}_j \rangle = \langle \boldsymbol{\Lambda}_i, (\boldsymbol{xx} + \boldsymbol{yy}) G^A_{xx} + \boldsymbol{zz} G^A_{zz} \\ + \boldsymbol{zx} G^A_{zx} + \boldsymbol{zy} G^A_{zy} + \boldsymbol{xz} G^A_{xz} \\ + \boldsymbol{yz} G^A_{yz}, \boldsymbol{\Lambda}_j \rangle\end{aligned} \tag{4.17}$$

The term for dyadic vector potential kernel $\underline{\boldsymbol{G}}^A$ in (4.10) is stated as follows,

$$\begin{aligned}\langle \boldsymbol{\Lambda}_i, \underline{\boldsymbol{G}}^A, \boldsymbol{\Lambda}_j \rangle = \langle \boldsymbol{\Lambda}_i, (\boldsymbol{xx} + \boldsymbol{yy}) G^A_{xx} + \boldsymbol{zz} G^A_{zz} \\ + \boldsymbol{xz} G^A_{xz} + \boldsymbol{yz} G^A_{yz}, \boldsymbol{\Lambda}_j \rangle\end{aligned} \tag{4.18}$$

C. Integration over Source and Observation Triangles

In the case of free-space Green functions, integration of vector products over source and observation triangles appear as follows,

$$\begin{aligned} I &= \langle \boldsymbol{\Lambda}_i, G, \boldsymbol{\Lambda}_j \rangle \\ &= \int_S \boldsymbol{\Lambda}_i \cdot \int_{S'} \boldsymbol{\Lambda}_i G(R)\, dS'\, dS, \end{aligned} \tag{4.19}$$

The integration in (4.19) is performed by transforming the triangles to a unit triangle with area coordinates (ξ', η', ζ'). This requires computation of three integration types as follows,

$$I_a = \int_0^1 \int_0^{1-\eta'} G(\xi', \eta') d\xi' d\eta' \tag{4.20}$$

$$I_b = \int_0^1 \int_0^{1-\eta'} \xi' G(\xi', \eta') d\xi' d\eta' \tag{4.21}$$

$$I_c = \int_0^1 \int_0^{1-\eta'} \eta' G(\xi', \eta') d\xi' d\eta' \tag{4.22}$$

Considering single Gauss point for the testing triangle, the integral in (4.19) can

be stated as follows,

$$\begin{aligned} I = \frac{l_i l_j}{4S'}(\boldsymbol{\rho}_i \cdot (\boldsymbol{r}_3 - \boldsymbol{r}_j) I_a \\ + \boldsymbol{\rho}_i \cdot (\boldsymbol{r}_1 - \boldsymbol{r}_3) I_b + \boldsymbol{\rho}_i \cdot (\boldsymbol{r}_2 - \boldsymbol{r}_3) I_c) \end{aligned} \tag{4.23}$$

The difference between the free-space and the dyadic kernels is that the testing and the basis functions are not projected on each other but on the dyads as follows,

$$\begin{aligned} I &= \langle \boldsymbol{\Lambda}_i, \boldsymbol{ab} G^A_{ab}, \boldsymbol{\Lambda}_j \rangle \\ &= \int_S (\boldsymbol{\Lambda}_i \cdot \boldsymbol{a}) \int_{S'} (\boldsymbol{\Lambda}_i \cdot \boldsymbol{b}) G^A_{ab}(\rho, z|z')\ dS'\ dS, \end{aligned} \tag{4.24}$$

where $\boldsymbol{a}$ or $\boldsymbol{b}$ correspond to cartesian unit vectors $\boldsymbol{x}$, $\boldsymbol{y}$, or $\boldsymbol{z}$.

As in the free-space kernel case, we need to compute three types of integrals over the basic triangles as follows,

$$I_a = \int_0^1 \int_0^{1-\eta'} G^A_{ab}(\xi', \eta') d\xi' d\eta', \tag{4.25}$$

$$I_b = \int_0^1 \int_0^{1-\eta'} \xi' G^A_{ab}(\xi', \eta') d\xi' d\eta', \tag{4.26}$$

$$I_c = \int_0^1 \int_0^{1-\eta'} \eta' G^A_{ab}(\xi', \eta') d\xi' d\eta'. \tag{4.27}$$

Integral in (4.24) now can be written as follows,

$$\begin{aligned} I = \frac{l_i l_j (\boldsymbol{a} \cdot \boldsymbol{\rho}_i)}{4S'}(\boldsymbol{b} \cdot (\boldsymbol{r}_3 - \boldsymbol{r}_j) I_a \\ + \boldsymbol{b} \cdot (\boldsymbol{r}_1 - \boldsymbol{r}_3) I_b + \boldsymbol{b} \cdot (\boldsymbol{r}_2 - \boldsymbol{r}_3) I_c) \end{aligned} \tag{4.28}$$

Note that, the integrals in (4.20)-(4.22) or (4.25)-(4.27) are computed using Gauss Quadrature rules [52].

D. Low Frequency Solution

Low frequency problem arises as the vector potential term in (2.4) goes to zero while the scalar potential term goes to infinity when the frequency goes to zero. In order to alleviate this problem, surface current is separated into divergence-free and non-divergence-free parts [35, 36, 46, 47, 49, 50].

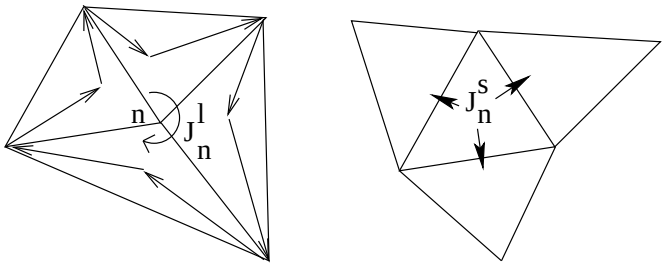

(a) loop function (b) star function

Fig. 10. Loop and star functions

Loop and star (LS) functions are used to separate the surface currents into divergence-free and non-divergence-free parts [46]. LS functions are linear combinations of RWG functions and depicted in Fig. 10(a) and 10(b). Reference direction for loop and star currents are clockwise and outward, respectively. Loop and star functions are defined as follows,

$$\boldsymbol{L}_n = \sum_{i=1}^{N_n} \nu_i \frac{\boldsymbol{\Lambda}_i}{l_i} \tag{4.29}$$

$$\boldsymbol{S}_n = \sum_{i=1}^{3} \nu_i \frac{\boldsymbol{\Lambda}_i}{l_i}, \tag{4.30}$$

where N_n is the number of edges for loop n and ν_i can be -1 or 1 depending on the current direction or 0 if the corresponding edge is not involved in the loop. L_n and

S_n are divergence-free and non-divergence-free, respectively, as follows,

$$\nabla \cdot \boldsymbol{L}_n = 0, \tag{4.31}$$

$$\nabla \cdot \boldsymbol{S}_n \neq 0. \tag{4.32}$$

Surface currents can be represented by LS functions as follows,

$$\boldsymbol{J} = \sum_{n=1}^{N_l} \boldsymbol{L}_n J_n^l + \sum_{n=1}^{N_e - N_l} \boldsymbol{S}_n J_n^s, \tag{4.33}$$

where N_l and N_e are the number of internal nodes and non-boundary edges, respectively. Note that, N_l is the same as the internal node count when the object has open surface, however, for the case of closed surfaces, N_l is equal to the internal node count decreased by 1 in order to obtain linearly independent equations.

When (3.18),(3.19) and (3.20) are discretized with LS functions, sub-matrices A, C and E in (4.8) is composed of four sub-matrices due to loop-loop, loop-star, star-loop, star-star interactions. Similarly, J and E^g vectors are composed of two sub-vectors due to loop and star parts.

$$\begin{bmatrix} \frac{1}{s}A^{ll} & A^{ls} & 0 & 0 & 0 & 0 & 0 \\ A^{sl} & sA^{ss} & C^{sp} & 0 & 0 & 0 & 0 \\ 0 & sE^{ps} & F & 0 & G & 0 & 0 \\ 0 & 0 & L & I & 0 & 0 & 0 \\ 0 & 0 & 0 & 0 & -Q & 0 & I \\ 0 & 0 & 0 & I & 0 & -Q^T & 0 \\ 0 & 0 & 0 & 0 & 0 & R & P \end{bmatrix} \begin{bmatrix} J^l \\ \frac{1}{s}J^s \\ K \\ I_c \\ V_c \\ I_p \\ V_p \end{bmatrix} = \begin{bmatrix} \frac{1}{s}E^l \\ E^s \\ 0 \\ 0 \\ 0 \\ 0 \\ U \end{bmatrix} \tag{4.34}$$

where s represents scaling for stability.

The details of sub-matrices in (4.34) is shown below.

$$A^{ll} = j\omega\mu_0\langle \boldsymbol{L}_i, \underline{\boldsymbol{G}}^A, \boldsymbol{L}_j\rangle + Z_s\langle \boldsymbol{L}_i, \boldsymbol{L}_j\rangle \tag{4.35}$$

$$A^{ls} = j\omega\mu_0\langle \boldsymbol{L}_i, \underline{\boldsymbol{G}}^A, \boldsymbol{S}_j\rangle + Z_s\langle \boldsymbol{L}_i, \boldsymbol{S}_j\rangle \tag{4.36}$$

$$A^{sl} = j\omega\mu_0\langle \boldsymbol{S}_i, \underline{\boldsymbol{G}}^A, \boldsymbol{L}_j\rangle + Z_s\langle \boldsymbol{S}_i, \boldsymbol{L}_j\rangle \tag{4.37}$$

$$A^{ss} = j\omega\mu_0\langle \boldsymbol{S}_i, \underline{\boldsymbol{G}}^A, \boldsymbol{S}_j\rangle + \frac{1}{j\omega\epsilon_0}\langle \boldsymbol{\nabla}\cdot\boldsymbol{S}_i, G^\phi, \boldsymbol{\nabla}\cdot\boldsymbol{S}_j\rangle + Z_s\langle \boldsymbol{S}_i, \boldsymbol{S}_j\rangle \tag{4.38}$$

$$C^{sp} = -\frac{1}{j\omega\epsilon_0}\langle \boldsymbol{\nabla}\cdot\boldsymbol{S}_i, G^\phi, \varphi_n\rangle \tag{4.39}$$

$$E^{ps} = \frac{1}{j\omega\epsilon_0}\langle \varphi_m, G^\phi, \boldsymbol{\nabla}\cdot\boldsymbol{S}_j\rangle \tag{4.40}$$

$$E^{l} = \langle \boldsymbol{L}_i, \boldsymbol{E}^i\rangle \tag{4.41}$$

$$E^{s} = \langle \boldsymbol{S}_i, \boldsymbol{E}^i\rangle \tag{4.42}$$

When (3.25),(3.26) and (3.27) are discretized with LS functions, there will be additional terms due to the correction kernel, C^ϕ. Some of these terms disappear when the testing function is a loop function.

$$\begin{bmatrix} \frac{1}{s}A^{ll} & A^{ls} & 0 & 0 & 0 & 0 & 0 \\ A^{sl} & sA^{ss} & C^{sp} & 0 & 0 & 0 & 0 \\ E^{pl} & sE^{ps} & F & 0 & G & 0 & 0 \\ 0 & 0 & L & I & 0 & 0 & 0 \\ 0 & 0 & 0 & 0 & -Q & 0 & I \\ 0 & 0 & 0 & I & 0 & -Q^T & 0 \\ 0 & 0 & 0 & 0 & 0 & R & P \end{bmatrix} \begin{bmatrix} J^l \\ \frac{1}{s}J^s \\ K \\ I_c \\ V_c \\ I_p \\ V_p \end{bmatrix} = \begin{bmatrix} \frac{1}{s}E^l \\ E^s \\ 0 \\ 0 \\ 0 \\ 0 \\ U \end{bmatrix} \tag{4.43}$$

The details of sub-matrices in (4.43) is shown below.

$$A^{ll} = j\omega\mu_0\langle \boldsymbol{L}_i, \underline{\boldsymbol{G}}^A, \boldsymbol{L}_j\rangle + Z_s\langle \boldsymbol{L}_i, \boldsymbol{L}_j\rangle \tag{4.44}$$

$$A^{ls} = j\omega\mu_0\langle \boldsymbol{L}_i, \underline{\boldsymbol{G}}^A, \boldsymbol{S}_j\rangle + Z_s\langle \boldsymbol{L}_i, \boldsymbol{S}_j\rangle \tag{4.45}$$

$$A^{sl} = j\omega\mu_0\langle \boldsymbol{S}_i, \underline{\boldsymbol{G}}^A, \boldsymbol{L}_j\rangle + \frac{1}{j\omega\epsilon_0}\langle \boldsymbol{\nabla}\cdot\boldsymbol{S}_i, \boldsymbol{z}C^\phi, \boldsymbol{L}_j\rangle + Z_s\langle \boldsymbol{S}_i, \boldsymbol{L}_j\rangle \tag{4.46}$$

$$\begin{aligned} A^{ss} = {} & j\omega\mu_0\langle \boldsymbol{S}_i, \underline{\boldsymbol{G}}^A, \boldsymbol{S}_j\rangle + \frac{1}{j\omega\epsilon_0}\langle \boldsymbol{\nabla}\cdot\boldsymbol{S}_i, G^\phi, \boldsymbol{\nabla}\cdot\boldsymbol{S}_j\rangle \\ & + \frac{1}{j\omega\epsilon_0}\langle \boldsymbol{\nabla}\cdot\boldsymbol{S}_i, \boldsymbol{z}C^\phi, \boldsymbol{S}_j\rangle + Z_s\langle \boldsymbol{S}_i, \boldsymbol{S}_j\rangle \end{aligned} \tag{4.47}$$

$$C^{sp} = -\frac{1}{j\omega\epsilon_0}\langle \boldsymbol{\nabla}\cdot\boldsymbol{S}_i, G^\phi, \varphi_n\rangle \tag{4.48}$$

$$E^{pl} = \frac{1}{j\omega\epsilon_0}\langle \varphi_m, \boldsymbol{z}C^\phi, \boldsymbol{L}_j\rangle \tag{4.49}$$

$$E^{ps} = \frac{1}{j\omega\epsilon_0}\langle \varphi_m, G^\phi, \boldsymbol{\nabla}\cdot\boldsymbol{S}_j\rangle + \frac{1}{j\omega\epsilon_0}\langle \varphi_m, \boldsymbol{z}C^\phi, \boldsymbol{S}_j\rangle \tag{4.50}$$

$$E^l = \langle \boldsymbol{L}_i, \boldsymbol{E}^i\rangle \tag{4.51}$$

$$E^s = \langle \boldsymbol{S}_i, \boldsymbol{E}^i\rangle \tag{4.52}$$

Note that, there is no contribution due to the correction kernel when the surface normal, $\boldsymbol{n}$ is equal to $\boldsymbol{z}$.

E. Discretization of the Generic Surface Integral Equations

The difference between surface impedance integral equations and generic SIE is that we have additional equations for the interior equivalent problem as well as magnetic surface currents. The generic SIE in (A.1) and (A.2) are discretized using RWG testing and basis functions as follows,

$$\begin{bmatrix} \sum_{m=1}^{2}\alpha_m A_m & \sum_{m=1}^{2}\alpha_m B_m \\ \sum_{m=1}^{2}-\beta_m B_m & \sum_{m=1}^{2}\beta_m C_m \end{bmatrix} \begin{bmatrix} J \\ M \end{bmatrix} = \begin{bmatrix} \alpha_1 E^g \\ \beta_1 H^g \end{bmatrix} \tag{4.53}$$

Each sub-matrix is obtained as follows,

$$A_m = j\omega\mu_m\langle \mathbf{\Lambda}_i, G_m, \mathbf{\Lambda}_j\rangle + \frac{1}{j\omega\epsilon_m}\langle \nabla\cdot\mathbf{\Lambda}_i, G_m, \nabla\cdot\mathbf{\Lambda}_j\rangle \tag{4.54}$$

$$B_m = \langle \mathbf{\Lambda}_i, \mathbf{\Lambda}_j \times \nabla' G_m\rangle + \frac{\gamma_m}{2}\langle \mathbf{\Lambda}_i, \hat{n}\times\mathbf{\Lambda}_j\rangle \tag{4.55}$$

$$C_m = j\omega\epsilon_m\langle \mathbf{\Lambda}_i, G_m, \mathbf{\Lambda}_j\rangle + \frac{1}{j\omega\mu_m}\langle \nabla\cdot\mathbf{\Lambda}_i, G_m, \nabla\cdot\mathbf{\Lambda}_j\rangle \tag{4.56}$$

$$E^g = \langle \mathbf{\Lambda}_i, \boldsymbol{E}^i\rangle \tag{4.57}$$

$$H^g = \langle \mathbf{\Lambda}_i, \boldsymbol{H}^i\rangle \tag{4.58}$$

The matrix system for EFIE and MFIE for PEC objects are as follows,

$$[A_1][J] = [E^g] \tag{4.59}$$

$$[-B_1][J] = [H^g] \tag{4.60}$$

CHAPTER V

SECSLM: THE TOOL FOR SURFACE ELECTROMAGNETIC-CIRCUIT SIMULATION IN LAYERED MEDIA

In this chapter, the tool that encapsulates the proposed methods is summarized. The flow and some important algorithms that incorporate various modes of operation are discussed.

A. System Inputs

The inputs to SECSLM include discretized geometry, frequency, layer, excitation, simulation and surface boundary condition information as shown in Fig. 11.

SECSLM supports discretized geometry in terms of triangular patches in neutral format from any outside mesher. The meshed input contains node and element information. The edge data is formed while reading the input. Reference edge current direction for the first encountered edge is assumed to be outward and normal to the edge. The same edge corresponding to a latter element is assigned a negative value which implies that the current direction is inward and normal to the edge. This avoids the computation of the current direction based on the surface normal and the edge vectors.

Depending on the layer mode whether it is free-space or layered, corresponding input files are used to compute the Green functions. The excitation input is either a plane wave or port voltage or current supply. Simulation modes are electromagnetic and electromagnetic-circuit. In the former case, only plane-wave excitation is used whereas in the latter case, port excitations are used with the option of plane waves. Formulation modes include MPIE I or II. Surface boundary condition input can be PEC or impedance boundary condition (IBC). Basis mode represents usage of RWG

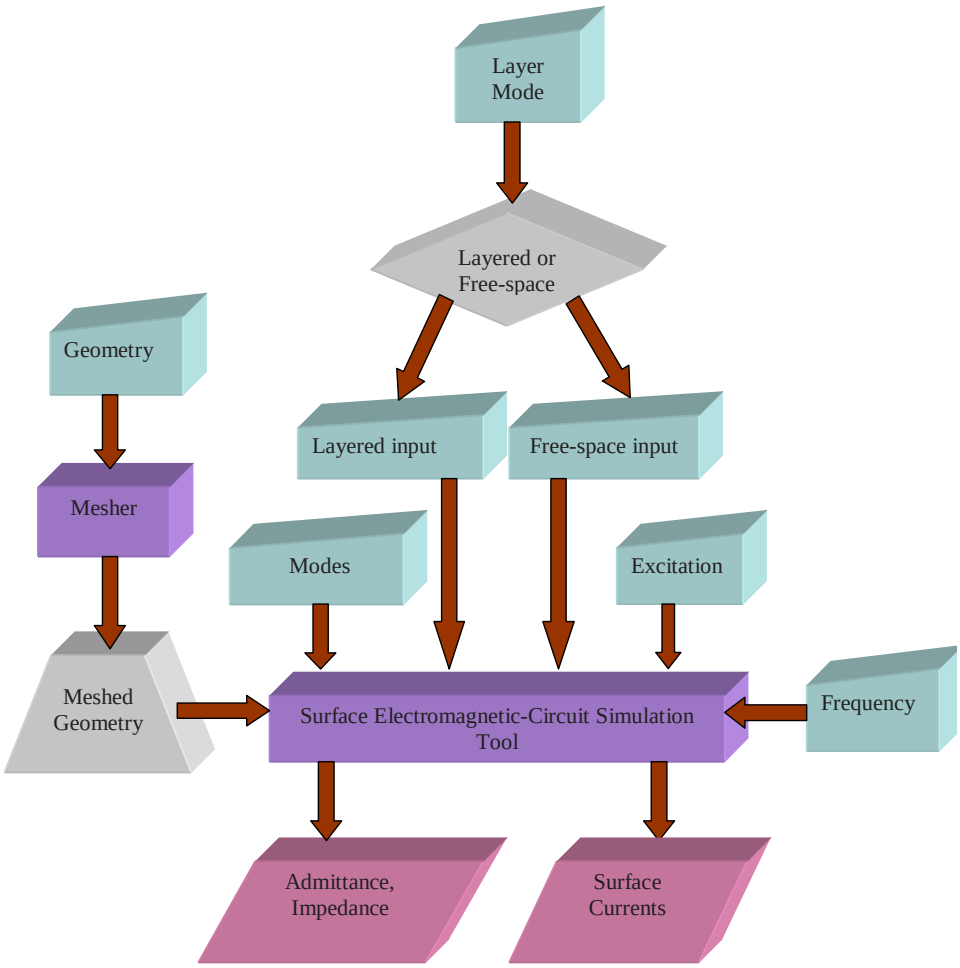

Fig. 11. Flow diagram

or LS functions. Wave mode is used for either full-wave or EMQS free-space Green functions. Note that, not all the combinations of inputs are reasonable. Layered Green functions are already full-wave, therefore there is no EMQS version.

B. System Outputs

The outputs include port admittance or impedance values and surface currents as shown in Fig. 11. When the simulation mode is electromagnetic, only surface currents are produced. In case of electromagnetic-circuit simulation, depending on the

excitation type, port admittance or impedance is produced.

C. Matrix Formation

In this section, the algorithm for matrix formation is presented in Fig. 12 for the proposed surface impedance integral equation method for electromagnetic-circuit simulation of three-dimensional interconnects in layered media. The integrations are computed looping through testing and source elements. Each triangle edge pair interaction is computed and added to 1 and 16 locations in RWG and LS based matrices, respectively. In the case of excitation or right-hand-side vector, contribution from each testing edge is added to four locations with the correct sign in LS method. The advantage of the proposed method is that the integrals and the matrix contributions are computed once for each element pair and edge pair, respectively. Once the contribution for edge pair is computed, it is used for both RWG and LS methods, the main algorithm used for RWG functions does not change when LS functions are used. Computations for the electromagnetic-circuit interface matrices are also handled in the main element loops to avoid extra computational cost. The matrices that are purely based on circuit equations are filled outside the element loop.

Filling in the matrices for LS method is more complicated than the RWG method as shown in Fig. 13. An edge corresponds to two triangles. During the geometry processing, the first encountered edge is assigned the positive edge number whereas the second one is assigned the negative edge number. The sign of the edges are multiplied while filling in the matrix for RWG method. LS method requires both normalization with the testing and the source edge lengths and sign multiplication.

```
foreach testing element m
  foreach source element n
        compute integrals Ia,Ib,Ic for Green functions
        foreach non-boundary testing edge
                find global edge index, loop indices, and star indices
                if (simulation mode == electromagnetic-circuit) then
                        if (n is contact element) then
                                find contact element index
                                compute contribution to sub-matrix C
                                if (basis mode ==  rwg) add  to single location
                                if (basis mode ==  ls) add  to 2 locations
                                if (m is contact element) then
                                        find contact element index
                                        add contribution to sub-matrix F
                                end if
                        end if
                end if
                foreach non-boundary source edge
                        find global edge index, loop indices, and star indices
                        compute contribution to sub-matrix A
                        if (surface boundary condition=ibc) then
                                add contribution to sub-matrix A
                        end if
                        if (basis mode ==  rwg) add contribution to single location
                        if (basis mode ==  ls) add contributions to 16 locations
                        if (simulation mode == electromagnetic-circuit) then
                                if (m is contact element) then
                                        find contact element index
                                        compute contributions to sub-matrix E
                                        if (basis mode ==  rwg) add to single location
                                        if (basis mode ==  ls)
                                                add  to 2 locations for MPIE I
                                                add to 4 locations for MPIE II
                                        end if
                                end if
                        end if
                end
         end
   end
end
if (simulation mode == electromagnetic-circuit) then
        foreach contact
                fill sub-matrices G,L
        foreach port
                fill sub-matrices -Q,-Q^T,R,P
end if
```

Fig. 12. Algorithm for matrix formation

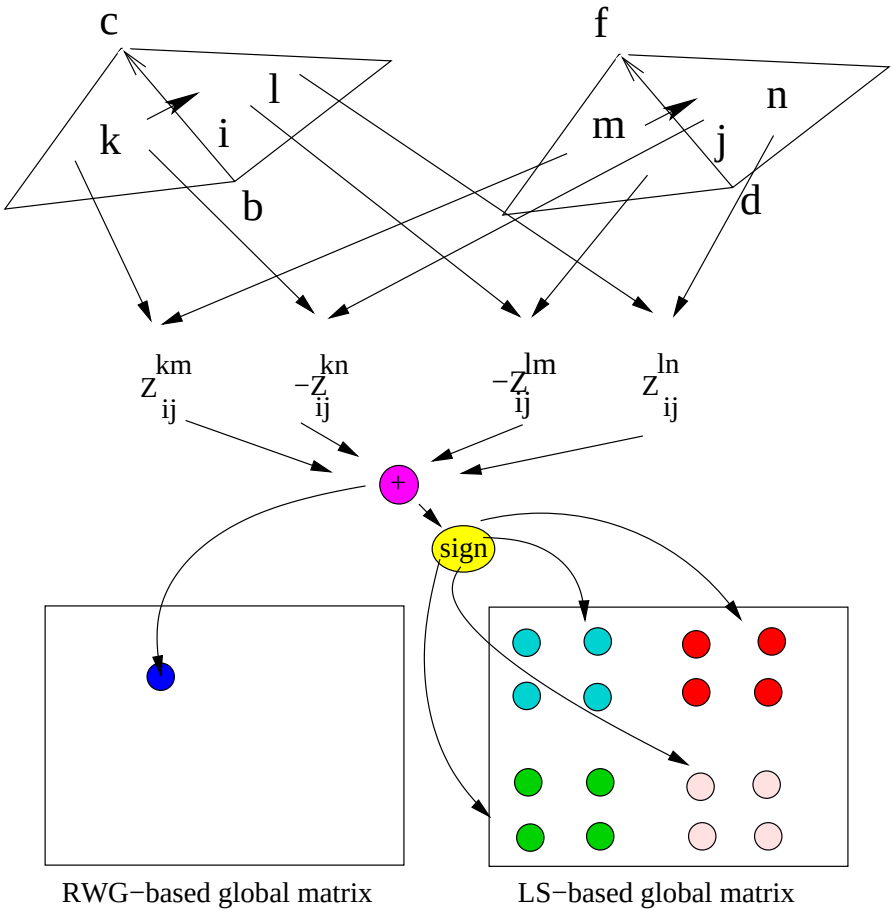

Fig. 13. Illustration of matrix A formation

CHAPTER VI

NUMERICAL RESULTS

In this chapter, the proposed methods are validated with various examples in a systematic way. First, the electromagnetic part of the solution is verified. Then, the low frequency solution for electromagnetic part is validated. After that, the layered kernel computation is tested. Finally, the RWG and LS based solutions for two MPIE forms are evaluated for electromagnetic-circuit simulation and compared to other methods in the literature.

A. Validation of the Electromagnetic Simulation

1. Validation of Different Formulations

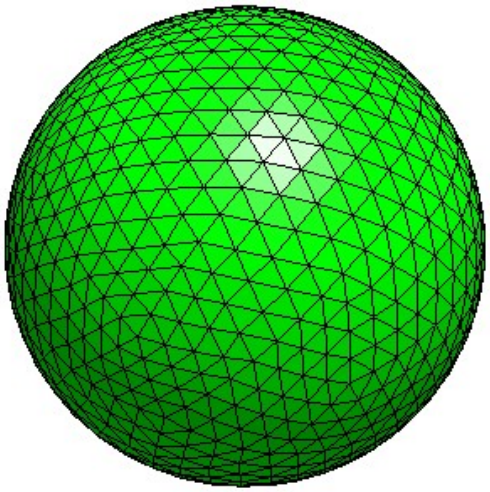

Fig. 14. Sphere

In order to evaluate the electromagnetic part of the method, the accuracy is

validated for the EFIE, the MFIE and the PMCHWT formulations in (4.59), (4.60) and (4.53), respectively. The number of nodes, elements and edges of the discretized sphere in Fig. 14 are 1749, 1856 and 2784, respectively. The electric currents are analyzed and compared for a PEC sphere of radius 0.2λ for a z-directed, y-polarized incident electric field at 300MHz in Figs. 15 and 16. The electric surface currents in Figs. 15 and 16 are consistent between the EFIE and the MFIE formulations based on the RWG basis and testing functions.

The PMCHWT electric and magnetic surface currents are analyzed for a dielectric sphere of permittivity $2\epsilon_0$ and shown in Figs.17, 18, respectively.

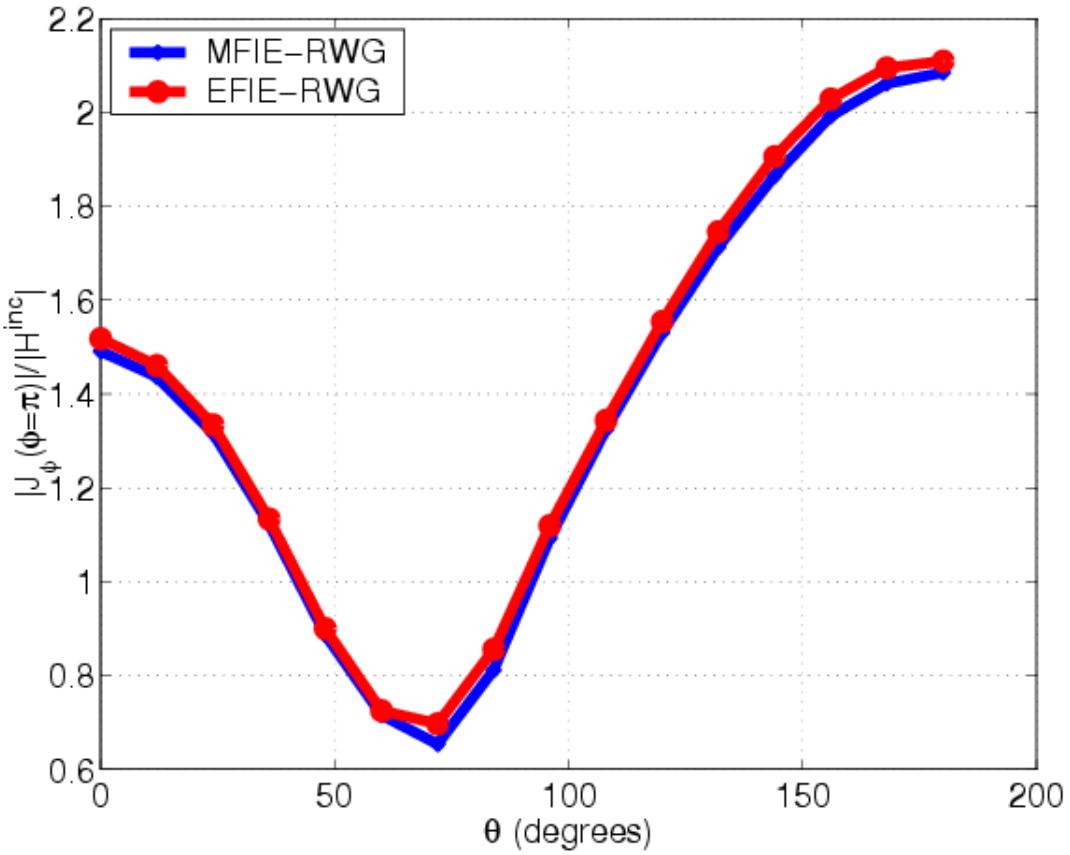

Fig. 15. Normalized current in ϕ direction on a PEC sphere of radius 0.2λ for a z-directed, y-polarized incident electric field

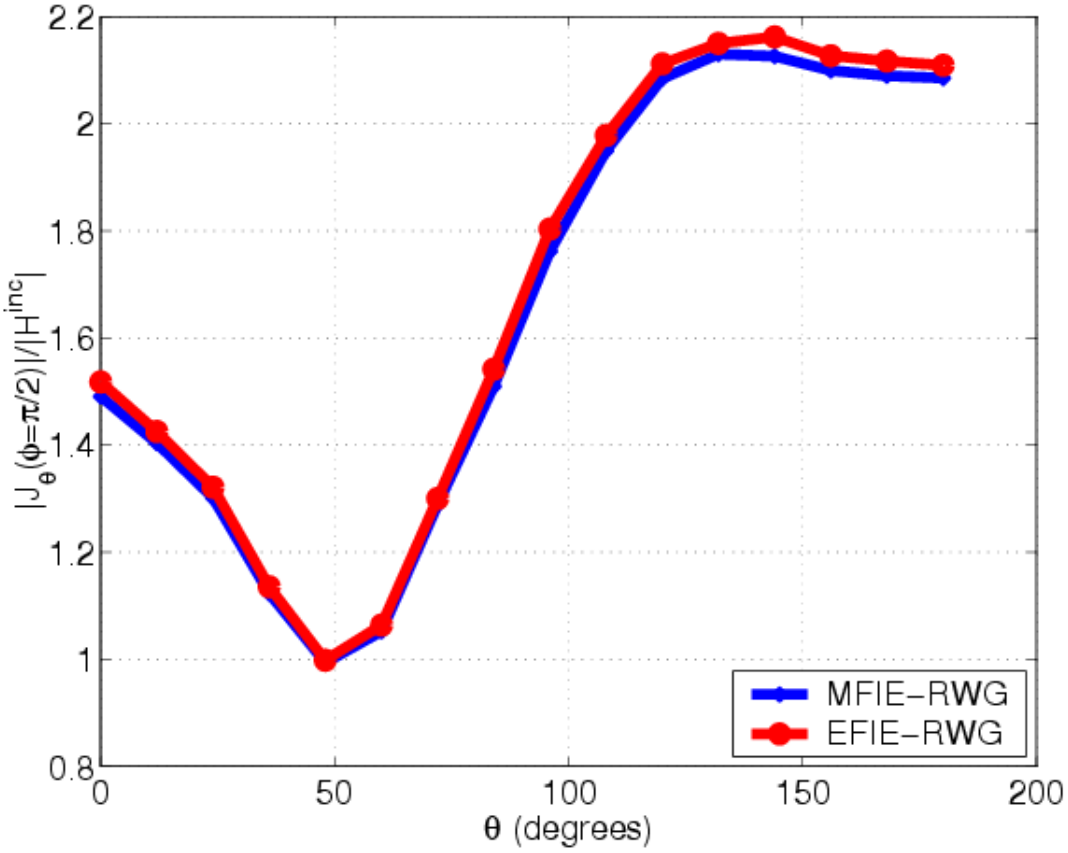

Fig. 16. Normalized current in θ direction on a PEC sphere of radius 0.2λ for a z-directed, y-polarized incident electric field

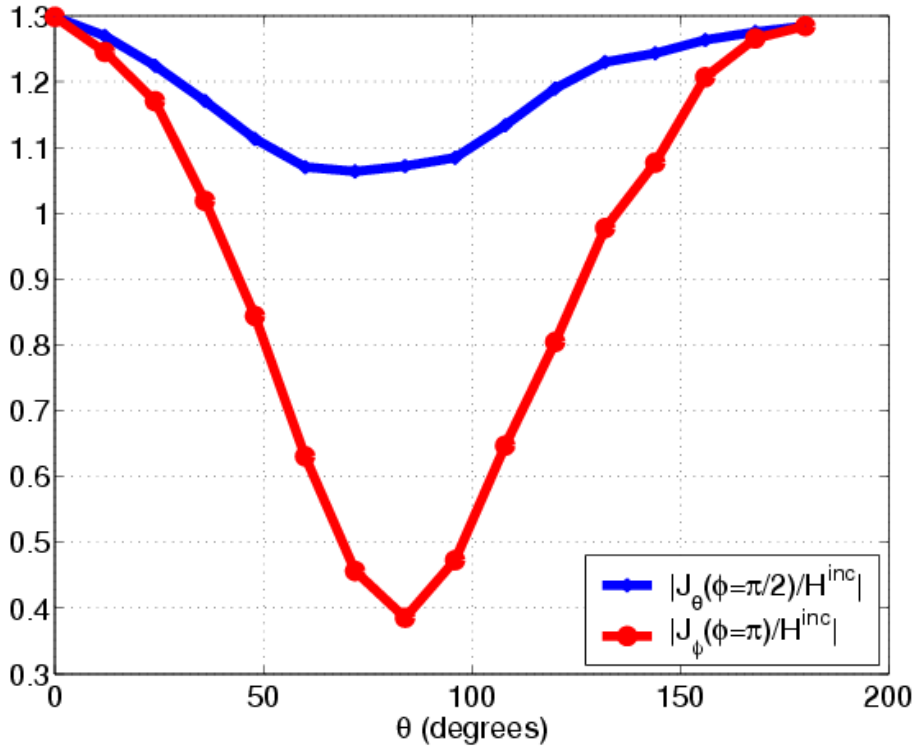

Fig. 17. Normalized electric surface currents on a dielectric sphere of radius 0.2λ for a z-directed, y-polarized incident electric field

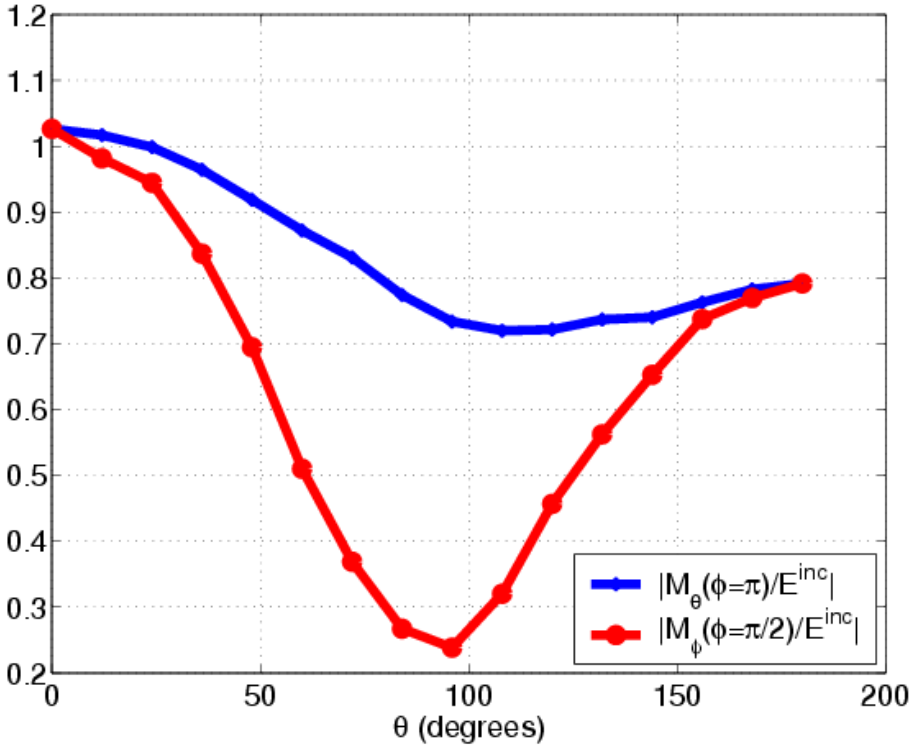

Fig. 18. Normalized magnetic surface currents on a dielectric sphere of radius 0.2λ for a z-directed, y-polarized incident electric field

2. Validation of the Low Frequency Solution for Electromagnetic Simulation

The accuracy of the LS basis and testing functions along with frequency scaling are compared to RWG basis and testing functions with respect to frequency. Note that, the scaling factor in (4.34) is equal to frequency.

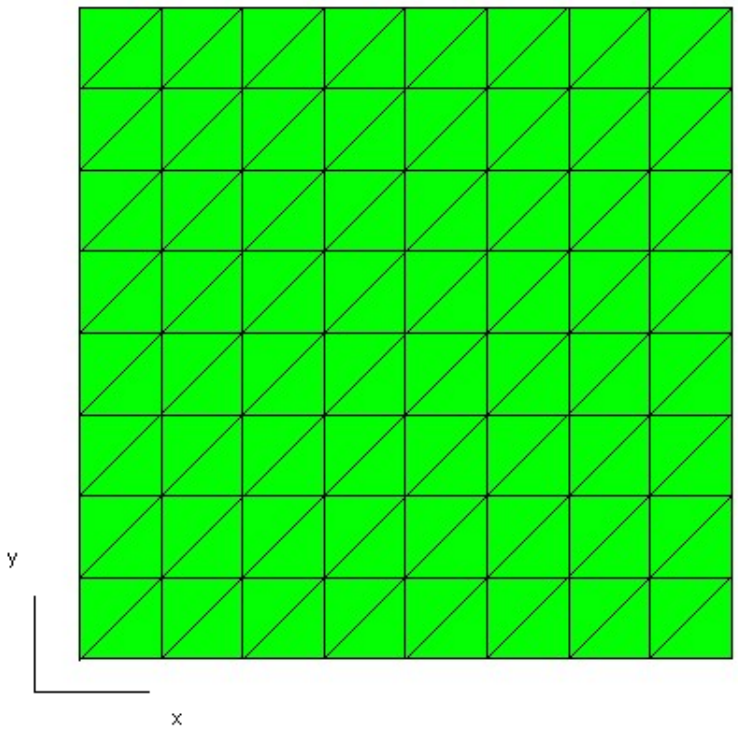

Fig. 19. Meshed plate

A thin PEC plate with width and length of 1m is discretized so that there are 81 nodes, 208 edges, 128 elements as shown in Fig. 19. Incident electric field is z-directed and x-polarized. It is clear from Figs. 20 and 21 that the RWG and the LS functions provide consistent results at 300MHz. However the RWG approach starts to be unreliable at 20Hz as seen in Figs. 22 and 23. Other reason for RWG method providing expected results down to 20Hz is the use of double precision in Fortran90.

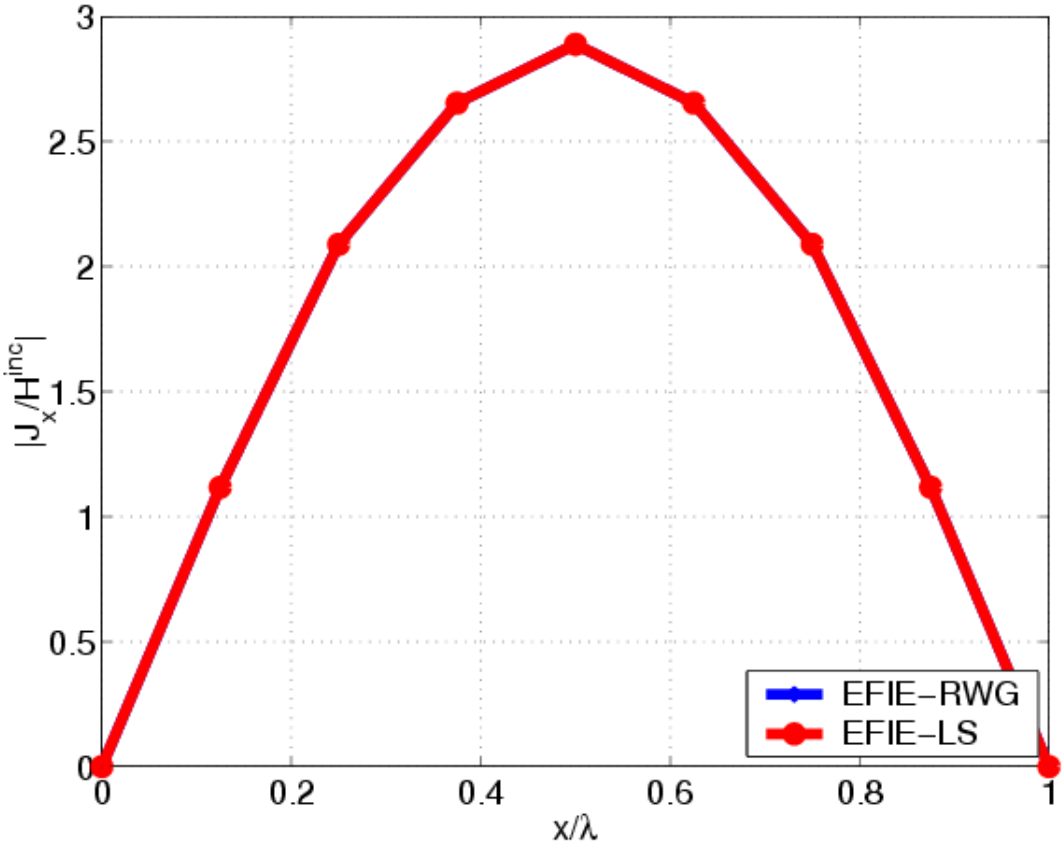

Fig. 20. Normalized current at y cross-section on a thin plate at 300 MHz

Another example for validating low frequency solution is a coarse-meshed PEC sphere as shown in Fig. 24. Surface currents are plotted in Figs. 25 and 26 at 300 MHz. The results at 20Hz are plotted in Figs. 27 and 28. Similar results as in the plate case is observed in the sphere case. RWG and LS results match well at 300MHz whereas RWG results are not reliable at 20Hz.

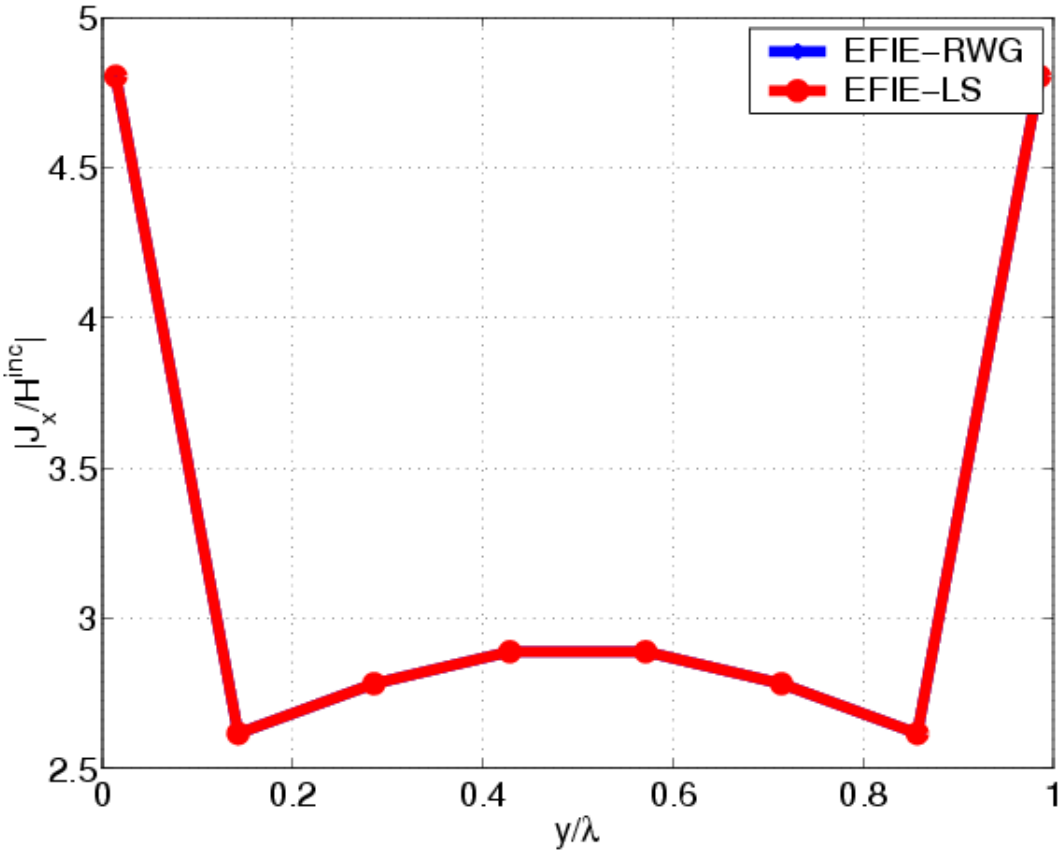

Fig. 21. Normalized current at x cross-section on a thin plate at 300 MHz

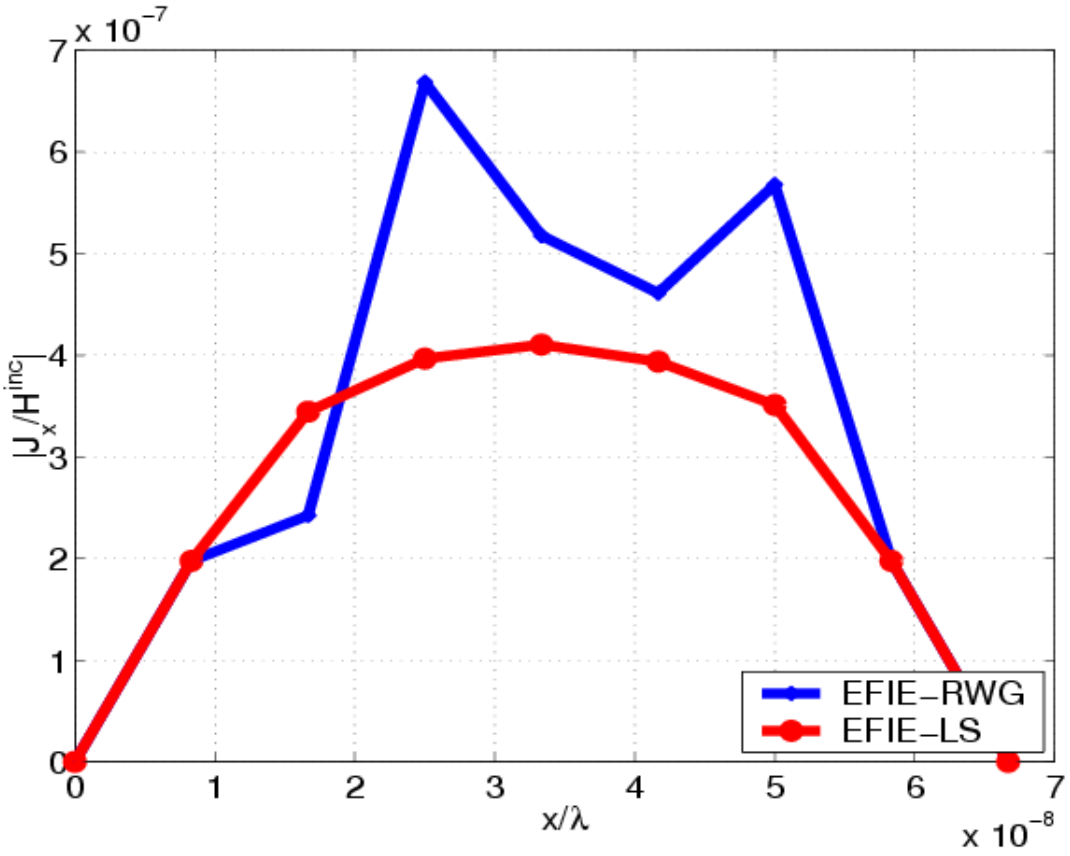

Fig. 22. Normalized current at y cross-section on a thin plate at 20 Hz

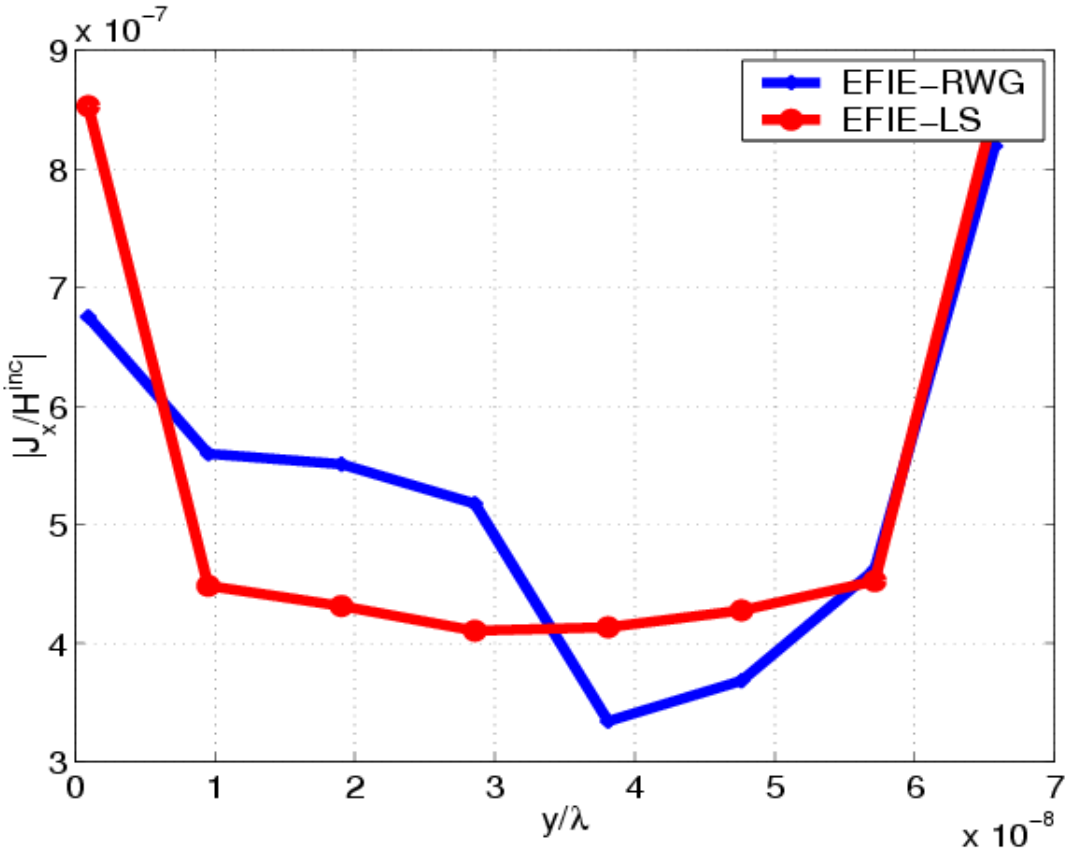

Fig. 23. Normalized current at x cross-section on a thin plate at 20 Hz

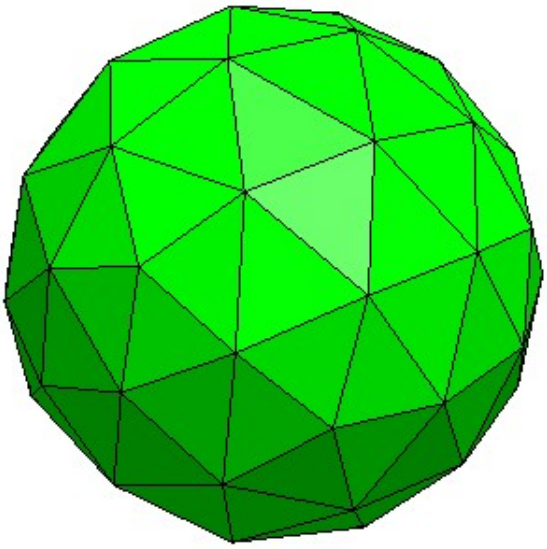

Fig. 24. Coarse-meshed sphere

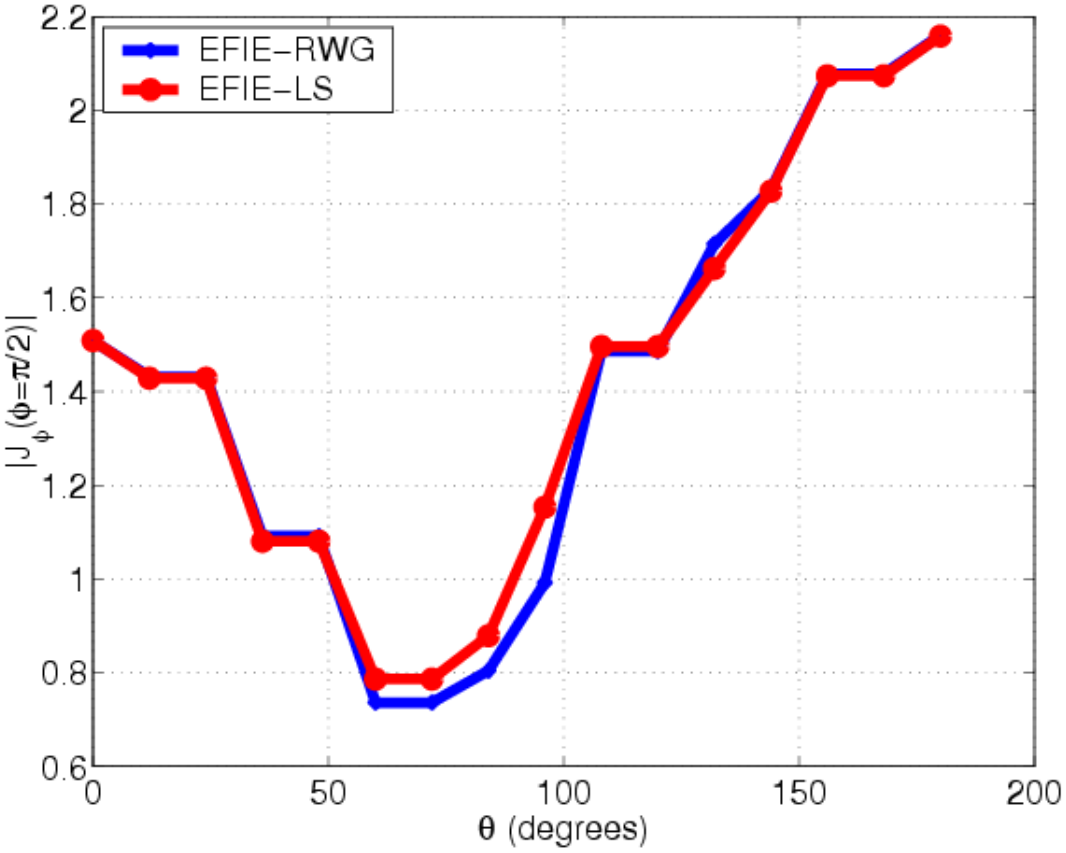

Fig. 25. Normalized current in ϕ direction on a PEC sphere of radius 0.2λ for a z-directed, y-polarized incident electric field at 300Mhz

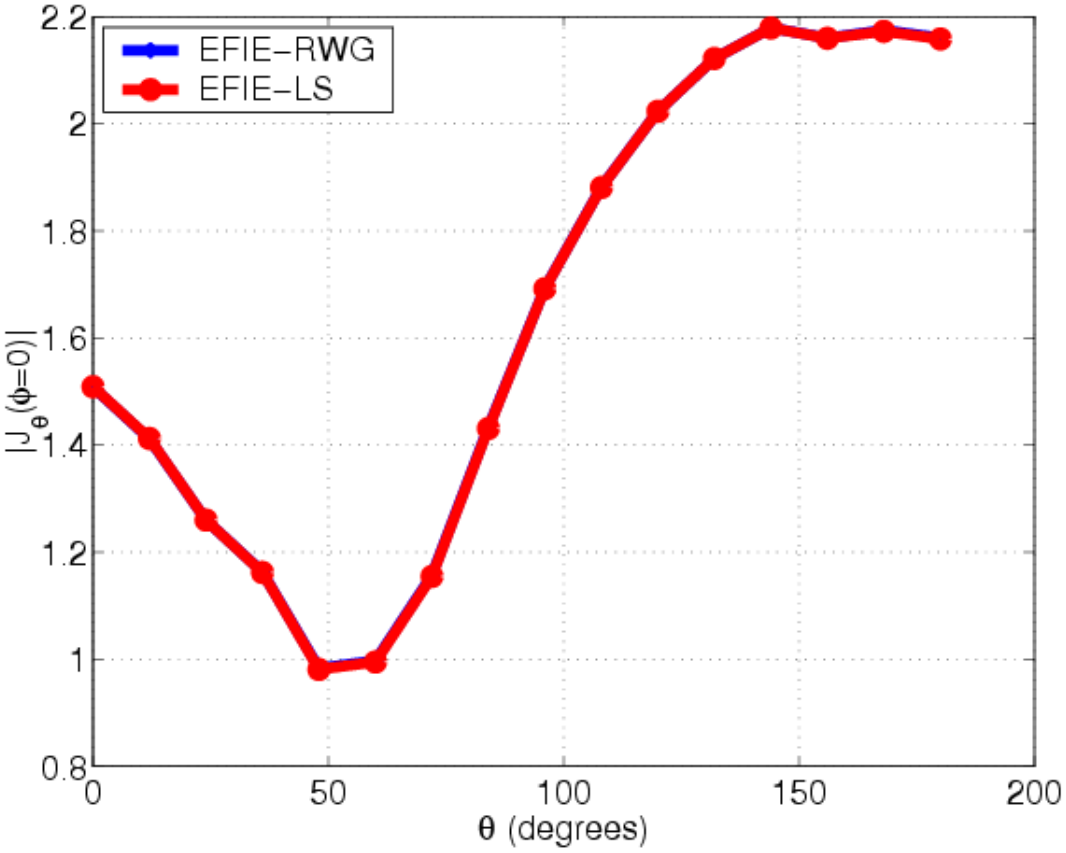

Fig. 26. Normalized current in θ direction on a PEC sphere of radius 0.2λ for a z-directed, y-polarized incident electric field at 300Mhz

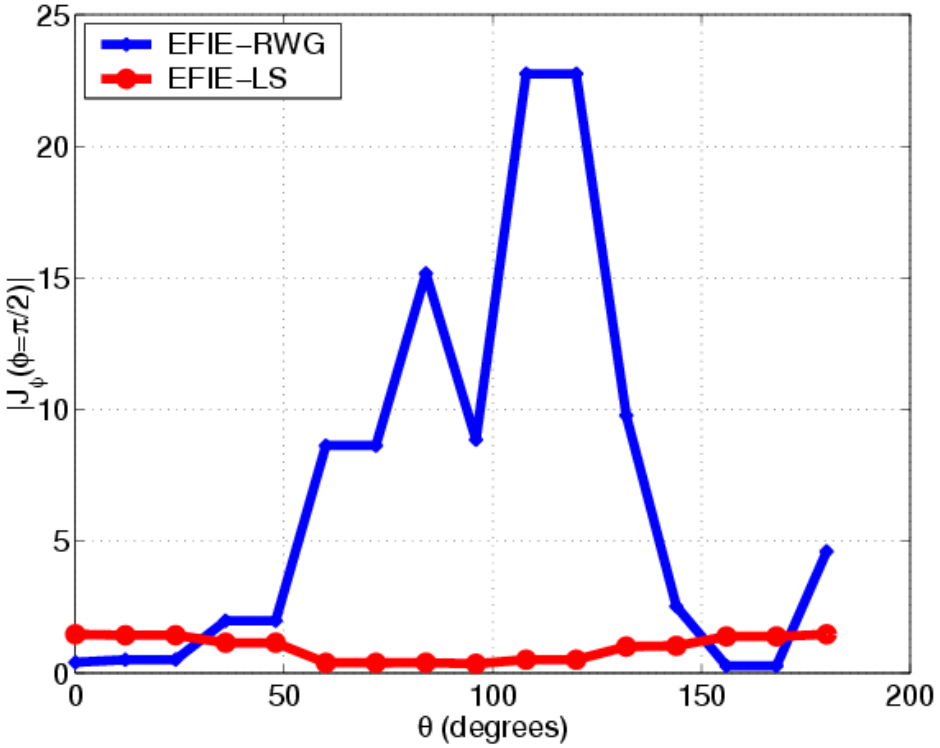

Fig. 27. Normalized current in ϕ direction on a PEC sphere of radius 0.2λ for a z-directed, y-polarized incident electric field at 20 Hz

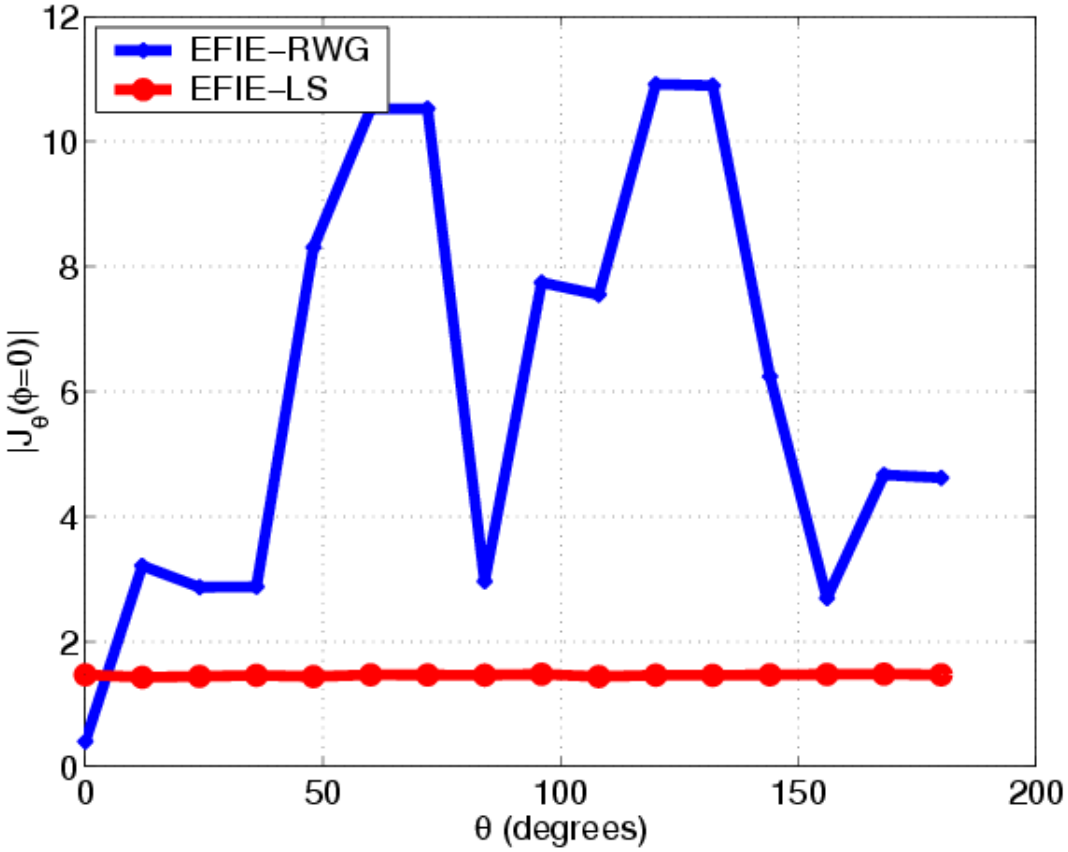

Fig. 28. Normalized current in θ direction on a PEC sphere of radius 0.2λ for a z-directed, y-polarized incident electric field at 20 Hz

B. Validation of the Electromagnetic-Circuit Simulation

1. Validation of the Layered Kernels

Layered kernel implementation is validated using free-space case. This way, the layered kernels in (B.98) and (B.80) can be directly compared to free-space kernel in (1.11). Fig. 29 shows the comparison of the implementation results against (1.11) and [62]. It can be seen that the results match well.

2. Convergence Tests

A 3-D rectangle wire is analyzed using the proposed electromagnetic-circuit simulation method as shown in Fig. 30. The size and the conductivity of the wire is 0.5x0.5x5 mm and $5.8\text{x}10^7$ S/m, respectively.

First of all, convergence tests are performed on the wire for validating the electromagnetic-circuit approach in free-space which are shown in Figs. 31 and 32. Seven different discretizations are applied on the wire where matrix size, N is 58, 70, 73, 189, 403, 529, 647 and the contact element count, N_c is 4, 4, 4, 12, 34, 40, 56, respectively. It is clear from Figs. 31 and 32 that larger R or L values converge to their final values much faster than the smaller values.

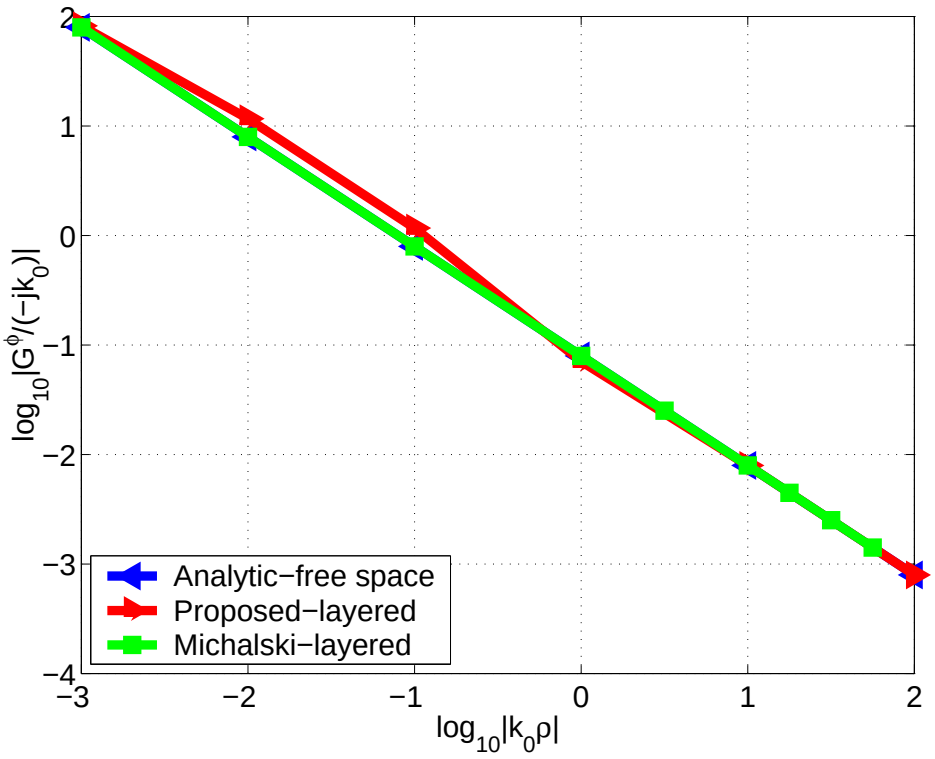

Fig. 29. Kernel comparison in free-space

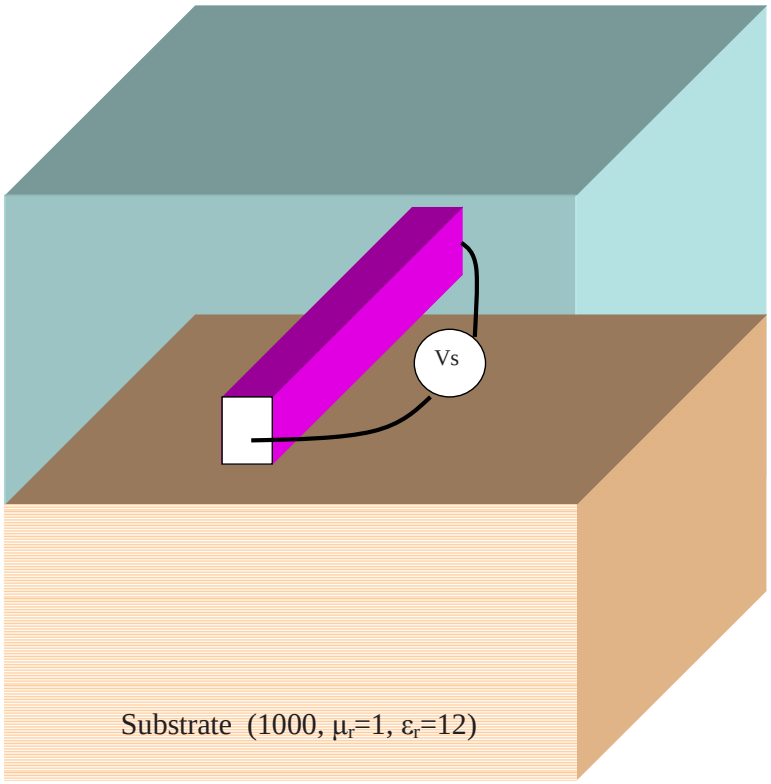

Fig. 30. Single wire over a single substrate layer

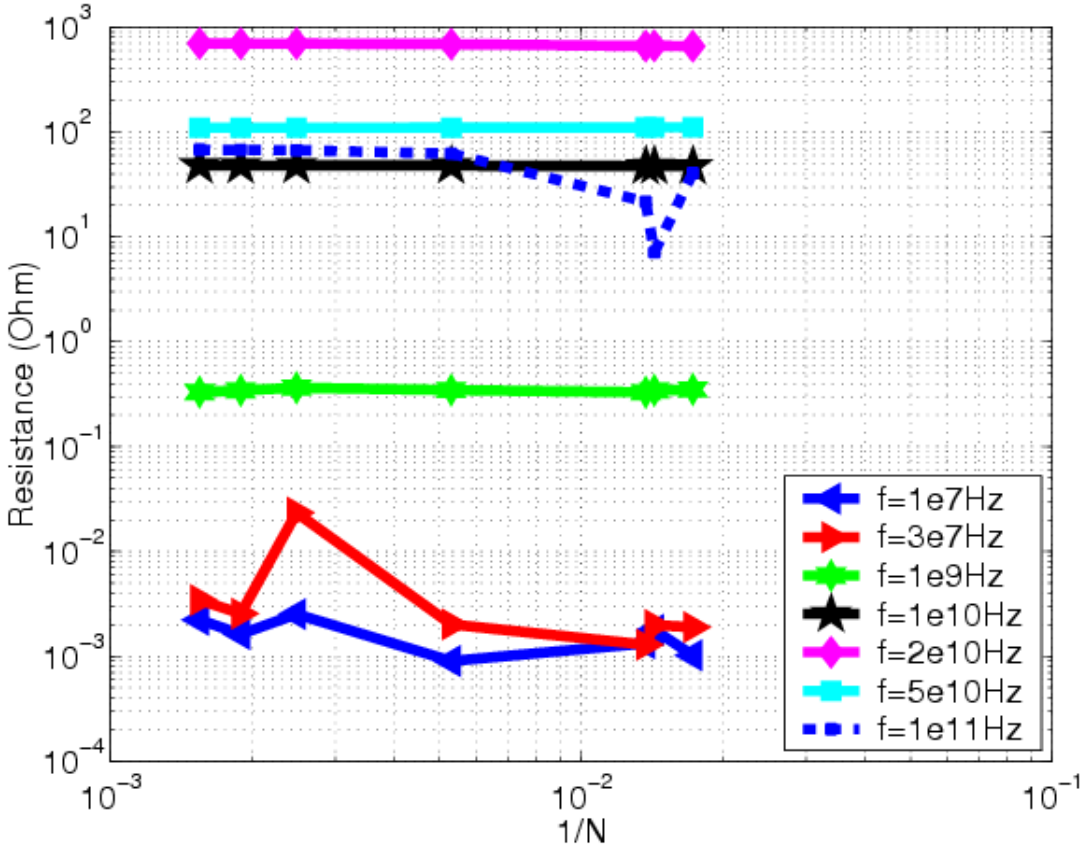

Fig. 31. Resistance vs 1/N for free-space kernel

Then, convergence tests are performed on the wire for validating the electromagnetic-circuit approach in free-space by using layered kernels which are shown in Figs. 33 and 34. Six different discretizations are applied on the wire where matrix size, N is 58, 70, 73, 189, 403, 529 and the contact element count, N_c is 4, 4, 4, 12, 34, 40, respectively. In this case, each value converge about N=403.

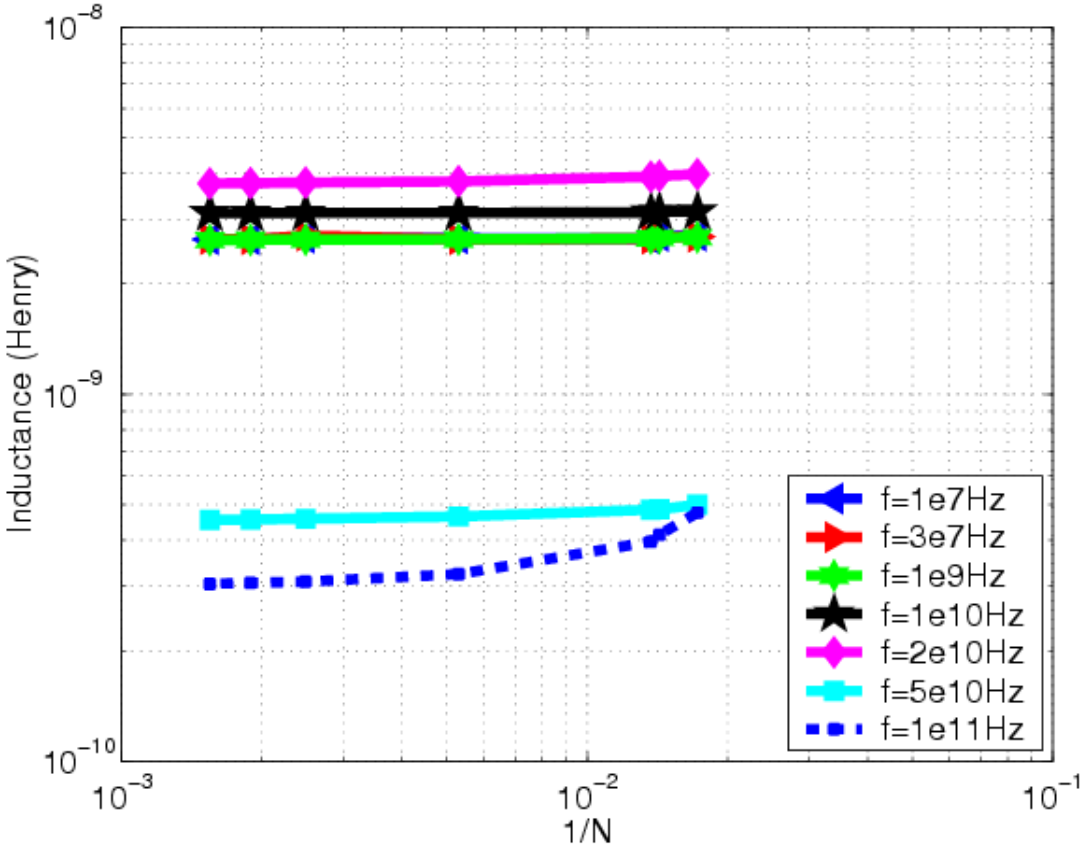

Fig. 32. Inductance vs 1/N for free-space kernel

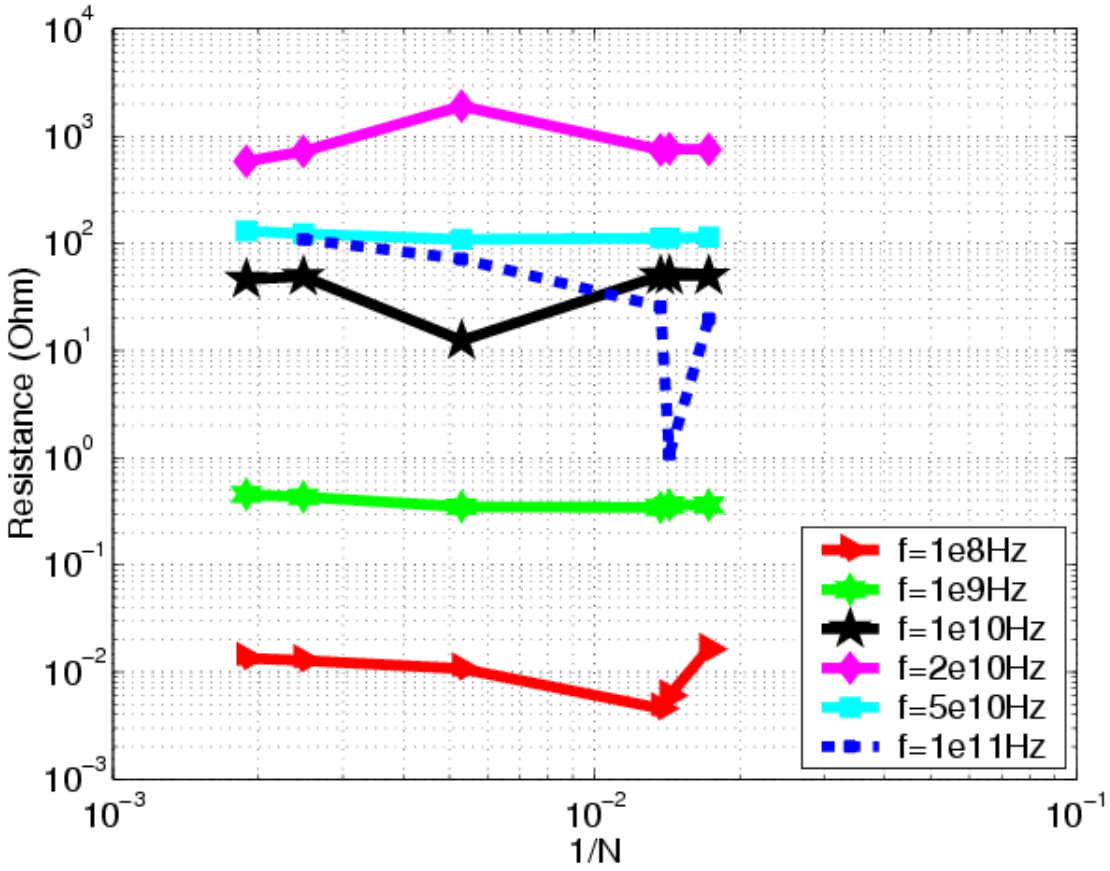

Fig. 33. Resistance vs 1/N for layered kernels

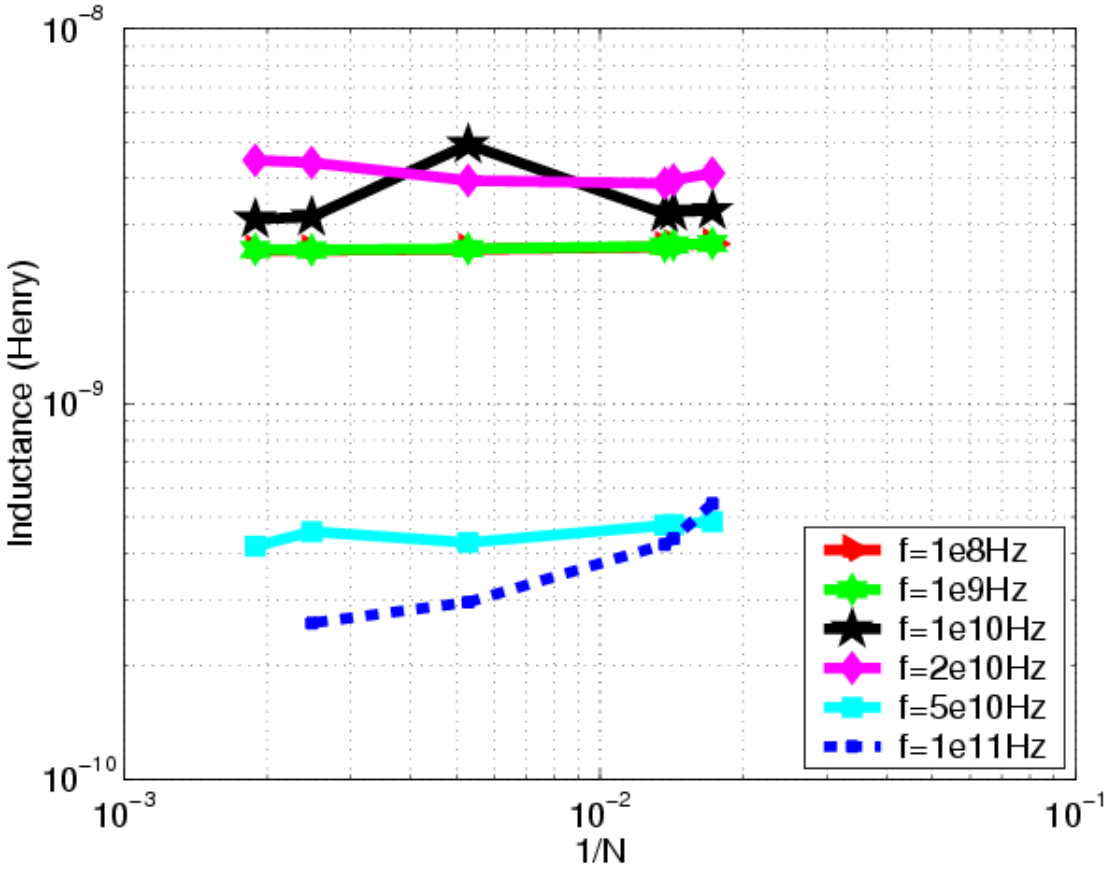

Fig. 34. Inductance vs 1/N for layered kernels

After that, the wire is placed over a substrate as in Fig. 30 and analyzed using layered kernels. The resistance and the inductance of the wire is analyzed with respect to frequency for three conditions: EMQS and full-wave (FW) modes in free-space and FW mode over the substrate denoted as FS-EMQS, FS-FW, and SUB-FW, respectively. It can be seen from Figs. 35 and 36 that FS-EMQS and FS-FW results match well with FI-FS-EMQS [17] and CJ-FS-FW [20], respectively. It is important to note that FS-EMQS results become unreliable beyond the frequency of 30 MHz compared to FS-FW.

Since FastMaxwell supports only one substrate layer, a single substrate $1\mu m$ below the wire with conductivity of $1000\frac{S}{m}$ and dielectric constant of 12 is simulated as shown in Fig. 30. Our and FastMaxwell results are denoted as SUB-FW and FM-SUB-FW, respectively, in Figs. 35 and 36. Despite the differences in the discretization, SUB-FW and FM-SUB-FW frequency behaviors are consistent. When the substrate is absent and present, the inductance is constant until 10GHz and 1GHz, respectively. This implies that the presence of substrate shortens the frequency range where the quasi-static inductance values are acceptable. It can also be observed that the resistance is larger until 2GHz and the inductance is smaller when the substrate is introduced.

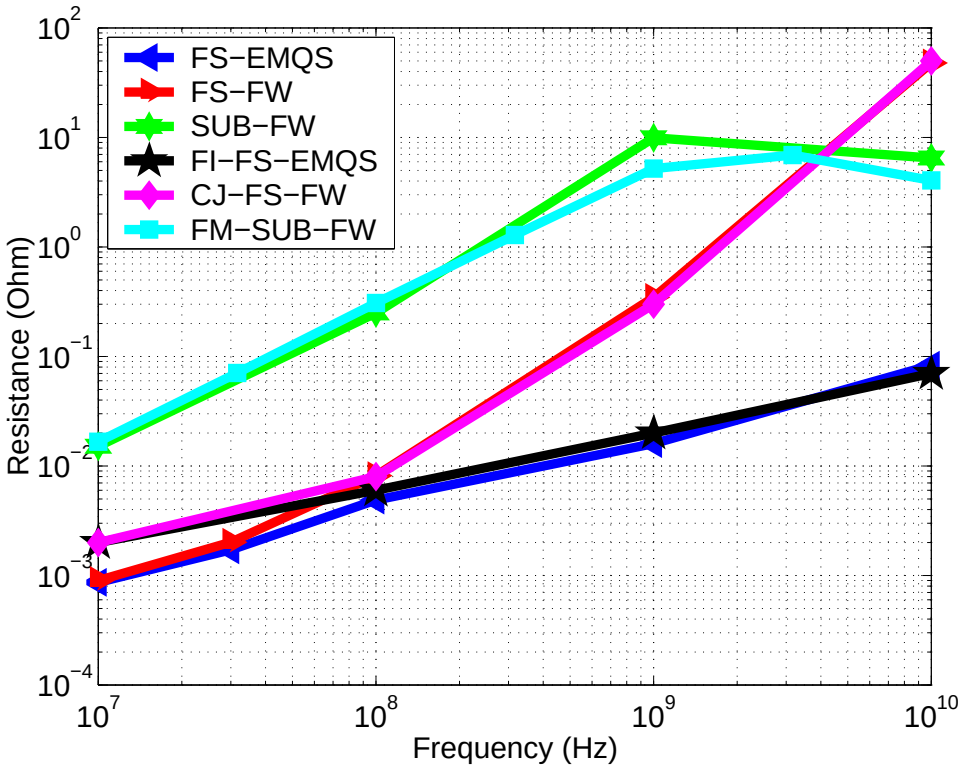

Fig. 35. Resistance vs frequency

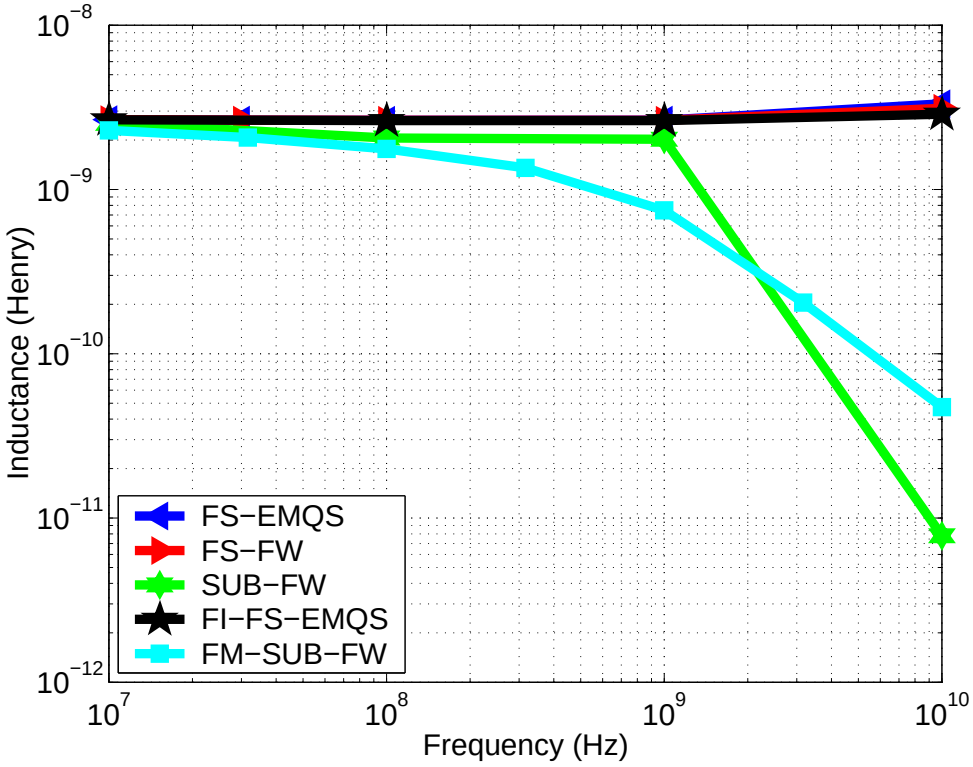

Fig. 36. Inductance vs frequency

4. Detailed Analysis of the Solutions

The normal contact currents and the edge currents are analyzed for the single wire at 1GHz in free-space and over single substrate layer. Note that, the size of the matrix and the contact element count are 189 and 12, respectively.

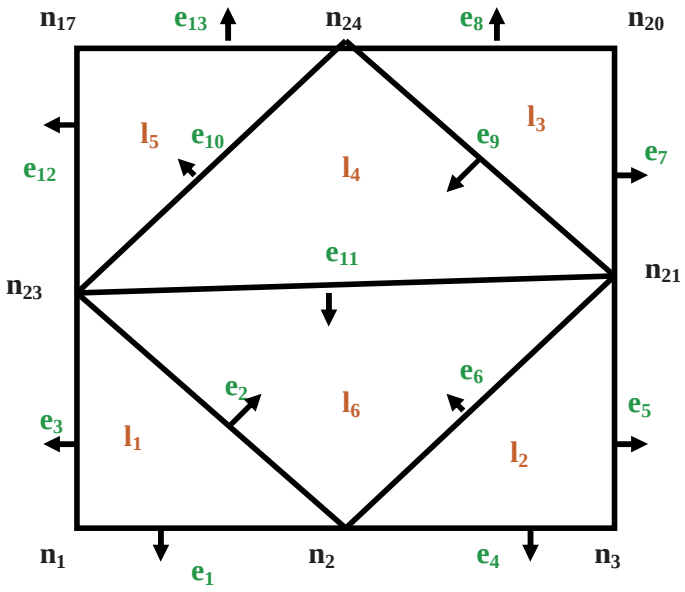

Fig. 37. Illustration of nodes, edges and elements at the first contact

The element and the edge numbers of the first contact is depicted in Fig. 37. Note that, each arrow represents the edge reference current direction.

The normal currents at each contact element for free-space are summarized in Table I. The normal current values at the outer elements are all equal and larger in magnitude compared to the inner elements. The normal current at the inner elements, l_4 and l_6 are in the opposite direction of the currents at the outer elements.

Table I. Normal current solution at the first contact elements at 1GHz in free-space

Contact elements	Normal current, K_{l_j}
l_1	4e-4 - 0.02i
l_2	4e-4 - 0.02i
l_3	4e-4 - 0.02i
l_4	-2e-4 + 0.01i
l_5	4e-4 - 0.02i
l_6	-2e-4 + 0.01i

Table II. Edge currents at the first contact edges at 1GHz in free-space

Contact edges	Edge current, J_{e_j}
e_1	0.629348667626423 - 29.7775589862608i
e_2	0.277399074824135 - 13.5299136876587i
e_3	0.645136745840424 - 30.4569194174933i
e_4	0.634942030052991 - 30.0162552388967i
e_5	0.627859082579790 - 29.8334212704605i
e_6	0.270126214896339 - 13.4905271467228i
e_7	0.630956331327895 - 29.8463589334680i
e_8	0.648233573916082 - 30.5626890908994i
e_9	0.287978699485261 - 13.9303276867932i
e_{10}	-0.287448236475236 + 13.8485300882827i
e_{11}	-0.007157535728994253 + 0.327810315539969i
e_{12}	0.641305896875261 - 30.2929616636587i
e_{13}	0.636856138751637 - 30.1535762138571i

The edge currents at the first contact in free-space are summarized in Table II. The currents at outer edges are the same and larger than the currents at the inner edge currents. These results are expected since the current flows close to the surface of the conductor due to the skin effect at high frequencies.

Table III. Normal current solution at the first contact elements at 1GHz over substrate

Contact elements	Normal current, K_{l_j}
l_1	1.786374781462120E-002 - 3.863161179403857E-003i
l_2	1.953973882874904E-002 - 3.891155837521129E-003i
l_3	4.155314932274268E-003 - 2.231602719805836E-002i
l_4	-1.121840334356842E-003 + 1.031077549427729E-002i
l_5	5.119839512562709E-003 - 2.669399294027297E-002i
l_6	-7.380770998758337E-003 - 2.308574333292104E-003i

The normal currents at each contact element in the presence of a substrate are summarized in Table III. As seen in the table, the substrate caused the normal currents at l_3 and l_5 to be larger than l_1 and l_2. The outer elements still has larger current values compared to inner elements. The currents at outer and inner elements are in opposite directions. The normal current at l_4 is also larger than the one at l_6 due the presence of the substrate.

Table IV. Edge currents at the first contact edges at 1GHz over a substrate

Contact edges	Edge current, J_{e_j}
e_1	42.7495551166481 - 9.88633987176484i
e_2	8.53664360297934 + 6.48575629986297i
e_3	15.7733799360188 - 14.7343120622190i
e_4	35.1804688396258 - 7.92645561326690i
e_5	20.0366109991670 - 18.1659703396686i
e_6	17.3465085398526 + 7.25789383298187i
e_7	10.9540543994231 - 39.2434524233143i
e_8	8.71625718302248 - 32.9083096945065i
e_9	-2.12725306686258 - 12.3379673235612i
e_{10}	-0.553931415741109 + 23.5548220319840i
e_{11}	-3.34099935967673 - 5.03737783280081i
e_{12}	12.2985353168718 - 47.8787734857099i
e_{13}	7.04113827690358 - 23.7228166306437i

The edge currents at the first contact in the presence of a substrate are summarized in Table IV.

5. Comparison of Two MPIE Forms

Impedance values for two forms of MPIE using RWG method, (4.8) are compared in Table V. Note that, the same mesh is used for both cases where the matrix size, N is 189. The substrate has the same parameters as in Fig. 30.

Table V. Comparison of wire impedance for MPIE form I and II using RWG method

GHz	Form I (Ω)	Form II (Ω)	$\frac{\lvert FormII\rvert - \lvert FormI\rvert}{\lvert FormI\rvert}$ (%)
0.01	0.0152 + 0.1587i	0.0161 + 0.1594i	0.5
0.1	0.2501 + 1.2924i	0.2523 + 1.2942i	0.2
1	9.9282 + 12.7142i	9.9165 + 12.7159i	-0.04
10	6.5038 + 0.4896i	6.4322 + 0.404i	-1.2

Table VI. Analysis of different excitations

Excitation Type	Output	Value
Unit voltage at the port	Admittance	1.2736E-003 - 6.0208E-002i
Unit current at the port	Impedance	0.3512 + 16.6017i
Unit voltage at terminal 1	Terminal currents	$\mp$ 1.2699E-003 $\pm$ 6.0033E-002
Unit current at terminal 1	Voltage at terminal 1	-29.8780-1427.6176
Unit current at terminal 1	Voltage at terminal 2	-30.0536-1435.9187

6. Validation of Different Excitations

Four different excitations are applied to the single wire in Fig. 30 at 1GHz in free-space. The wire is discretized such that the total and contact element counts are 116 and 12, respectively. The edge, terminal and port counts are 174, 2, and 1, respectively.

In the first two runs, port voltage and current excitations are applied between the end terminals where the size of the matrix is 192. In the second two runs, unit voltage and current excitations are applied at one of the terminals while the other terminal is grounded or open-circuit. In this case, the matrix size is 190. The results of each run is summarized in Table VI. It is shown that with different port excitations, we can directly obtain the port impedances or admittances. The impedance value obtained by port current excitation is in fact equal to the inverse of the admittance value obtained by port voltage excitation. It is also observed that the terminal currents for terminal voltage excitation are very close to the admittance value obtained by port voltage excitation. In the fourth case, applying a unit current at a terminal and

Table VII. Comparison of wire admittance for RWG and LS methods

GHz	RWG method ($\mho$)	LS method ($\mho$)	$\frac{\lvert LS\rvert-\lvert RWG\rvert}{\lvert RWG\rvert}$ (%)
0.01	7.396669e-2-5.908493i	7.3966636e-2-5.908491i	-0.3479e-4
0.1	3.51152989e-3-0.5959337i	3.511529807e-3-0.5959336i	-0.1482e-4
1	1.2498777e-3-5.963262e-2i	1.2498774e-3-5.963261e-2i	-0.1491e-4
10	1.1550388e-3-4.793215e-3i	1.15503834e-3-4.793214e-3i	-0.3179e-4

open-circuit the other one, produced close voltage values at each terminal.

7. Validation of the Low Frequency Solution for Electromagnetic-Circuit Simulation

First, the low frequency solution is verified in free-space for the electromagnetic-circuit simulation. Note that, the scaling factors are set to 1 in (4.34) and (4.43). Table VII contains the comparison of the single wire admittance due to RWG and LS methods for a coarsely meshed single wire where the matrix size is 70. It is observed that both methods return almost the same values for the frequencies between 0.01 and 10GHz as expected.

Next, the low frequency solution for MPIE form II in (4.43) is compared against RWG method in (4.8). Impedance values for a wire over a single substrate are shown in Table VIII. Note that, the same mesh is used for both cases where the matrix size, N is 189. The substrate has the same parameters as in Fig. 30.

Table VIII. Comparison of wire impedance for MPIE form II using RWG and LS methods

GHz	RWG (Ω)	LS (Ω)	$\frac{\|LS\|-\|RWG\|}{\|RWG\|}$ (%)
0.01	0.0152 + 0.1587i	0.0155 + 0.1578i	-0.5437
0.1	0.2501 + 1.2924i	0.2489 + 1.293i	0.0275
1	9.9282 + 12.714i	9.9197 + 12.725i	0.0213
10	6.5038 + 0.4896i	6.433 + 0.404i	-1.1734

8. Analysis of Two Wires

A second wire is added next to the wire in the first example at a distance of 0.5mm as shown in Fig. 38. Two wires are analyzed in both free-space and over a lightly-doped substrate using free-space and layered kernels, respectively. The voltage is applied at the first port which connects the front contacts of the wires in Fig. 38. The discretized wires have 339 edges, 24 contact elements and ports connecting the contacts at the ends of the wires. The admittance of the first port is analyzed. The back plane below the substrate layers is considered to be a PEC and the two substrate layers are modeled as lossy layers with thicknesses of 400μm and 1μm and the conductivities of 5 S/m and 1000 S/m, respectively. Dielectric constants and permeabilities of both substrate layers are 12 and that of free-space, respectively. The region above the substrate layers is considered to be free-space.

Magnitude of real and imaginary parts of the admittance at the excitation port are plotted in Figs. 39 and 40 for three modes: EMQS and FW modes in free-space and FW mode in the presence of the lightly doped substrate. As observed in the single wire case, FS-FW admittance results depart from FS-EMQS results at a large frequency which is 1 GHz in this case. It is also observed that the presence of the substrate affects both real and imaginary parts. As seen in Fig. 39, real part becomes constant after 0.1GHz. Imaginary part diverges from free-space solution at 1GHz in Fig. 40.

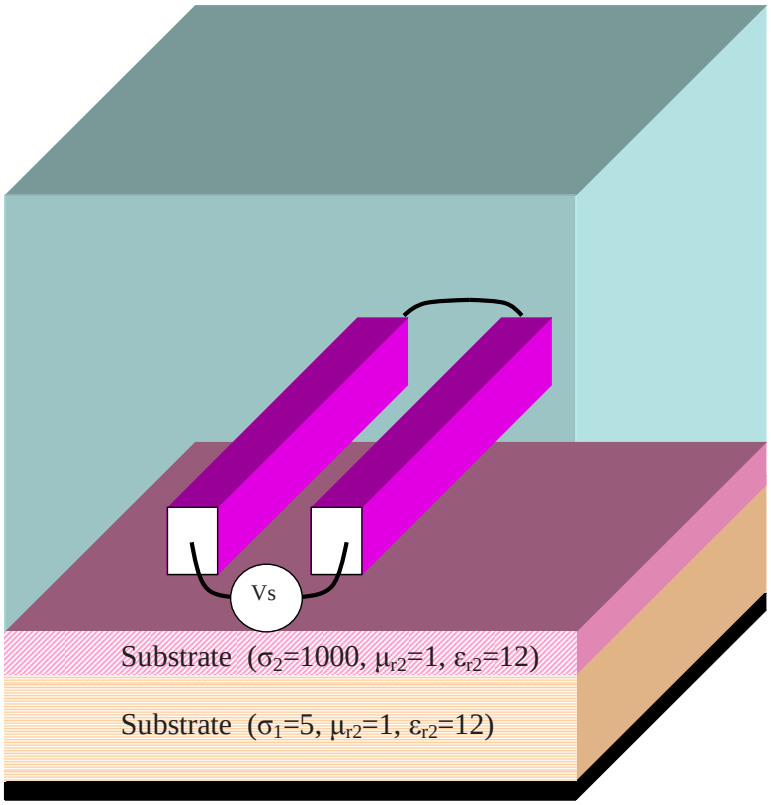

Fig. 38. Two wires over lightly doped substrate

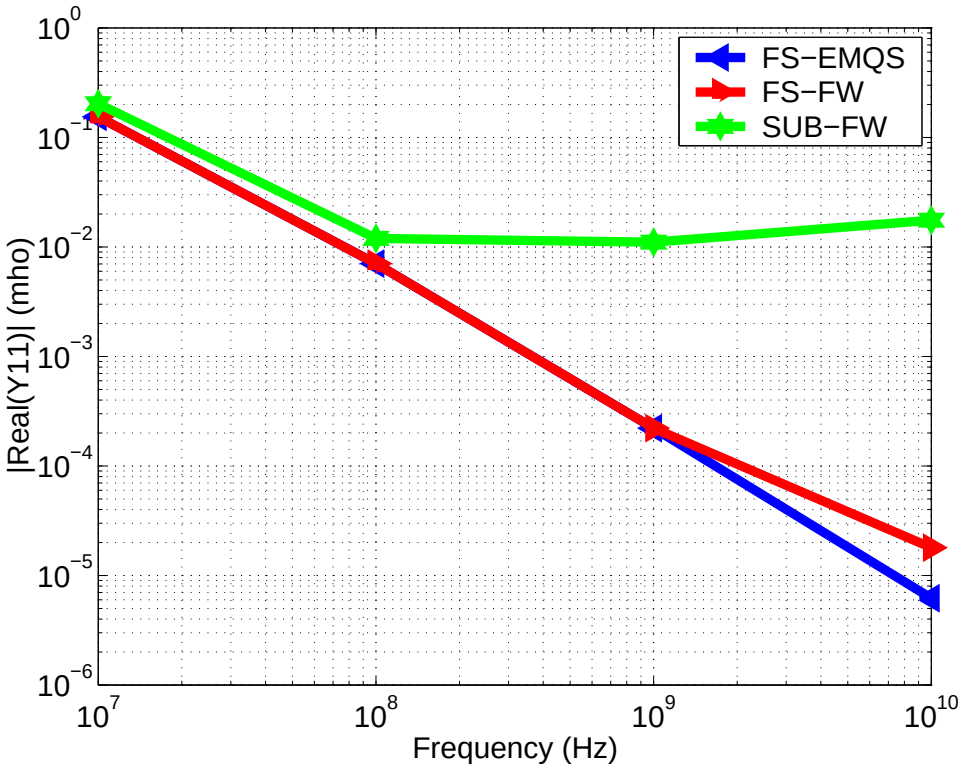

Fig. 39. Real part of admittance at the excitation port

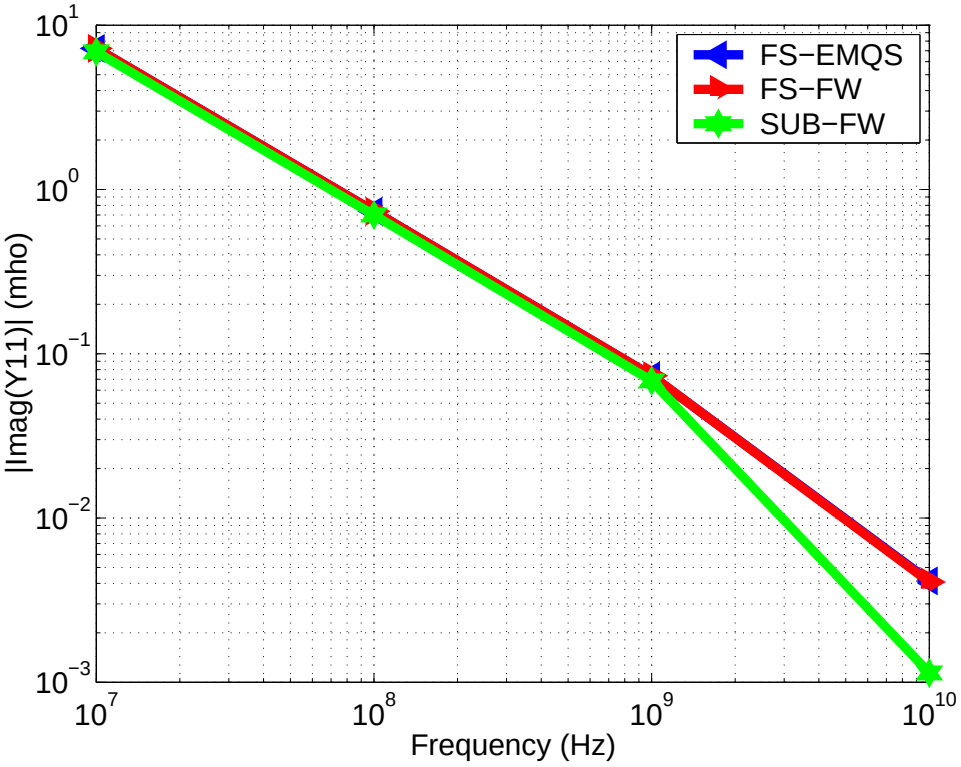

Fig. 40. Imaginary part of admittance at the excitation port

CHAPTER VII

CONCLUSION AND FUTURE WORK

A new full-wave, surface impedance integral equation method is presented for parasitic extraction of 3-D arbitrary-shaped homogeneous objects in layered media. Two MPIE forms of EFIE are used along with the Michalski-Mosig formulations for electromagnetic interactions of 3-D interconnects in layered media over a conducting substrate.

New approach for incorporating LS basis and testing functions to RWG MOM framework is introduced to address the low frequency problem. New low frequency solutions are introduced for electromagnetic-circuit simulation using two MPIE forms. Proposed methods are validated in both electromagnetic and electromagnetic-circuit simulations.

Port and terminal excitations for electromagnetic-circuit simulation are elaborated in detail. The advantage of the proposed method is that there is no need for model order reduction unlike PEEC methods. Another advantage of the proposed method is that there is no need to compute the whole impedance or admittance matrix to compute a single port admittance or impedance, respectively.

The accuracy of the proposed electromagnetic-circuit simulation of 3-D interconnects is validated against references in both free-space and layered media. High frequency behavior of interconnects is analyzed using full-wave kernels and in the presence of conducting substrate layers.

Proposed method meets the needs of parasitic extraction in terms of providing port impedance or admittance as output. It is also possible to post-process the surface currents to obtain the electromagnetic fields exterior to conductors. Interior fields are not of practical concern, however one extension of the proposed electromagnetic-

circuit simulation method is to advance the generic SIE method in homogeneous media with two MPIE forms along with layered kernels and low frequency solutions.

The accuracy of the proposed method has been the major goal of this dissertation, therefore there was not as much emphasis on the performance aspect. This part of the problem can be addressed by incorporating fast iterative and matrix-vector multiplication methods for solving larger interconnect problems in layered media.

REFERENCES

[1] A. E. Ruehli and A. C. Cangellaris, "Progress in the methodologies for the electrical modeling of interconnects and electronic packages," *Proc. IEEE*, vol. 89, no. 5, pp. 740–771, May 2001.

[2] N. Kurt-Karsilayan, "Generic modeling of nonplanar dielectrics for 2 1/2d parasitic extraction," in *Proc. of the Fifth Int. Workshop on System-on-Chip for Real-Time Applicat.*, Banff, AB, Canada, July 2005, pp. 64–69.

[3] Z. Ren, H. Hegazy, and N. Kurt-Karsilayan, "Characterization of dynamic substrate macro-model in mixed signal IC systems using 3-D finite element method," *IEEE Trans. Magn.*, vol. 44, no. 6, pp. 1466–1469, June 2008.

[4] R. Gharpurey, "Modeling and analysis of substrate coupling in integrated circuits," Ph.D. dissertation, Dept. of Elec. Engin. and Compu. Sci., Univ. Cal., Berkeley, 1995.

[5] R. Harrington, *Time-harmonic Electromagnetic Fields*. Piscataway, NJ: IEEE Press, Wiley Interscience, 2001.

[6] N. Morita, N. Kumagai, and J. Mautz, *Integral Equation Methods for Electromagnetics*. Norwood, MA: Artech House, 1990.

[7] A. J. Poggio and E. K. Miller, "Integral equation solutions of three-dimensional scattering problems," in *Comput. Techniq. for Electromagn.* Oxford and New York: Hemis. Pub. Corp., pp. 159–264.

[8] U. Choudhury and A. Sangiovanni-Vincentelli, "Automatic generation of analytical models for interconnect capacitances," *IEEE Trans. Comput.-Aided Design Integr. Circuits Syst.*, vol. 14, no. 4, pp. 470–480, Apr 1995.

[9] J. Cong, L. He, A. B. Kahng, D. Noice, N. Shirali, and S. H.-C. Yen, "Analysis and justification of a simple practical 2 1/2-D capacitance extraction methodology," in *Proc. Design Automa. Conf.*, Anaheim, CA, June 1997, pp. 627–632.

[10] Z. Ren and J. Falbo, "Parasitic extraction of IC interconnects in consideration of optical distortion by using shape sensitivity modeling," in *12th Biennial IEEE Conf. on Electromagn. Field Computa.*, Miami, FL, 2006, pp. 347–347.

[11] S. Kapur and D. E. Long, "IES3: Efficient electrostatic and electromagnetic simulation," *IEEE Comput. Sci. Eng.*, vol. 5, no. 4, pp. 60–67, 1998.

[12] K. Nabors and J. White, "Fastcap: A multipole accelerated 3-D capacitance extraction program," *IEEE Trans. Comput.-Aided Design Integr. Circuits Syst.*, vol. 10, no. 11, pp. 1447–1459, Nov 1991.

[13] R. Du Cloux, G. P. J. F. M. Maas, and A. J. H. Wachters, "Quasi-static boundary element method for electromagnetic simulation of PCBs," *Philips J. of Res.*, vol. 48, pp. 117–144, 1994.

[14] M. Kamon, N. A. Marques, L. M. Silveira, and J. White, "Automatic generation of accurate circuit models of 3-D interconnect," *IEEE Trans. Compon., Packag., Manuf. Technol. B*, vol. 21, no. 3, pp. 225–240, Aug 1998.

[15] W. Shi, J. Liu, N. Kakani, and T. Yu, "A fast hierarchical algorithm for three-dimensional capacitance extraction," *IEEE Trans. Comput.-Aided Design Integr. Circuits Syst.*, vol. 21, no. 3, pp. 330–336, Mar 2002.

[16] V. Jandhyala, Y. Wang, D. Gope, and C.-J. R. Shi, "A surface-based integral-equation formulation for coupled electromagnetic and circuit simulation," *Micro. and Opt. Tech. Lett.*, vol. 34, no. 2, pp. 103–106, July 2002.

[17] Z. Zhu, B. Song, and J. White, "Algorithms in FastImp: A fast and wideband impedance extraction program for complicated 3-D geometries," in *Proc. Design Automa. Conf.*, Anaheim, CA, June 2003, pp. 712–717.

[18] Y. Wang, D. Gope, V. Jandhyala, and C. J. R. Shi, "Generalized Kirchoff's current and voltage law formulation for coupled circuit-electromagnetic simulation with surface integral equations," *IEEE Trans. Microw. Theory Tech.*, vol. 52, no. 7, pp. 1673–1682, July 2004.

[19] X. Hu, J. White, J. H. Lee, and L. Daniel, "Analysis of full-wave conductor system impedance over substrate using novel integration techniques," in *Proc. Design Automa. Conf.*, San Diego, CA, June 2005, pp. 147–152.

[20] S. Chakraborty and V. Jandhyala, "Surface-based broadband electromagnetic-circuit simulation of lossy conductors," *IEE Proc. - Microw., Antennas Propag.*, vol. 153, no. 2, pp. 191–198, Apr 2006.

[21] G. Rubinacci and A. Tamburrino, "A broadband volume integral formulation based on edge-elements for full-wave analysis of lossy interconnects," *IEEE Trans. Antennas Propag.*, vol. 54, no. 10, pp. 2977–2989, Oct 2006.

[22] N. Srivastava, R. Suaya, and K. Banerjee, "High-frequency mutual impedance extraction of VLSI interconnects in the presence of a multi-layer conducting substrate," in *Design, Automation and Test in Europe (DATE) Conf.*, Munich, Germany, Mar 2008, pp. 426–431.

[23] Y. Yi, P. Li, V. Sarin, and W. Shi, "A preconditioned hierarchical algorithm for impedance extraction of three-dimensional structures with multiple dielectrics," *IEEE Trans. Comput.-Aided Design Integr. Circuits Syst.*, vol. 27, no. 11, pp. 1918–1927, Nov 2008.

[24] L. Daniel, A. Sangiovanni-Vincentelli, and J. White, "Proximity templates for modeling of skin and proximity effects on packages and high frequency interconnect," in *Proc. IEEE/ACM Int. Conf. on Comput.-Aided Des.*, San Jose, CA, 2002, pp. 326–333.

[25] S. Ortiz and R. Suaya, "Fullwave volumetric Maxwell solver using conduction modes," in *Proc. IEEE/ACM Int. Conf. on Comput.-Aided Des.*, San Jose, CA, Nov 2006, pp. 13–18.

[26] A. E. Ruehli, "Equivalent circuit models for three-dimensional multiconductor systems," *IEEE Trans. Microw. Theory Tech.*, vol. 22, no. 3, pp. 216–221, Mar 1974.

[27] P. A. Brennan, N. Raver, and A. E. Ruehli, "Three-dimensional inductance computations with partial element equivalent circuits," *IBM J. Res. Dev.*, vol. 23, no. 6, pp. 661–668, Nov 1979.

[28] A. M. Niknejad and R. G. Meyer, "Analysis of eddy-current losses over conductive substrates with applications to monolithic inductors and transformers," *IEEE Trans. Microw. Theory Tech.*, vol. 49, no. 1, pp. 166–176, Jan 2001.

[29] R. Jiang, W. Fu, and C. C.-P. Chen, "EPEEC: Comprehensive SPICE-compatible reluctance extraction for high-speed interconnects above lossy multilayer substrates," *IEEE Trans. Comput.-Aided Design Integr. Circuits Syst.*, vol. 24, no. 10, pp. 1562–1571, Oct 2005.

[30] D. Gope, A. Ruehli, and V. Jandhyala, "Solving low-frequency EM-CKT problems using the PEEC method," *IEEE Trans. Adv. Packag.*, vol. 30, no. 2, pp. 313–320, May 2007.

[31] S. V. Kochetov, M. Leone, and G. Wollenberg, "PEEC formulation based on dyadic Green's functions for layered media in the time and frequency domains," *IEEE Trans. Electromagn. Compat.*, vol. 50, no. 4, pp. 953–965, Nov 2008.

[32] H. A. Haus and J. R. Melcher, *Electromagnetic Fields and Energy.* Englewood Cliffs, NJ: Prentice-Hall, 1989.

[33] S. Ponnapalli, R. Bertin, and A. Deutsch, "A package analysis tool based on a method of moments/surface formulation," in *Proc. Electronic Compon. and Tech. Conf.*, Orlando, FL, June 1993, pp. 615–622.

[34] S. Ponnapalli, A. Deutsch, and R. Bertin, "A package analysis tool based on a method of moments surface formulation," *IEEE Trans. Compon., Hybrids, Manuf. Technol.*, vol. 16, no. 8, pp. 884–892, Dec 1993.

[35] W. C. Chew, J. Jin, E. Michielssen, and J. Song, *Fast and Efficient Algorithms in Computational Electromagnetics.* Norwood, MA: Artech House, 2001.

[36] B. Song, Z. Zhu, J. D. Rockway, and J. White, "A new surface integral formulation for wideband impedance extraction of 3-D structures," in *Int. Conf. on Computer Aided Design*, Washington, DC, Nov 2003, pp. 843–847.

[37] S. Kapur and D. E. Long, "Large-scale full-wave simulation," in *Proc. Design Automa. Conf.*, San Diego, CA, June 2004, pp. 806–809.

[38] F. Ling, V. I. Okhmatovski, W. Harris, S. McCracken, and A. Dengi, "Large-scale broad-band parasitic extraction for fast layout verification of 3-D RF and mixed-signal on-chip structures," *IEEE Trans. Microw. Theory Tech.*, vol. 53, no. 1, pp. 264–273, Jan 2005.

[39] M. I. Aksun, "A robust approach for the derivation of closed-form Green's functions," *IEEE Trans. Microw. Theory Tech.*, vol. 44, no. 5, pp. 651–658, May 1996.

[40] J. Chen, A. A. Kishk, and A. W. Glisson, "Application of a new MPIE formulation to the analysis of a dielectric resonator embedded in a multilayered medium coupled to a microstrip circuit," *IEEE Trans. Microw. Theory Tech.*, vol. 49, no. 2, pp. 263–279, Feb 2001.

[41] K. A. Michalski, "Electromagnetic field computation in planar multilayers," in *Encyclopedia of RF and Microwave Engineering*, K. Chang, Ed. John Wiley, 2005, vol. 2, pp. 1163–1190.

[42] Q. B. Rong, "Mixed potential integral equations method in 3-D induction modeling," Ph.D. dissertation, Dept. of Elec. and Compu. Engin., Univ. of Houston, 2006.

[43] K. A. Michalski and D. Zheng, "Electromagnetic scattering and radiation by surfaces of arbitrary shape in layered media. Part I: Theory," *IEEE Trans. Antennas Propag.*, vol. 38, no. 3, pp. 335–344, Mar 1990.

[44] ——, "Electromagnetic scattering and radiation by surfaces of arbitrary shape in layered media. Part II: Implementation and results for contiguous half-spaces," *IEEE Trans. Antennas Propag.*, vol. 38, no. 3, pp. 345–352, Mar 1990.

[45] R. Harrington, *Field Computation by Moment Methods*. Piscataway, NJ: IEEE Press, 1993.

[46] J. Lim, "The electromagnetic scattering from arbitrarily shaped bodies at very low frequency range using triangular patch modeling," Ph.D. dissertation, Dept.

of Elec. Engin., Auburn Univ., 1994.

[47] W. L. Wu, A. Glisson, and D. Kajfez, "A study of two numerical solution procedures for the electric field integral equation at low frequency," *Applied Computational Electromagnetics Society (ACES) Journal*, vol. 10, no. 3, pp. 69–80, Nov 1995.

[48] G. Vecchi, "Loop-star decomposition of basis functions in the discretization of the EFIE," *IEEE Trans. Antennas Propag.*, vol. 47, no. 2, pp. 339–346, Feb 1999.

[49] J.-S. Zhao and W. C. Chew, "Integral equation solution of Maxwell's equations from zero frequency to microwave frequencies," *IEEE Trans. Antennas Propag.*, vol. 48, no. 10, pp. 1635–1645, Oct 2000.

[50] S. Y. Chen, W. C. Chew, J. M. Song, and J.-S. Zhao, "Analysis of low frequency scattering from penetrable scatterers," *IEEE Trans. Geosci. Remote Sens.*, vol. 39, no. 4, pp. 726–735, Apr 2001.

[51] Y. P. Chen, J. L. Xiong, W. C. Chew, and Z. P. Nie, "Numerical analysis of electrically small structures embedded in a layered medium," *Micro. and Opt. Tech. Lett.*, vol. 51, no. 5, pp. 1304–1308, May 2009.

[52] D. R. Wilton, "Computational methods," in *Scattering and Inverse Scattering in Pure and Applied Science*, R. Pike and P. Sabatier, Eds. Academic Press, London, 2002, pp. 316–365.

[53] I. P. Theron and J. H. Cloete, "On the surface impedance used to model the conductor losses of microstrip structures," *IEE Proc. - Microw., Antennas Propag.*, vol. 142, no. 1, pp. 35–40, 1995.

[54] Y. Higuchi and M. Koizumi, "Integral equation method with surface impedance model for 3D eddy current analysis in transformers," *IEEE Trans. Magn.*, vol. 36, no. 4, pp. 774–779, July 2000.

[55] J. C. Rautio and V. Demir, "Microstrip conductor loss models for electromagnetic analysis," *IEEE Trans. Microw. Theory Tech.*, vol. 51, no. 3, pp. 915–921, Mar 2003.

[56] A. Rong, A. C. Cangellaris, and L. Dong, "A novel effective surface impedance formulation for efficient broadband modeling of lossy thick strip conductors," in *IEEE MTT-S Int. Microwave Symp. Digest*, vol. 3, Philadelphia, PA, June 2003, pp. 1959–1962.

[57] M. Al-Qedra and V. I. Okhmatovski, "Full-periphery surface impedance for skin-effect approximation in electric field integral equation," *IEEE Microw. Wireless Compon. Lett.*, vol. 19, no. 1, pp. 9–11, Jan 2009.

[58] K. A. Michalski and J. R. Mosig, "Multilayered media Green's functions in integral equation formulations," *IEEE Trans. Antennas Propag.*, vol. 45, no. 3, pp. 508–519, Mar 1997.

[59] G. Miano and F. Villone, "A surface integral formulation of Maxwell equations for topologically complex conducting domains," *IEEE Trans. Antennas Propag.*, vol. 53, no. 12, pp. 4001–4014, Dec 2005.

[60] L. O. Chua, C. A. Desoer, and E. S. Kuh, *Linear and Nonlinear Circuits.* Singapore: McGraw-Hill, 1987.

[61] S. Rao, D. Wilton, and A. Glisson, "Electromagnetic scattering by surfaces of arbitrary shape," *IEEE Trans. Antennas Propag.*, vol. 30, no. 3, pp. 409–418,

May 1982.

[62] K. A. Michalski and M. I. Aksun, "Discrete complex image method for planar multilayers with uniaxial anisotropy," in *The Second European Conf. on Antennas and Propag.*, Edinburgh, UK, Nov. 2007, pp. 1–7.

[63] J. A. Stratton, *Electromagnetic Theory*. New York: McGraw-Hill, 1941.

[64] Y.-H. Chu and W. C. Chew, "A robust surface-integral-equation formulation for conductive media," *Micro. and Opt. Tech. Lett.*, vol. 46, no. 2, pp. 109–114, July 2005.

[65] N. Kurt-Karsilayan and K. A. Michalski, "A full-wave wide-band surface-integral-equation-based field solver," in *PIERS Online*, vol. 4, no. 8, July 2008, pp. 825–830.

[66] D. M. Correia and H. Singer, "A MoM solution for the EFIE applicable to any combination of thin-wire and surface scatterers down to low frequencies," in *Int. Zurich Symp. and Tech. Exhibition on Electromagn. Compat.*, Feb 1999, pp. 363–368.

[67] M. S. Ingber and R. H. Ott, "An application of the boundary element method to the magnetic field integral equation," *IEEE Trans. Antennas Propag.*, vol. 39, no. 5, pp. 606–611, May 1991.

[68] R. E. Hodges and Y. Rahmat-Samii, "The evaluation of MFIE integrals with the use of vector triangle basis functions," *Micro. and Opt. Tech. Lett.*, vol. 14, no. 1, pp. 9–14, Jan 1997.

[69] O. Ergul and L. Gurel, "Improving the accuracy of the MFIE with the choice of basis functions," in *IEEE Antennas and Propag. Society Int. Symp.*, vol. 3,

Sendai, Japan, June 2004, pp. 3389–3392.

[70] Y. Chu, W. C. Chew, S. Chen, and J. Zhao, "Generalized PMCHWT formulation for low-frequency multi-region problems," in *IEEE Antennas and Propag. Society Int. Symp.*, vol. 3, San Antonio, TX, 2002, pp. 664–667.

[71] W. C. Chew, *Waves and Fields in Inhmogeneous Media.* New York: Van Nostrand Reinhold, 1990.

[72] W. C. Chew, J. L. Xiong, and M. A. Saville, "A matrix-friendly formulation of layered medium Green's function," *IEEE Antennas Wireless Propag. Lett.*, vol. 5, no. 1, pp. 490–494, Dec 2006.

[73] K. A. Michalski, "Extrapolation methods for Sommerfeld integral tails," *IEEE Trans. Antennas Propag.*, vol. 46, no. 10, pp. 1405–1418, Oct 1998.

APPENDIX A

BACKGROUND ON SURFACE INTEGRAL EQUATIONS

The exterior and the interior surface integral equations over a smooth surface in homogeneous medium are stated as follows [7, 52, 63–65],

$$\sum_{m=1}^{2} \alpha_m [\gamma_m \hat{n} \times \frac{\boldsymbol{M}_s}{2} + \oint [j\omega\mu_m G_m \boldsymbol{J}_s + \frac{1}{j\omega\epsilon_m} \nabla'_s \cdot \boldsymbol{J}_s \nabla' G_m + \boldsymbol{M}_s \times \nabla' G_m] ds'] = \alpha_1 \boldsymbol{E}^i, \tag{A.1}$$

$$\sum_{m=1}^{2} \beta_m [-\gamma_m \hat{n} \times \frac{\boldsymbol{J}_s}{2} + \oint [-\boldsymbol{J}_s \times \nabla' G_m + \frac{1}{j\omega\mu_m} \nabla'_s \cdot \boldsymbol{M}_s \nabla' G_m + j\omega\epsilon_m G_m \boldsymbol{M}_s] ds'] = \beta_1 \boldsymbol{H}^i, \tag{A.2}$$

where $\gamma_1 = 1, \gamma_2 = -1$, and $m = 1, 2$ represents the exterior and the interior regions, respectively. Note that, G_m is the full-wave homogeneous Green function which is introduced in (1.11).

For a perfect electric conductor (PEC), $\boldsymbol{M}_s = 0$, therefore (A.1) and (A.2) reduce to well-known EFIE [61, 66] and magnetic field integral equation (MFIE) [67–69], respectively.

$$\oint [j\omega\mu_1 G_1 \boldsymbol{J}_s + \frac{1}{j\omega\epsilon_1} \nabla'_s \cdot \boldsymbol{J}_s \nabla' G_1] ds' = \boldsymbol{E}^i \tag{A.3}$$

$$\frac{\boldsymbol{J}_s}{2} - \hat{n} \times \oint [\boldsymbol{J}_s \times \nabla' G_1] ds' = \hat{n} \times \boldsymbol{H}^i \tag{A.4}$$

When $\alpha_1 = \alpha_2$ and $\beta_1 = \beta_2$, (A.1) and (A.2) represent the Poggio-Miller-Chang-

Harrington-Wu-Tsai (PMCHWT) equations [7, 52, 70].

$$\sum_{m=1}^{2} \oint [j\omega\mu_m G_m \boldsymbol{J}_s + \frac{1}{j\omega\epsilon_m} \nabla'_s \cdot \boldsymbol{J}_s \nabla' G_m + \boldsymbol{M}_s \times \nabla' G_m] ds' = \boldsymbol{E}^i \tag{A.5}$$

$$\sum_{m=1}^{2} \oint [-\boldsymbol{J}_s \times \nabla' G_m + \frac{1}{j\omega\mu_m} \nabla'_s \cdot \boldsymbol{M}_s \nabla' G_m + j\omega\epsilon_m G_m \boldsymbol{M}_s] ds' = \boldsymbol{H}^i \tag{A.6}$$

APPENDIX B

BACKGROUND ON GREEN FUNCTIONS IN LAYERED MEDIA

Using free-space Green functions in parasitic extraction requires the discretization of both the dielectric interfaces and the substrate. Layered Green functions are used to eliminate this requirement. Layered Green functions have been derived in various references [41, 43, 44, 58, 62, 71, 72]. In this chapter, transmission line analogy is used for obtaining layered Green functions.

A. Transmission Line Analogy in Spectral Domain

The analogy between layered media and transmission line (TL) equivalent circuit is established by Michalski and Mosig [41, 58]. The TL is assumed to be along the axis normal to stratification as shown in Fig. B-1. Each layer is assumed to have uniaxial anisotropy which implies the usage of the following permittivity and permeability in dyadic form,

$$\underline{\boldsymbol{\epsilon}} = \underline{\boldsymbol{I}_t}\epsilon_t + \hat{\boldsymbol{z}}\hat{\boldsymbol{z}}\epsilon_z, \tag{B.1}$$

$$\underline{\boldsymbol{\mu}} = \underline{\boldsymbol{I}_t}\mu_t + \hat{\boldsymbol{z}}\hat{\boldsymbol{z}}\mu_z, \tag{B.2}$$

in (1.1) and (1.2). Since the medium is homogeneous and of infinite extent in transverse plane, Fourier transform of all the fields in transverse coordinates can be represented as follows,

$$\tilde{f}(\boldsymbol{k}_\rho, z) = \int_{-\infty}^{\infty}\int_{-\infty}^{\infty} f(\boldsymbol{r})e^{j\boldsymbol{k}_\rho\cdot\boldsymbol{\rho}}dxdy \tag{B.3}$$

Inverse Fourier transform of each field can be represented as follows,

$$f(\boldsymbol{r}) = \frac{1}{(2\pi)^2}\int_{-\infty}^{\infty}\int_{-\infty}^{\infty} \tilde{f}(\boldsymbol{k}_\rho, z)e^{-j\boldsymbol{k}_\rho\cdot\boldsymbol{\rho}}dk_x dk_y \tag{B.4}$$

where

$$\boldsymbol{\rho} = \hat{\boldsymbol{x}}x + \hat{\boldsymbol{y}}y, \tag{B.5}$$

$$\boldsymbol{k}_\rho = \hat{\boldsymbol{x}}k_x + \hat{\boldsymbol{y}}k_y \tag{B.6}$$

Note that, (B.4) can also be represented with Sommerfeld integrals where the integration variable is k_ρ instead of k_x and k_y. General form of Sommerfeld integrals is shown as follows,

$$f(\boldsymbol{r}) = S_n\{\tilde{f}(\boldsymbol{k}_\rho, z)\} = \frac{1}{2\pi}\int_0^\infty \tilde{f}(\boldsymbol{k}_\rho, z)J_n(k_\rho\rho)k_\rho dk_\rho \tag{B.7}$$

or in terms of normalized coordinates,

$$f(\boldsymbol{r}) = S_n^m\{\tilde{f}(\boldsymbol{k}_\rho, z)\} = \frac{1}{2\pi}\int_0^\infty \tilde{f}(\boldsymbol{k}_\rho, z)J_n(k_\rho\rho)\left(\frac{k_\rho}{k_0}\right)^m d\left(\frac{k_\rho}{k_0}\right) \tag{B.8}$$

Taking the Fourier transform of Maxwell equations (1.1), (1.2) by using (B.3), and separating transverse and longitudinal components, we obtain the following equations,

$$\frac{d}{dz}\tilde{\boldsymbol{E}}_t = \frac{1}{j\omega\epsilon_0\epsilon_t}(k^2 - \frac{1}{\nu^e}\boldsymbol{k}_\rho\boldsymbol{k}_\rho\cdot)(\tilde{\boldsymbol{H}}_t \times \hat{\boldsymbol{z}}) + \boldsymbol{k}_\rho\frac{\tilde{\boldsymbol{J}}_z}{\omega\epsilon_0\epsilon_z} - \tilde{\boldsymbol{M}}_t \times \hat{\boldsymbol{z}} \tag{B.9}$$

$$\frac{d}{dz}\tilde{\boldsymbol{H}}_t = \frac{1}{j\omega\mu_0\mu_t}(k^2 - \frac{1}{\nu^h}\boldsymbol{k}_{\boldsymbol{\rho}}\boldsymbol{k}_{\boldsymbol{\rho}}\cdot)(\tilde{\boldsymbol{E}}_t \times \hat{\boldsymbol{z}}) + \boldsymbol{k}_\rho\frac{\tilde{\boldsymbol{M}}_z}{\omega\mu_0\mu_z} - \hat{\boldsymbol{z}} \times \tilde{\boldsymbol{J}}_t \tag{B.10}$$

$$-j\omega\epsilon_0\epsilon_z\tilde{\boldsymbol{E}}_z = j\boldsymbol{k}_\rho \cdot (\tilde{\boldsymbol{H}}_t \times \hat{\boldsymbol{z}}) + \tilde{\boldsymbol{J}}_z \tag{B.11}$$

$$-j\omega\mu_0\mu_z\tilde{\boldsymbol{H}}_z = j\boldsymbol{k}_\rho \cdot (\hat{\boldsymbol{z}} \times \tilde{\boldsymbol{E}}_t) + \tilde{\boldsymbol{M}}_z \tag{B.12}$$

where

$$k = k_0\sqrt{\epsilon_t\mu_t}, \tag{B.13}$$

$$k_0 = \omega\sqrt{\epsilon_0\mu_0}, \tag{B.14}$$

$$\nu^e = \frac{\epsilon_z}{\epsilon_t}, \tag{B.15}$$

$$\nu^h = \frac{\mu_z}{\mu_t} \tag{B.16}$$

After defining spectral-domain coordinate system $(\hat{\boldsymbol{u}}, \hat{\boldsymbol{v}})$ such that

$$\hat{\boldsymbol{u}} = \frac{\boldsymbol{k}_\rho}{k_\rho} = \hat{\boldsymbol{x}}\cos\xi + \hat{\boldsymbol{y}}\sin\xi, \tag{B.17}$$

$$\hat{\boldsymbol{v}} = \frac{\hat{\boldsymbol{z}} \times \boldsymbol{k}_\rho}{k_\rho} = -\hat{\boldsymbol{x}}\sin\xi + \hat{\boldsymbol{y}}\cos\xi \tag{B.18}$$

where $k_\rho = \sqrt{k_x^2 + k_y^2}$ and ξ represents the angle between $\boldsymbol{k}_\rho$ and $\boldsymbol{k}_x$, transverse electric and magnetic fields can be represented with TL voltage and current variables as follows,

$$\tilde{\boldsymbol{E}}_t = \hat{\boldsymbol{u}}V^e + \hat{\boldsymbol{v}}V^h, \tag{B.19}$$

$$\tilde{\boldsymbol{H}}_t = -\hat{\boldsymbol{u}}I^h + \hat{\boldsymbol{v}}I^e \tag{B.20}$$

Using (B.19) and (B.20) in (B.9) and (B.10) and projecting on $\hat{\boldsymbol{u}}$ and $\hat{\boldsymbol{v}}$, following TL equations are obtained,

$$\frac{dV^\alpha}{dz} = -jk_z^\alpha Z^\alpha I^\alpha + v^\alpha, \tag{B.21}$$

$$\frac{dI^\alpha}{dz} = -jk_z^\alpha Y^\alpha V^\alpha + i^\alpha, \tag{B.22}$$

where

$$k_z^\alpha = \sqrt{k^2 - \frac{k_\rho^2}{\nu^\alpha}}, \tag{B.23}$$

$$Z^e = \frac{1}{Y^e} = \frac{k_z^e}{\omega\epsilon_0\epsilon_t}, \tag{B.24}$$

$$Z^h = \frac{1}{Y^h} = \frac{\omega\mu_0\mu_t}{k_z^h}, \tag{B.25}$$

α is e or h, representing TM or TE waves, respectively. The sources for each mode are shown below.

$$v^e = \frac{k_\rho}{\omega\epsilon_0\epsilon_z}\tilde{\boldsymbol{J}}_z - \tilde{\boldsymbol{M}}_v, \tag{B.26}$$

$$v^h = \tilde{\boldsymbol{M}}_u, \tag{B.27}$$

$$i^e = -\tilde{\boldsymbol{J}}_u, \tag{B.28}$$

$$i^h = \frac{k_\rho}{\omega\mu_0\mu_z}\tilde{\boldsymbol{M}}_z - \tilde{\boldsymbol{J}}_v \tag{B.29}$$

Transmission line Green functions (TLGF) are defined as the voltages and currents when the TL is excited by unit-strength impulsive voltage and current sources as shown in Fig. B-2. V_i and I_i represent TLGF when the excitation is through a current source, whereas V_v and I_v represent TLGF when the excitation is through a voltage source. Using the superposition property due to the linearity of TL equations, V and I at any point in the transmission line can be expressed as follows,

$$V(z) = \langle V_i(z|z'), i(z')\rangle + \langle V_v(z|z'), v(z')\rangle \tag{B.30}$$

$$I(z) = \langle I_i(z|z'), i(z')\rangle + \langle I_v(z|z'), v(z')\rangle \tag{B.31}$$

TL voltage and current waves possess the reciprocity properties [41],

$$V_i(z|z') = V_i(z'|z), \tag{B.32}$$

$$I_v(z|z') = I_v(z'|z), \tag{B.33}$$

$$V_v(z|z') = -I_i(z'|z) \tag{B.34}$$

When the source and the observation point lie within the same TL section (i.e. m=n), the voltage and the current equations are found as follows,

$$V_i(z|z') = \frac{Z_n}{2}\left[e^{-jk_{z,n}|z-z'|} + \frac{1}{D_n}\sum_{s=1}^{4} R_n^s e^{-jk_{z,n}\zeta_n^s}\right], \tag{B.35}$$

$$I_i(z|z') = \frac{1}{2}\left[e^{\pm jk_{z,n}|z-z'|} - \frac{1}{D_n}\sum_{s=1}^{4}(-1)^s R_n^s e^{-jk_{z,n}\zeta_n^s}\right], \tag{B.36}$$

where $\pm$ corresponds to $z \gtrless z'$,

$$R_n^1 = \overleftarrow{\Gamma}_n, \tag{B.37}$$

$$R_n^2 = \overrightarrow{\Gamma}_n, \tag{B.38}$$

$$R_n^3 = R_n^4 = \overleftarrow{\Gamma}_n \overrightarrow{\Gamma}_n, \tag{B.39}$$

$$\zeta_n^1 = z + z' - 2z_n, \tag{B.40}$$

$$\zeta_n^2 = 2z_{n+1} - (z + z'), \tag{B.41}$$

$$\zeta_n^3 = 2d_n + (z - z'), \tag{B.42}$$

$$\zeta_n^4 = 2d_n - (z - z'), \tag{B.43}$$

and the resonant denominator is

$$D_n = 1 - \overleftarrow{\Gamma}_n \overrightarrow{\Gamma}_n e^{-j2k_{z,n}d_n}, \tag{B.44}$$

where $\overleftarrow{\Gamma}_n$ and $\overrightarrow{\Gamma}_n$ represent the backward and forward reflection coefficients as shown in Fig. B-2,

$$\overleftarrow{\Gamma}_n = \frac{\overleftarrow{Z}_{n-1} - Z_n}{\overleftarrow{Z}_{n-1} + Z_n}, \tag{B.45}$$

$$\overrightarrow{\Gamma}_n = \frac{\overrightarrow{Z}_{n+1} - Z_n}{\overrightarrow{Z}_{n+1} + Z_n} \tag{B.46}$$

Recursive formulas for the reflection coefficients are found as [41],

$$\overleftarrow{\Gamma}_n = \frac{\Gamma_{n-1,n} + \overleftarrow{\Gamma}_{n-1} e^{-j2k_{z,n-1}d_{n-1}}}{1 + \Gamma_{n-1,n}\overleftarrow{\Gamma}_{n-1} e^{-j2k_{z,n-1}d_{n-1}}}, \tag{B.47}$$

$$\overrightarrow{\Gamma}_n = \frac{\Gamma_{n+1,n} + \overrightarrow{\Gamma}_{n+1} e^{-j2k_{z,n+1}d_{n+1}}}{1 + \Gamma_{n+1,n}\overrightarrow{\Gamma}_{n+1} e^{-j2k_{z,n+1}d_{n+1}}} \tag{B.48}$$

where

$$\Gamma_{i,j} = \frac{Z_i - Z_j}{Z_i + Z_j} \tag{B.49}$$

When the source and the observation point lie in different sections ($m > n$), the voltages and the currents at point z in section m are found as follows,

$$V_i(z|z') = V_i(z_{n+1}|z')\overrightarrow{T}^1_{nm} e^{-jk_{z,m}(z-z_m)} \left[\frac{1 + \overrightarrow{\Gamma}_m e^{-j2k_{z,m}(z_{m+1}-z)}}{1 + \overrightarrow{\Gamma}_m e^{-j2k_{z,m}d_m}}\right], \tag{B.50}$$

$$I_i(z|z') = I_i(z_{n+1}|z')\overrightarrow{T}^2_{nm}e^{-jk_{z,m}(z-z_m)}\left[\frac{1-\overrightarrow{\Gamma}_m e^{-j2k_{z,m}(z_{m+1}-z)}}{1-\overrightarrow{\Gamma}_m e^{-j2k_{z,m}d_m}}\right], \tag{B.51}$$

where the voltage transmission coefficient between the right terminals of section n and the left terminals of section m is defined as

$$\overrightarrow{T}^{1,2}_{nm} = \prod_{k=n+1}^{m-1}\overrightarrow{\tau}^{1,2}_k, \tag{B.52}$$

where

$$\overrightarrow{\tau}^1_k = \frac{(1+\overrightarrow{\Gamma}_k e^{-jk_{z,k}d_k})}{1+\overrightarrow{\Gamma}_k e^{-j2k_{z,k}d_k}}, \tag{B.53}$$

$$\overrightarrow{\tau}^2_k = \frac{(1-\overrightarrow{\Gamma}_k e^{-jk_{z,k}d_k})}{1-\overrightarrow{\Gamma}_k e^{-j2k_{z,k}d_k}} \tag{B.54}$$

Rest of the TLGF, I_v and V_v are dual to V_i and I_i, therefore the former can be obtained by replacing the impedances by the admittances and the reflection coefficients by their negatives in (B.50) and (B.51). When $m < n$, the reciprocity equations in (B.32), (B.33), (B.34) can be used to obtain all the TLGF based on the equations for $m \geqslant n$.

B. Formulation of Green Functions

Now that the TLGF equations are derived, using (B.9), (B.10), (B.11), (B.12), (B.30) and (B.31) lead to the spectral domain representation of the electric and magnetic fields in terms of the spectral domain dyadic Green functions as follows,

$$\tilde{\boldsymbol{E}} = \langle\underline{\tilde{\boldsymbol{G}}}^{\boldsymbol{EJ}}, \tilde{\boldsymbol{J}}\rangle + \langle\underline{\tilde{\boldsymbol{G}}}^{\boldsymbol{EM}}, \tilde{\boldsymbol{M}}\rangle \tag{B.55}$$

$$\tilde{\boldsymbol{H}} = \langle\underline{\tilde{\boldsymbol{G}}}^{\boldsymbol{HJ}}, \tilde{\boldsymbol{J}}\rangle + \langle\underline{\tilde{\boldsymbol{G}}}^{\boldsymbol{HM}}, \tilde{\boldsymbol{M}}\rangle \tag{B.56}$$

where

$$\underline{\tilde{\boldsymbol{G}}}^{\boldsymbol{EJ}} = -\hat{\boldsymbol{u}}\hat{\boldsymbol{u}}V_i^e - \hat{\boldsymbol{v}}\hat{\boldsymbol{v}}V_i^h + \hat{\boldsymbol{z}}\hat{\boldsymbol{u}}\frac{k_\rho}{\omega\epsilon_0\epsilon_z}I_i^e + \hat{\boldsymbol{u}}\hat{\boldsymbol{z}}\frac{k_\rho}{\omega\epsilon_0\epsilon'_z}V_v^e + \hat{\boldsymbol{z}}\hat{\boldsymbol{z}}\frac{1}{j\omega\epsilon_0\epsilon'_z}[\frac{k_\rho^2}{j\omega\epsilon_0\epsilon_z}I_v^e - \delta(z-z')] \tag{B.57}$$

$$\underline{\tilde{\boldsymbol{G}}}^{\boldsymbol{EM}} = -\hat{\boldsymbol{u}}\hat{\boldsymbol{v}}V_v^e + \hat{\boldsymbol{v}}\hat{\boldsymbol{u}}V_v^h + \hat{\boldsymbol{z}}\hat{\boldsymbol{v}}\frac{k_\rho}{\omega\epsilon_0\epsilon_z}I_v^e - \hat{\boldsymbol{v}}\hat{\boldsymbol{z}}\frac{k_\rho}{\omega\mu_0\mu_z'}V_i^h \tag{B.58}$$

$$\underline{\tilde{\boldsymbol{G}}}^{\boldsymbol{HJ}} = \hat{\boldsymbol{u}}\hat{\boldsymbol{v}}I_i^h - \hat{\boldsymbol{v}}\hat{\boldsymbol{u}}I_i^e - \hat{\boldsymbol{z}}\hat{\boldsymbol{v}}\frac{k_\rho}{\omega\mu_0\mu_z}V_i^h + \hat{\boldsymbol{v}}\hat{\boldsymbol{z}}\frac{k_\rho}{\omega\epsilon_0\epsilon_z'}I_v^e \tag{B.59}$$

$$\underline{\tilde{\boldsymbol{G}}}^{\boldsymbol{HM}} = -\hat{\boldsymbol{u}}\hat{\boldsymbol{u}}I_v^h - \hat{\boldsymbol{v}}\hat{\boldsymbol{v}}I_v^e + \hat{\boldsymbol{z}}\hat{\boldsymbol{u}}\frac{k_\rho}{\omega\mu_0\mu_z}V_v^h + \hat{\boldsymbol{u}}\hat{\boldsymbol{z}}\frac{k_\rho}{\omega\mu_0\mu_z'}I_i^h + \hat{\boldsymbol{z}}\hat{\boldsymbol{z}}\frac{1}{j\omega\mu_0\mu_z'}\left[\frac{k_\rho^2}{j\omega\mu_0\mu_z}V_i^h - \delta(z-z')\right] \tag{B.60}$$

Since the dyadic kernels in (B.55) and (B.56) are highly singular, mixed potential form of the field equations are used as follows,

$$\tilde{\boldsymbol{E}} = -j\omega\underline{\tilde{\boldsymbol{A}}} - \boldsymbol{\nabla}\tilde{\Phi} + \epsilon^{-1}\cdot\boldsymbol{\nabla}\times\underline{\tilde{\boldsymbol{F}}} \tag{B.61}$$

$$\tilde{\boldsymbol{H}} = -j\omega\underline{\tilde{\boldsymbol{F}}} - \boldsymbol{\nabla}\tilde{\Psi} + \mu^{-1}\cdot\boldsymbol{\nabla}\times\underline{\tilde{\boldsymbol{A}}} \tag{B.62}$$

where

$$\underline{\tilde{\boldsymbol{A}}} = \mu_0\langle\underline{\tilde{\boldsymbol{G}}}^{\boldsymbol{A}}, \tilde{\boldsymbol{J}}\rangle \tag{B.63}$$

In order to derive $\underline{\tilde{\boldsymbol{G}}}^{\boldsymbol{A}}$, the magnetic currents are set to zero in (B.61) and (B.62). Equating (B.56) and (B.62), we get,

$$\underline{\boldsymbol{\mu}}\cdot\underline{\tilde{\boldsymbol{G}}}^{\boldsymbol{HJ}} = \boldsymbol{\nabla}\times\underline{\tilde{\boldsymbol{G}}}^{\boldsymbol{A}} \tag{B.64}$$

where

$$\tilde{\boldsymbol{\nabla}} = -jk_\rho\hat{\boldsymbol{u}} + \hat{\boldsymbol{z}}\frac{d}{dz} \tag{B.65}$$

Note that, $\underline{\tilde{\boldsymbol{G}}}^{\boldsymbol{A}}$ is not unique. Next two sections contain derivations of two sets of layered kernels for two MPIE forms.

1. Mixed Potential Form I

One form of the vector potential dyadic is as shown below where the correction factor due to vertical currents in the scalar potential kernel is incorporated in the vector

potential kernel.

$$\underline{\tilde{\boldsymbol{G}}}^{\boldsymbol{A}} = \underline{\boldsymbol{I}}_t \tilde{G}^A_{uu} + \hat{\boldsymbol{z}}\hat{\boldsymbol{u}}\tilde{G}^A_{zu} + \hat{\boldsymbol{u}}\hat{\boldsymbol{z}}\tilde{G}^A_{uz} + \hat{\boldsymbol{z}}\hat{\boldsymbol{z}}\tilde{G}^A_{zz} \tag{B.66}$$

After solving (B.64), each dyadic term is obtained as follows,

$$\tilde{G}^A_{uu} = \frac{V_i^h}{j\omega\mu_0} \tag{B.67}$$

$$\tilde{G}^A_{zz} = \frac{1}{j\omega\mu_0}\left(\frac{\mu_t}{\epsilon_z'} + \frac{\mu_t'}{\epsilon_z}\right)\frac{\eta_0}{k_0^2} I_v^e + \mu_t\mu_t' \frac{\eta_0(I_v^h - I_v^e)}{k_\rho^2} \tag{B.68}$$

$$\tilde{G}^A_{zu} = \frac{-j\mu_t}{k_\rho}(I_i^h - I_i^e) \tag{B.69}$$

$$\tilde{G}^A_{uz} = \mu_t' \frac{V_v^h - V_v^e}{k_\rho} \tag{B.70}$$

The scalar potential kernels are found based on the auxiliary condition (B.71).

$$-j\omega\mu_0\epsilon_0\epsilon_t\tilde{\Phi} = \tilde{\boldsymbol{\nabla}} \cdot (\mu_t^{-1}\mu_z^{-1}\underline{\boldsymbol{\mu}} \cdot \tilde{\boldsymbol{A}}) \tag{B.71}$$

To arrive at the mixed potential form of $\tilde{\boldsymbol{E}}$, following equation is postulated,

$$-\tilde{\boldsymbol{\nabla}}'\tilde{G}^{\phi} = \epsilon_t^{-1}\tilde{\boldsymbol{\nabla}} \cdot (\mu_t^{-1}\mu_z^{-1}\underline{\boldsymbol{\mu}} \cdot \tilde{\boldsymbol{G}}^{\boldsymbol{A}}) \tag{B.72}$$

where $\tilde{G}^{\phi}$ represent the scalar potential kernel. Using (B.66) and (B.73),

$$\tilde{\boldsymbol{\nabla}}' = jk_\rho\hat{\boldsymbol{u}} + \hat{\boldsymbol{z}}\frac{d}{dz'}, \tag{B.73}$$

$\tilde{G}^{\phi}$ is obtained as follows,

$$\tilde{G}^{\phi} = -j\omega\epsilon_0 \frac{V_i^h - V_i^e}{k_\rho^2} \tag{B.74}$$

Substituting (B.71) and (B.72) in (B.61), the desired mixed potential form is obtained,

$$\tilde{\boldsymbol{E}} = -j\omega\mu_0\langle\underline{\tilde{\boldsymbol{G}}}^{\boldsymbol{A}}, \tilde{\boldsymbol{J}}\rangle + \frac{1}{j\omega\epsilon_0}\nabla\langle\tilde{G}^{\phi}, \tilde{\boldsymbol{\nabla}} \cdot \tilde{\boldsymbol{J}}\rangle \tag{B.75}$$

In the presence of only magnetic currents, the analysis is dual to the absence of magnetic currents. The MPIE form of $\tilde{\boldsymbol{H}}$ can be obtained by replacing the parameters

as, $\tilde{\boldsymbol{E}} \rightarrow \tilde{\boldsymbol{H}}, \tilde{\boldsymbol{J}} \rightarrow \tilde{\boldsymbol{M}}, \tilde{\boldsymbol{A}} \rightarrow \tilde{\boldsymbol{F}}, \tilde{\Phi} \rightarrow \tilde{\Psi}, \epsilon \rightarrow \mu, \mu \rightarrow \epsilon, V \rightarrow I, I \rightarrow V, v \rightarrow i, i \rightarrow v, e \rightarrow h, h \rightarrow e$

$$\tilde{\boldsymbol{H}} = -j\omega\epsilon_0 \langle \underline{\tilde{\boldsymbol{G}}}^{\boldsymbol{F}}, \tilde{\boldsymbol{M}} \rangle + \frac{1}{j\omega\mu_0} \nabla \langle \tilde{G}^{\psi}, \boldsymbol{\nabla} \cdot \tilde{\boldsymbol{M}} \rangle \tag{B.76}$$

When both electric and magnetic currents are present, MPIE equations are similar to free-space forms as shown below,

$$\tilde{\boldsymbol{E}} = -j\omega\mu_0 \langle \underline{\tilde{\boldsymbol{G}}}^{\boldsymbol{A}}, \tilde{\boldsymbol{J}} \rangle + \frac{1}{j\omega\epsilon_0} \nabla \langle \tilde{G}^{\phi}, \boldsymbol{\nabla} \cdot \tilde{\boldsymbol{J}} \rangle + \langle \underline{\tilde{\boldsymbol{G}}}^{\boldsymbol{HM}}, \tilde{\boldsymbol{M}} \rangle \tag{B.77}$$

$$\tilde{\boldsymbol{H}} = -j\omega\epsilon_0 \langle \underline{\tilde{\boldsymbol{G}}}^{\boldsymbol{F}}, \tilde{\boldsymbol{M}} \rangle + \frac{1}{j\omega\mu_0} \nabla \langle \tilde{G}^{\psi}, \boldsymbol{\nabla} \cdot \tilde{\boldsymbol{M}} \rangle + \langle \underline{\tilde{\boldsymbol{G}}}^{\boldsymbol{HJ}}, \tilde{\boldsymbol{J}} \rangle \tag{B.78}$$

Projection of (B.66) on the cartesian coordinates results as follows,

$$\underline{\tilde{\boldsymbol{G}}}^{\boldsymbol{A}} = \underline{\boldsymbol{I}_t} \tilde{G}^A_{uu} + \hat{\boldsymbol{z}}\hat{\boldsymbol{x}} \frac{k_x}{k_\rho} \tilde{G}^A_{zu} + \hat{\boldsymbol{z}}\hat{\boldsymbol{y}} \frac{k_y}{k_\rho} \tilde{G}^A_{zu} + \hat{\boldsymbol{z}}\hat{\boldsymbol{z}} \tilde{G}^A_{zz} \tag{B.79}$$

Spatial domain Green functions are listed as follows,

$$G^{\phi}(\rho; z|z') = -j\omega\epsilon_0 S_0 \left\{ \frac{V_i^h - V_i^e}{k_\rho^2} \right\} \tag{B.80}$$

$$G^A_{xx}(\rho; z|z') = \frac{1}{j\omega\mu_0} S_0 \{V_i^h\} \tag{B.81}$$

$$G^A_{zz}(\rho; z|z') = -j\omega\mu_0 S_0 \left\{ \left(\frac{\mu_t}{\epsilon'_z} + \frac{\mu'_t}{\epsilon_z} \right) \frac{I_v^e}{k_0^2} + \mu_t \mu'_t \frac{I_v^h - I_v^e}{k_\rho^2} \right\} \tag{B.82}$$

$$\left. \begin{matrix} G^A_{zx}(\rho; z|z') \\ G^A_{zy}(\rho; z|z') \end{matrix} \right\} = \left. \begin{matrix} -\cos(\phi) \\ -\sin(\phi) \end{matrix} \right\} S_1 \left\{ \mu_t \frac{(I_i^h - I_i^e)}{k_\rho} \right\} \tag{B.83}$$

$$\left. \begin{matrix} G^A_{xz}(\rho; z|z') \\ G^A_{yz}(\rho; z|z') \end{matrix} \right\} = \left. \begin{matrix} -\cos\phi \\ -\sin\phi \end{matrix} \right\} S_1 \left\{ \mu'_t \frac{(V_v^h - V_v^e)}{k_\rho} \right\} \tag{B.84}$$

2. Mixed Potential Form II

Another form of the $\underline{\tilde{\boldsymbol{G}}}^{\boldsymbol{A}}$ is shown below which will lead to MPIE form in (B.94) and (B.95) [58].

$$\underline{\tilde{\boldsymbol{G}}}^{\boldsymbol{A}} = \underline{\boldsymbol{I}}_t \tilde{G}^A_{uu} + \hat{\boldsymbol{z}}\hat{\boldsymbol{u}}\tilde{G}^A_{zu} + \hat{\boldsymbol{z}}\hat{\boldsymbol{z}}\tilde{G}^A_{zz} \tag{B.85}$$

After solving (B.64), each dyadic term is as follows,

$$\tilde{G}^A_{uu} = \frac{V^h_i}{j\omega\mu_0} \tag{B.86}$$

$$\tilde{G}^A_{zz} = \frac{\mu_t}{j\omega\epsilon_0\epsilon'_z} I^e_v \tag{B.87}$$

$$\tilde{G}^A_{zu} = -j\frac{\mu_t}{k_\rho}(I^h_i - I^e_i) \tag{B.88}$$

The scalar potential kernels are found based on the auxiliary condition (B.71). To arrive at the mixed potential form of $\tilde{\boldsymbol{E}}$, following equation is postulated,

$$-\tilde{\boldsymbol{\nabla}}'\tilde{G}^\phi + \tilde{C}^\phi\hat{\boldsymbol{z}} = \epsilon_t^{-1}\tilde{\boldsymbol{\nabla}} \cdot (\mu_t^{-1}\mu_z^{-1}\underline{\boldsymbol{\mu}} \cdot \tilde{\boldsymbol{G}}^{\boldsymbol{A}}) \tag{B.89}$$

where $\tilde{G}^\phi$ and $\tilde{C}^\phi$ represent the scalar potential kernel and the correction factor, respectively. The correction factor is due to the presence of both horizontal and vertical current components. Using (B.85) and (B.73), the following equations are obtained,

$$\tilde{G}^\phi = \frac{-j\omega\epsilon_0}{k_\rho^2}(V^h_i - V^e_i) \tag{B.90}$$

$$\tilde{C}^\phi = \frac{k_0^2\mu'_t}{k_\rho^2}(V^h_v - V^e_v) \tag{B.91}$$

Substituting (B.71) and (B.89) in (B.61), the desired mixed potential form is obtained,

$$\tilde{\boldsymbol{E}} = -j\omega\mu_0\langle\underline{\tilde{\boldsymbol{G}}}^{\boldsymbol{A}}, \tilde{\boldsymbol{J}}\rangle + \frac{1}{j\omega\epsilon_0}\nabla(\langle\tilde{G}^\phi, \boldsymbol{\nabla}\cdot\tilde{\boldsymbol{J}}\rangle + \langle\tilde{C}^\phi\hat{\boldsymbol{z}}, \tilde{\boldsymbol{J}}\rangle) \tag{B.92}$$

In the presence of only magnetic currents, the analysis is dual to the absence of magnetic currents. The MPIE form of $\tilde{\boldsymbol{H}}$ can be obtained by replacing the parameters

as, $\tilde{\boldsymbol{E}} \rightarrow \tilde{\boldsymbol{H}}, \tilde{\boldsymbol{J}} \rightarrow \tilde{\boldsymbol{M}}, \tilde{\boldsymbol{A}} \rightarrow \tilde{\boldsymbol{F}}, \tilde{\Phi} \rightarrow \tilde{\Psi}, \epsilon \rightarrow \mu, \mu \rightarrow \epsilon, V \rightarrow I, I \rightarrow V, v \rightarrow i, i \rightarrow v, e \rightarrow h, h \rightarrow e$

$$\tilde{\boldsymbol{H}} = -j\omega\epsilon_0 \langle \underline{\tilde{\boldsymbol{G}}}^{\boldsymbol{F}}, \tilde{\boldsymbol{M}} \rangle + \frac{1}{j\omega\mu_0} \nabla (\langle \tilde{G}^{\psi}, \boldsymbol{\nabla} \cdot \tilde{\boldsymbol{M}} \rangle + \langle \tilde{C}^{\psi} \hat{\boldsymbol{z}}, \tilde{\boldsymbol{M}} \rangle) \tag{B.93}$$

When both electric and magnetic currents are present, MPIE equations are stated as,

$$\tilde{\boldsymbol{E}} = -j\omega\mu_0 \langle \underline{\tilde{\boldsymbol{G}}}^{\boldsymbol{A}}, \tilde{\boldsymbol{J}} \rangle + \frac{1}{j\omega\epsilon_0} \nabla (\langle \tilde{G}^{\phi}, \boldsymbol{\nabla} \cdot \tilde{\boldsymbol{J}} \rangle + \langle \tilde{C}^{\phi} \hat{\boldsymbol{z}}, \tilde{\boldsymbol{J}} \rangle) + \langle \underline{\tilde{\boldsymbol{G}}}^{\boldsymbol{HM}}, \tilde{\boldsymbol{M}} \rangle \tag{B.94}$$

$$\tilde{\boldsymbol{H}} = -j\omega\epsilon_0 \langle \underline{\tilde{\boldsymbol{G}}}^{\boldsymbol{F}}, \tilde{\boldsymbol{M}} \rangle + \frac{1}{j\omega\mu_0} \nabla (\langle \tilde{G}^{\psi}, \boldsymbol{\nabla} \cdot \tilde{\boldsymbol{M}} \rangle + \langle \tilde{C}^{\psi} \hat{\boldsymbol{z}}, \tilde{\boldsymbol{M}} \rangle) + \langle \underline{\tilde{\boldsymbol{G}}}^{\boldsymbol{HJ}}, \tilde{\boldsymbol{J}} \rangle \tag{B.95}$$

Projection of (B.85) on the cartesian coordinates results as follows,

$$\begin{aligned} \underline{\tilde{\boldsymbol{G}}}^{\boldsymbol{A}} = \underline{\boldsymbol{I}}_t \tilde{G}^A_{uu} + \hat{\boldsymbol{z}}\hat{\boldsymbol{x}} \frac{k_x}{k_\rho} \tilde{G}^A_{zu} + \hat{\boldsymbol{z}}\hat{\boldsymbol{y}} \frac{k_y}{k_\rho} \tilde{G}^A_{zu} \\ + \hat{\boldsymbol{x}}\hat{\boldsymbol{z}} \frac{k_x}{k_\rho} \tilde{G}^A_{uz} + \hat{\boldsymbol{y}}\hat{\boldsymbol{z}} \frac{k_y}{k_\rho} \tilde{G}^A_{uz} + \hat{\boldsymbol{z}}\hat{\boldsymbol{z}} \tilde{G}^A_{zz} \end{aligned} \tag{B.96}$$

Now that, the MPIE form of the equations due to layered kernels are defined in spectral domain, they need to be transformed to spatial domain by using (B.4), (B.7), or (B.8). Spatial domain Green functions are listed as follows,

$$C^{\phi}(\rho, z|z') = k_0^2 S_0 \left\{ \frac{\mu'_t}{k_\rho^2} (V_v^h - V_v^e) \right\} \tag{B.97}$$

$$G^{\phi}(\rho, z|z') = -j\omega\epsilon_0 S_0 \left\{ \frac{V_i^h - V_i^e}{k_\rho^2} \right\} \tag{B.98}$$

$$G^A_{xx}(\rho, z|z') = \frac{1}{j\omega\mu_0} S_0 \{V_i^h\} \tag{B.99}$$

$$G^A_{zz}(\rho, z|z') = \frac{1}{j\omega\epsilon_0} S_0 \left\{ \frac{\mu_t}{\epsilon'_z} I_v^e \right\} \tag{B.100}$$

$$G^A_{zx}(\rho, z|z') = -\cos\phi S_1 \left\{ \mu_t \frac{(I_i^h - I_i^e)}{k_\rho} \right\} \tag{B.101}$$

$$G^A_{zy}(\rho, z|z') = -\sin\phi S_1 \left\{ \mu_t \frac{(I_i^h - I_i^e)}{k_\rho} \right\} \tag{B.102}$$

Table IX. Summary of kernel properties

MPIE form(s)	Kernel	Expression
I,II	$G^A_{xx}(\rho, z\|z')$	$\frac{1}{j\omega\mu_0} S_0\{V_i^h\}$
I	$G^A_{zz}(\rho; z\|z')$	$-j\omega\mu_0 S_0 \left\{ \left(\frac{\mu_t}{\epsilon'_z} + \frac{\mu'_t}{\epsilon_z} \right) \frac{I_v^e}{k_0^2} + \mu_t \mu'_t \frac{I_v^h - I_v^e}{k_\rho^2} \right\}$
I	$G^A_{xz}(\rho; z\|z')$	$-\cos\phi S_1 \left\{ \mu'_t \frac{(V_v^h - V_v^e)}{k_\rho} \right\}$
I	$G^A_{yz}(\rho; z\|z')$	$-\sin\phi S_1 \left\{ \mu'_t \frac{(V_v^h - V_v^e)}{k_\rho} \right\}$
I,II	$G^\phi(\rho, z\|z')$	$-j\omega\epsilon_0 S_0 \left\{ \frac{V_i^h - V_i^e}{k_\rho^2} \right\}$
I,II	$G^A_{zx}(\rho, z\|z')$	$-\cos\phi S_1 \left\{ \mu_t \frac{(I_i^h - I_i^e)}{k_\rho} \right\}$
I,II	$G^A_{zy}(\rho, z\|z')$	$-\sin\phi S_1 \left\{ \mu_t \frac{(I_i^h - I_i^e)}{k_\rho} \right\}$
II	$G^A_{zz}(\rho, z\|z')$	$\frac{1}{j\omega\epsilon_0} S_0 \left\{ \frac{\mu_t}{\epsilon'_z} I_v^e \right\}$
II	$C^\phi(\rho, z\|z')$	$k_0^2 S_0 \left\{ \frac{\mu'_t}{k_\rho^2} (V_v^h - V_v^e) \right\}$

where ϕ represents the angle between x-coordinate and $\boldsymbol{\rho}$.

The kernel properties for each MPIE form are summarized in Table IX. Note that, the MPIE form II requires one less kernel to be computed compared to the MPIE form I, although the number of distinct Sommerfeld integrals to be computed in both cases is five. The common kernels in two forms are G^ϕ, G^A_{xx}, G^A_{zx}, G^A_{zy} whereas G^A_{zz} content differ.

C. Asymptotic Analysis of TLGF

Asymptotic analysis of TLGF is needed as it relates to the convergence of Sommerfeld integrals and singularity in the source region in spatial domain. TLGF decay expo-

nentially in (B.35) and (B.36) as $k_\rho \to \infty$ unless $z = z'$. By expanding the inverse resonant denominator D_n in (B.44) with geometric series as follows,

$$\frac{1}{D_n} = \sum_{k=0}^{K} (\overleftarrow{\Gamma}_n \overrightarrow{\Gamma}_n e^{-j2k_{zn}d_n})^k + \frac{(\overleftarrow{\Gamma}_n \overrightarrow{\Gamma}_n e^{-j2k_{zn}d_n})^{K+1}}{1 - (\overleftarrow{\Gamma}_n \overrightarrow{\Gamma}_n e^{-j2k_{zn}d_n})}, \tag{B.103}$$

and using the asymptotic values for the reflection coefficients,

$$\Gamma^e_{i,j} \sim \chi^e_{i,j} = -\frac{\kappa^e_i - \kappa^e_j}{\kappa^e_i + \kappa^e_j}, \quad \kappa^e_n = \sqrt{\epsilon_{tn}\epsilon_{zn}}, \tag{B.104}$$

$$\Gamma^h_{i,j} \sim \chi^h_{i,j} = \frac{\kappa^h_i - \kappa^h_j}{\kappa^h_i + \kappa^h_j}, \quad \kappa^h_n = \sqrt{\mu_{tn}\mu_{zn}}, \tag{B.105}$$

and the asymptotic values for the characteristic impedances,

$$Z^e_n = \frac{1}{Y^e_n} \sim \frac{k_\rho}{j\omega\epsilon_0\kappa^e_n}, \quad Z^h_n = \frac{1}{Y^h_n} \sim \frac{j\omega\mu_0\kappa^h_n}{k_\rho}, \tag{B.106}$$

asymptotic form of TLGF as $k_\rho \to \infty$ are found as follows,

$$V^\alpha_i \sim \frac{Z^\alpha_n}{2}\left[e^{-jk^\alpha_{z,n}|z-z'|} + \chi^\alpha_{n-1,n}e^{-jk^\alpha_{z,n}\zeta^1_n} + \chi^\alpha_{n+1,n}e^{-jk^\alpha_{z,n}\zeta^2_n}\right], \tag{B.107}$$

$$I^\alpha_i \sim \frac{1}{2}\left[\pm e^{-jk^\alpha_{z,n}|z-z'|} + \chi^\alpha_{n-1,n}e^{-jk^\alpha_{z,n}\zeta^1_n} - \chi^\alpha_{n+1,n}e^{-jk^\alpha_{z,n}\zeta^2_n}\right], \tag{B.108}$$

$$V^\alpha_v \sim \frac{1}{2}\left[\mp e^{-jk^\alpha_{z,n}|z-z'|} - \chi^\alpha_{n-1,n}e^{-jk^\alpha_{z,n}\zeta^1_n} + \chi^\alpha_{n+1,n}e^{-jk^\alpha_{z,n}\zeta^2_n}\right], \tag{B.109}$$

$$I^\alpha_v \sim \frac{1}{2Z^\alpha_n}\left[e^{-jk^\alpha_{z,n}|z-z'|} - \chi^\alpha_{n-1,n}e^{-jk^\alpha_{z,n}\zeta^1_n} - \chi^\alpha_{n+1,n}e^{-jk^\alpha_{z,n}\zeta^2_n}\right] \tag{B.110}$$

The asymptotic behavior of each TLGF is summarized in Table X.

Among the spectral kernels that involve multiple TLGF with different asymptotic forms, the ones with $O\left(\frac{1}{k_\rho}\right)$ is dropped out of the equation to obtain quasi-static forms in the spatial domain, since they go to zero as $k_\rho \to \infty$.

Table X. Asymptotic behavior of TLGF

TLGF	Order when z=z'
V_i^e, I_v^h	$O(k_\rho)$
$V_v^e, V_v^h, I_i^e, I_i^h$	$O(1)$
V_i^h, I_v^e	$O\left(\frac{1}{k_\rho}\right)$

D. Computation of Sommerfeld Integrals

The spatial domain kernels are obtained by integrating the spectral domain as follows,

$$G = S_n\{\tilde{G}\} = \frac{1}{2\pi}\int_0^\infty \tilde{G} J_n(k_\rho \rho) k_\rho dk_\rho \tag{B.111}$$

Integration path for Sommerfeld integrals is shown in Fig. B-3. First term on the right hand side in (B.111) can further be separated into three sub-integrals as follows,

$$S_n\{\tilde{G}\} = I_a + I_b + I_c \tag{B.112}$$

I_a is the integral along the sine path in Fig. B-3,

$$I_a = \frac{1}{2\pi}\int_0^{k_{xmax}} \tilde{G} J_n(k_\rho \rho) k_\rho \frac{dk_\rho}{dt} dt, \tag{B.113}$$

$$k_\rho = t + j k_{ymax} \sin\left(\frac{\pi t}{k_{xmax}}\right) \tag{B.114}$$

where t is real. I_b is the integral from k_{xmax} to the first break point bp_1 in the real axis,

$$I_b = \frac{1}{2\pi}\int_{k_{xmax}}^{bp_1} \tilde{G} J_n(k_\rho \rho) k_\rho dk_\rho, \tag{B.115}$$

I_c is the tail integral in the real axis,

$$I_c = \frac{1}{2\pi} \int_{bp_1}^{\infty} \tilde{G} J_n(k_\rho \rho) k_\rho dk_\rho = \sum_{i=1}^{\infty} u_i, \tag{B.116}$$

where

$$u_i = \frac{1}{2\pi} \int_{bp_i}^{bp_{i+1}} \tilde{G} J_n(k_\rho \rho) k_\rho dk_\rho \tag{B.117}$$

The integrals I_a and I_b are computed by an adaptive quadrature based on the Patterson rule. I_c is computed by either Patterson or Gaussian-Legendre quadratures. I_c is a sequence of partial sums which is accelerated by using weighted averages extrapolation method [73].

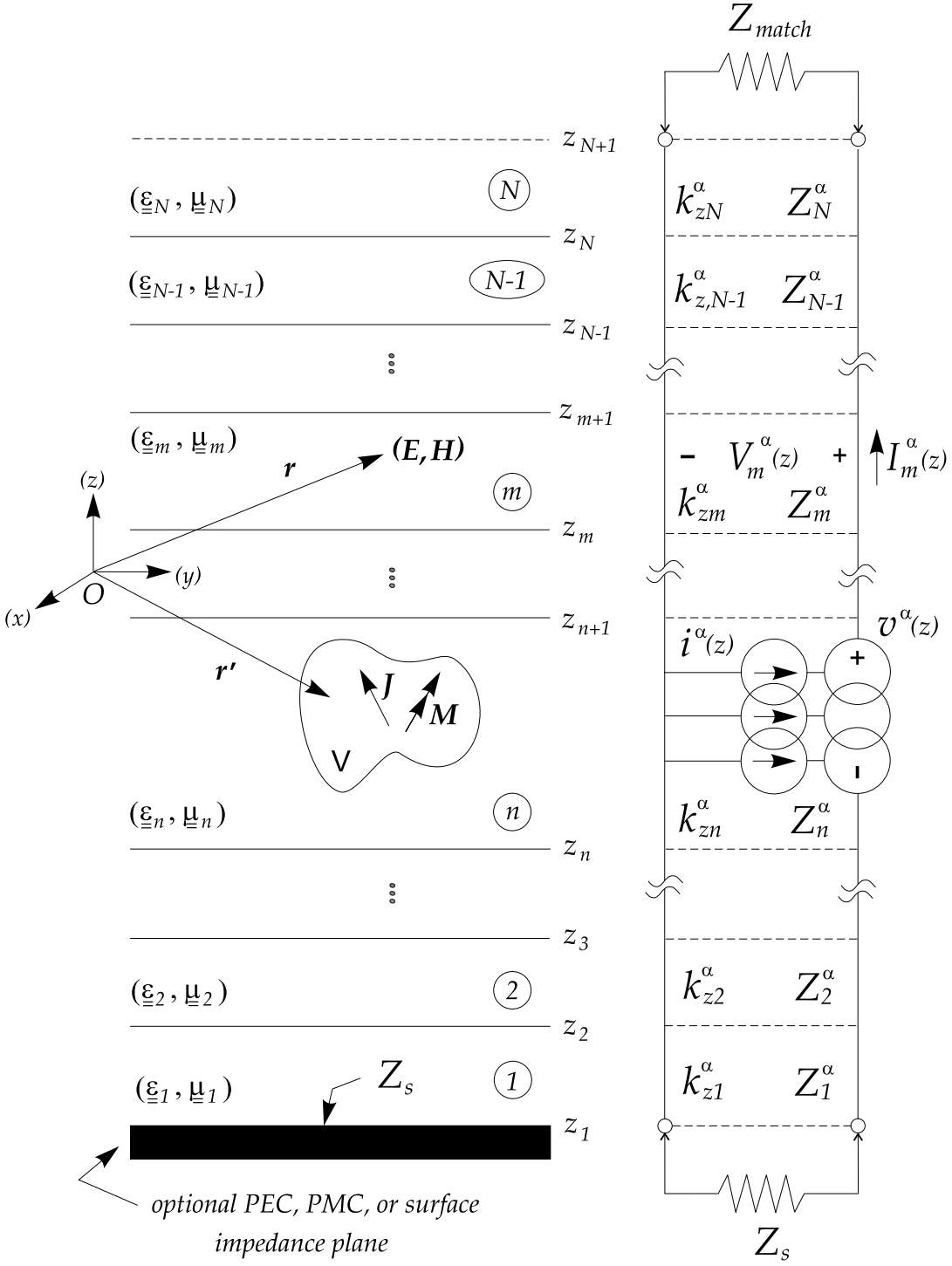

Fig. B-1. Transmission line representation of layered media

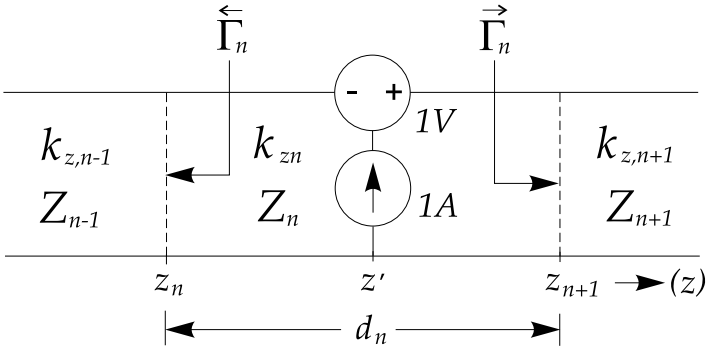

Fig. B-2. Voltage and current sources in section n of a trasmission line

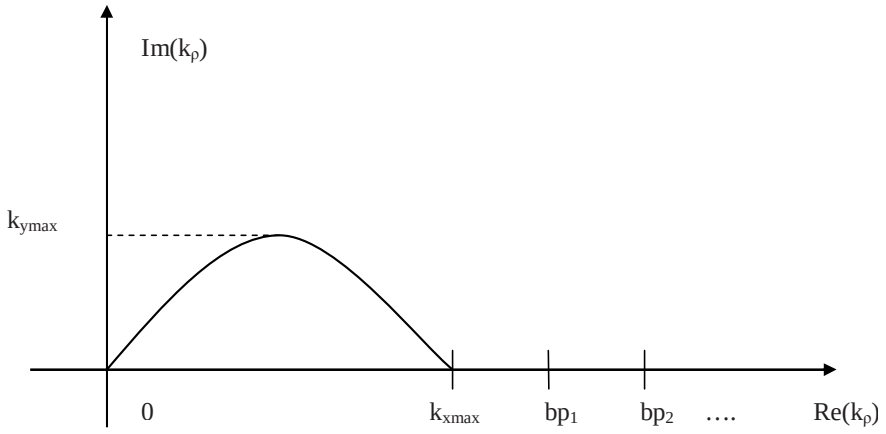

Fig. B-3. Sommerfeld integration path

VITA

Nur Kurt Karsilayan was born in Corum, Turkey. She was ranked the first among high school graduates in Corum Anadolu Lisesi. She was ranked the first and among the top 120, citywide and nationwide, among the thousands and about a million students, competing in the National University Entrance Exams, respectively. She received her B.S. degree in electrical and electronics engineering from Bilkent University, Ankara, Turkey in 1995, where she was also awarded a full undergraduate scholarship and graduate research assistantship. She earned her M.S. degree in electrical and computer engineering from Portland State University, Portland, OR in 1998 where she was a research assistant sponsored by Mentor Graphics. She won the outstanding M.S. student award at Portland State University. She was an intern at Mentor Graphics between July 1997 and January 1998. She has been an employee of Mentor Graphics since January 1998, where she has designed and led various parasitic extraction modeling projects with success, and was promoted twice. She has been pursuing her Ph.D. degree in electrical engineering at Texas A&M University, College Station, TX since 2000, while working full-time at Mentor Graphics. She is a member of IEEE, Tau Beta Pi and Eta Kappa Nu. She is also a Graduate Teaching Academy fellow at Texas A&M University. Her research interests include parasitic extraction of interconnects and the substrate, computational electromagnetics and data modeling.

Address: Department of Electrical and Computer Engineering, Texas A&M University, College Station, TX